AN EXPERIMENTAL STUDY OF LIGHT-MATERIAL INTERACTION AT SUBWAVELENGTH SCALE

BY

HYUNGJIN MA

DISSERTATION

Submitted in partial fulfillment of the requirements
for the degree of Doctor of Philosophy in Physics
in the Graduate College of the
University of Illinois at Urbana-Champaign, 2011

Urbana, Illinois

Doctoral Committee:

Professor Paul G. Kwiat, Chair
Assistant Professor Nicholas X. Fang
Professor J. Gary Eden
Professor Robert M. Clegg

Abstract

The recent emergence of nanotechnology offers a new perspective in the field of optics. The study of light-material interaction has evolved into a nanoscale regime with its dimension smaller than the wavelength of light. While there are pressing needs of optical applications with higher resolution and efficiency, one important hurdle is the so-called diffraction limit that originates from light's inherent wave nature. Based on the localized electromagnetic field generation due to the resonant oscillation of electron plasma in metal, plasmonics offers new opportunities for manipulating light at the subwavelength scale. This dissertation investigates the effects of electromagnetic field confinement on light-material interaction inside nanoscale metal-dielectric composite structures.

One of the simplest structures is a subwavelength hole perforated on a thin metal film. The scalar diffraction theory by Kirchhoff fails to explain the nature of light at nanoscale. Later, it was pointed out by Bethe that light in a small hole can be represented by the electric and magnetic dipole fields which satisfy the boundary conditions at the screen. Using near-field scanning optical microscope (NSOM), I have experimentally studied light transmission through a subwavelength hole, and found an unusually large amount of phase shift in the transmitted light contradicting Bethe's theory. Such effect is explained by the strong contribution of in-plane electric dipole field due to the excitation of surface plasmon wave.

An important challenge to the study of a localized light field is the requirement of non-traditional optical tools that can probe the near-field of light with subwavelength resolution. The cathodoluminescence (CL) microscope, which is a variation of the electron microscope (that has an imaging resolution better than 10nm), is employed to generate a point-like dipole light source using an electron beam in a controlled way. By using CL to excite local plasmonic modes in a

nanoscale metal-air-semiconductor bubbles, I demonstrate an ultrasmall mode volume and cavity-enhanced luminescence from a plasmonic structure. Numerical calculation based on a point dipole model indicates that such an effect is a result of increased local optical density of states (LDOS) due to a strong localized field. This device enables a way to generate localized light from a continuous active medium with high quantum efficiency, which is potentially useful for on-chip subwavelength optoelectric applications.

Active optical devices sometimes involve an interaction between a plane electromagnetic wave and an active optical medium, which interaction can be modulated by an external stimulus, such as optical or electric pumping. The optical non-linearity of active media available in nature is, in general, extremely weak. Therefore, either bulky or highly resonant structures are required to build an effective, active optical device. Artificially engineered material, sometimes referred as a "metamaterials," can have optical properties that are not naturally available. I demonstrate an efficient optical modulator based on a plasmonic metamaterial, which takes advantage of enhanced light-matter interaction within a small-footprint device. Simple modeling and numerical simulation is performed to identify a strong localized field that is due to magnetic resonance. A far-field optical characterization, based on the pump-probe technique, is performed, to demonstrate all-optical modulation with an ultrafast response time of 2ps and a modulation depth of 40%.

To my family

Acknowledgment

It has been an extraordinary experience to study an exciting new field of physics at the graduate program of the University of Illinois at Urbana-Champaign. It is my pleasure to thank everyone surrounding me for their support and encouragement.

First of all, I'd like to express my sincere thanks to my advisor, Prof. Nicholas Fang, for his inspiring guidance throughout my graduate studies. His enthusiasm and vision always has been a source of great new ideas, motivation and advancement. Without his support, I would not have reached this far today.

I was fortunate to work with a group of people who shares curiosity and enthusiasm in the field of nanotechnology. Their invaluable supports and discussions allowed me to move forward. I am thankful to Dr. Jun Xu for his guidance and lively discussions; Dr. Kin Hung Fung and Dr. Pratik Chaturvedi for various numerical simulation; Dr. Anil Kumar and Dr. Keng Hsu for their help on sample fabrications. I am also thankful to all other group members, Howon Lee, Dr. Chuguang Xia, Dr. Tarun Malik, Dr. Shu Zhang, Shinhu Cho, and Matthew Alonso for a friendly environment.

I am also thankful to the staffs in the Frederick Seitz Material Research Laboratory for providing extensive help for me to carry out necessary experiments. It was also pleasure to work with collaborators from U.C. Berkeley, Prof. Ron Shen and David Cho who provided valuable resources and experimental tools.

Finally, I am grateful to my family for everlasting love and support. Some of my close friends, Joonho Jang, Youngil Joe, Hyeongjin Kim and Minjung Kim made me possible to get through difficult times and add great memories that I will always cherish.

Table of Contents

Chapter 1 Introduction

1.1. Background and Motivation

The spatial and spectral imaging of light interacting with matter provides valuable information in physical, chemical and biological systems. One important limitation of optical imaging tool is the diffraction limit discovered by Abbe [1] and Rayleigh [2] in the late nineteenth century. Recent advances in technology have driven strong research in nanoscale science, and researchers have investigated possibilities for manipulating light beyond the diffraction limit. A high precision optical technique, such as Förster resonance energy transfer (FRET), has demonstrated the possibility to measure the distance between fluorescence molecules within a ten nanometer scale [3,4]. Variations of high resolution fluorescence microscopy techniques, such as stimulated emission depletion (STED) [5,6], photo-activated localization microscopy (PALM) [7], and stochastic optical reconstruction microscopy (STORM) [8], have been developed and shown to have strong potential in biological applications. However, these techniques require specific types of fluorophores, and are limited due to weak fluorescence intensity, photobleaching and the complicated process of achieving high resolution.

Direct measurement of an evanescent field that contains subwavelength information enables high resolution imaging. A near-field scanning optical microscope (NSOM) is used to collect the scattered evanescent field, demonstrating sub-wavelength resolution [9]. Since Ebbesen's [10] discovery in 1998 of extraordinary transmission, researchers have studied the role of surface plasmon polaritons (SPPs) in the transmission of light through patterned metallic

films [11,12]. A SPP has a wavelength shorter than that of light propagating in free space and is confined on a metal surface, which makes it one of the most promising candidates for on-chip subwavelength optics. NSOM has been successfully employed to investigate the local field profile in passive optical components, such as subwavelength waveguides and splitters [13,14,15,16]. Localized surface plasmon on metallic nanostructures focuses light into a small region beyond the diffraction limit, and, therefore, enables high density optical recording [17,18]. The strong localized field can also be utilized in biosensor applications [19].Using thin silver film, a superlens that recovers near-field information has been realized by amplifying the evanescent field [20,21].

An entire new generation of materials, termed "plasmonic metamaterials," has emerged [22]. Unconventional optical properties, such as a negative index of refraction, have been proposed and demonstrated [23,20,24]. With the capability of engineering-designed optical properties, based on the concept of metamaterials, exotic optical devices, such as the invisibility cloak, have been realized [25, 26]. Moreover, the application of plasmonics is no longer limited to miniaturized optics or high resolution imaging. The concepts and applications of metamaterials will be further discussed in the following chapter.

The development of modern information technology is largely indebted to the invention of active optical devices such as the laser, optical modulator, and photodetector, which rely on the sophisticated use of light-matter interaction [27,28]. One of the great advantages of using light for communication is its capacity for high bandwidth operation, which electronics cannot provide due to the inherent limitation imposed by carrier mobility. The feature size of semiconductor electronics has been miniaturized to a few tens of nanometers, according to Moore's law. However, in its optical counterpart (i.e., silicon photonics), the dimension is near a

few hundred nanometers due to the diffraction limit. Therefore, the role of plasmonics in scaling down optical counterparts to build highly integrated optoelectric devices is essential in future active plasmonics [29]. To build highly efficient active plasmonic devices, it is critical to understand light-matter interaction at the nanoscale, both fundamentally and from the perspective of practical applications [30].

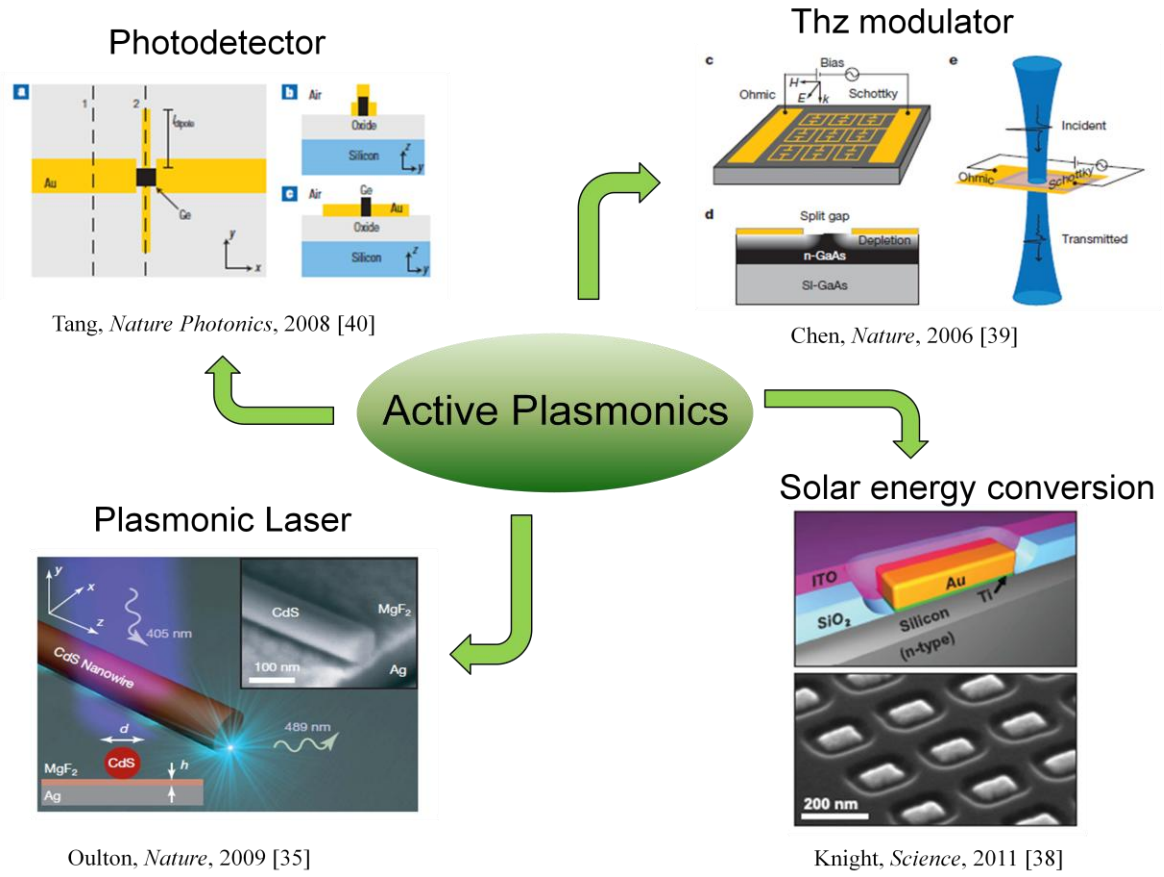

Figure 1.1 Wide ranges of applications are driving current research in active plasmonics. Some of the applications include various active optical components, such as photodetectors, optical modulators, nanoscale lasers and nano-antenna solar cells.

The enhancement of Raman signatures due to a strong localized field on roughened silver was demonstrated in 1974 [31]. This effect, explained as surface-enhanced Raman scattering (SERS), was later utilized to detect single molecules [32]. Purcell indicated that light-matter

interaction could be improved by cavity resonance in classical optics [33]. Lifetime and spectral measurements of light generated from a plasmonic cavity display the Purcell effect, which leads to the nanoscale laser demonstrated by several groups [34, 35, 36, 37]. A strong localized field can also improve solar energy harvesting in the off-bandgap near-IR region [38]. The THz optical modulator, based on split-ring-resonator (SRR), has been demonstrated [39]. A nanoscale dipole antenna was placed to improve the efficiency of the photodetector at a near-IR range [40]. In these applications, plasmonics plays an important role in improving the efficiencies of the devices.

The intricate structure of these novel active plasmonics devices is derived from physics-driven design for desired properties and applications. These designs require a solid understanding of physical principles as well as novel characterization techniques. In this dissertation, I explore the field of active plasmonics to address important applications, namely, the nanoscale light emitting device and metamaterial optical modulator for telecommunication. The objective of this research is three fold: (1) to study light-matter interaction at the nanoscale, (2) to explore a near-field characterization tool that provides information on local optical modes beyond diffraction limit, and (3) to develop efficient active plasmonic devices at the microscopic and macroscopic scale.

1.2. Metamaterial

Metamaterials are artificially engineered materials which have unusual properties that may not exist in natural material. Metamaterials are composed of unit cells that are designed to give specific properties originating from their structure rather than composition. An individual unit is

often referred as an artificial atom, in analogy to the atom in conventional material (See Fig. 1.2). In most cases, unit cells are arranged in a periodic manner, with a lattice constant much smaller than the wavelength, so that they can be represented by effective macroscopic parameters. Electromagnetic properties are usually implied, but acoustic and seismic properties are also actively being studied [41,42].

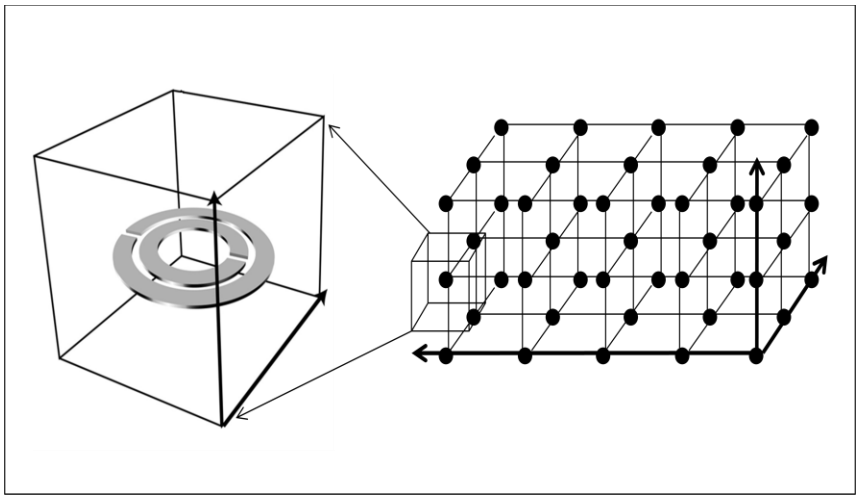

Figure 1.2 Schematic drawing of three dimensional metamaterial. An individual unit shown on the left side is usually composed of metal and dielectric materials, with dimensions smaller than the wavelength of interest.

Individual plasmonic structures such as metallic particles and cavities by themselves give interesting properties with plethora of potential applications. As the size of such structures becomes comparable or larger than the wavelength of operation, the quasistatic approximation no longer holds, and therefore it becomes harder to understand the optical behavior due to the retardation effect [43]. However, in the case where the subwavelength structures are periodically arrayed and form a macroscopic structure, the overall medium can be described by the averaged effect of individual units, i.e., treated as a bulk medium with representative macroscopic parameters [50]. Even more interesting, it is possible to engineer certain artificial optical properties that are not readily available in nature. Novel properties, such as negative refractive index [23,20], which has both negative

dielectric permittivity and magnetic permeability, negative refraction, inversed Doppler shift and lens beyond the traditional diffraction limit have been proposed and demonstrated [20,44].

Over the past few years, the operating frequency of artificially engineered plasmonic metamaterials has been extended into the optical frequency range, enabling, e.g., optical magnetism [45]. With a careful design of artificial structures supporting magnetic resonance, both negative electric permittivity and magnetic permeability can be achieved at visible wavelengths [46,47]. Also, negative refraction effects in the optical range have been experimentally observed [45]. One of the interesting aspects of optical metamaterials is the capability to perform as a fast optical switch/modulator in telecommunication due to the resonance [48,49]. Photoexcitation of carriers in a constituent semiconductor layer or the substrate leads to modulation of optical properties such as effective refractive index and resonance frequency of the metamaterial.

Characterization of discrete materials is sometimes based on homogenization theory. An electromagnetic response of conventional material is affected by the electric and magnetic fields in the medium. It is generally complicated due to spatial inhomogeneity, non-linearity and mutual interaction between electric and magnetic fields. However, when the wavelength of interest is much larger than the size and spacing of atoms in the medium, the main response can be described by linear combination of incident fields with corresponding bulk parameters of electric permittivity(ε) and magnetic permeability(μ), eliminating the complexity by taking the spatial average effect. If the wavelength is comparable to the lattice constant of metamaterial, complex diffraction and scattering effects will be involved, and one can no longer use simple material parameters to describe the phenomenon. Assuming that the spatial variation of incident fields is small compared to the variation due to inhomogeneity, we can have effective parameters satisfying following equations [50]:

$$\varepsilon_{eff} \equiv \frac{<\mathbf{D}>}{\varepsilon_0 <\mathbf{E}>} \text{ and } \mu_{eff} \equiv \frac{<\mathbf{B}>}{\mu_0 <\mathbf{H}>} , \quad (1.1)$$

where $\mathbf{D}, \mathbf{E}, \mathbf{B}$ and $\mathbf{H}$ are the displacement field, electric field, magnetic field, and associated magnetic field, respectively. The symbol $< \ >$ denotes a spatial average of the fields over the unit cell, and ε_0 and μ_0 are the free-space electric permittivity and magnetic permeability.

The response of an artificial atom can be designed to give unusual properties which go beyond that of conventional atoms listed in the periodic table. One example is a double negative material (DNG), where both ε and μ are negative. Wave propagation in a DNG medium was first described theoretically by Veselago in 1967 [23]. Maxwell's equations in isotropic medium without any sources are

$$\mathbf{k} \times \mathbf{E} = \omega \mathbf{B} = \omega \mu_{eff} \mu_0 \mathbf{H} \text{ and } \mathbf{k} \times \mathbf{H} = -\omega \mathbf{D} = -\omega \varepsilon_{eff} \varepsilon_0 \mathbf{E}, \quad (1.2)$$

where $\mathbf{k}$ is the wavevector.

When a wave propagates in a conventional dielectric medium, equation (1.2) shows that the electric field $\mathbf{E}$, magnetic field $\mathbf{H}$ and wavevector $\mathbf{k}$ follow the right-handed rule: ($\hat{\mathbf{E}} \times \hat{\mathbf{H}} = \hat{\mathbf{k}}$). In the case of a DNG medium, waves still can propagate through the medium but instead follow the left-handed rule: ($\hat{\mathbf{E}} \times \hat{\mathbf{H}} = -\hat{\mathbf{k}}$). For this reason, a DNG medium is often called a left-handed medium (LHM), while a standard dielectric medium is a right-handed medium (RHM). It should be noted that the handedness of DNG or DPS medium is not related to the handedness of circularly polarized light or any chirality in geometrical structure of the medium.

Considering that the Poynting vector is defined as $\mathbf{S} = \mathbf{E} \times \mathbf{H}$, the phase velocity (in the direction of $\mathbf{k}$) is now opposite to the direction of group velocity (in the direction of $\mathbf{S}$), indicating a backward propagating wave. The index of refraction is defined as $n = \pm\sqrt{\varepsilon\mu}$, but it is required that $\mathrm{Im}(\varepsilon) > 0, \mathrm{Im}(\mu) > 0$ for passive DNG medium, and therefore only the negative square root of n is

chosen. For this reason, a DNG medium is also referred as a negative index material. Also, the real part of impedance is positive, $Z = \sqrt{\mu / \varepsilon}$.

For an isotropic medium, one can determine the angle of refraction using Snell's law, $n_1 \sin\theta_1 = n_2 \sin\theta_2$. If a wave propagates across the interface between a dielectric and a DNG medium, the angles θ_1 and θ_2 have opposite signs, and therefore the wave displays negative refraction (See Fig.1.2). This is a direct consequence of boundary conditions at the interface where the parallel component of the **k** vector must be matched. Other examples of unusual properties of DNG medium which can be found in the literature [23] are reversed Doppler shift and reversed Cherenkov radiation.

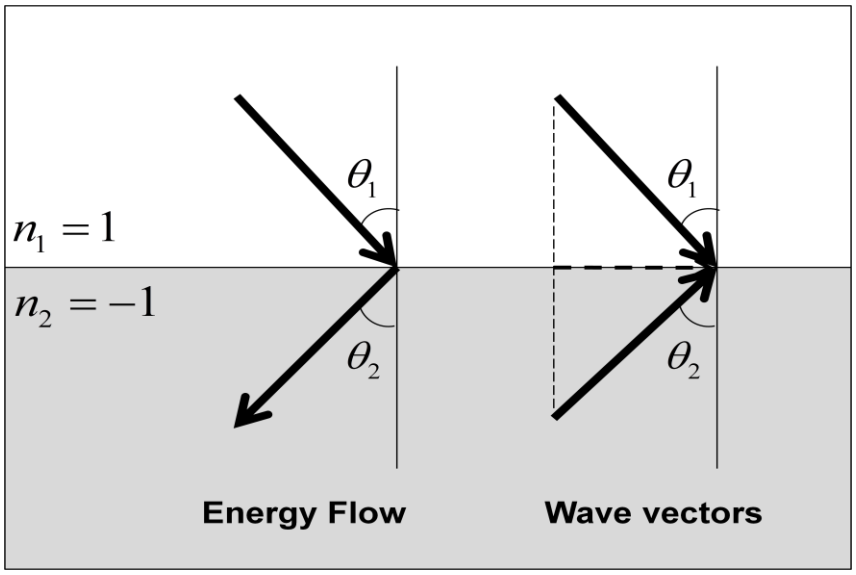

Figure 1.3 Illustration of negative refraction between a dielectric and a DNG medium.

There is a special case of negative refraction when the electric and magnetic responses of materials are coupled:

$$\mathbf{D} = \varepsilon\mathbf{E} - i\kappa\mathbf{H} \text{ and } \mathbf{B} = i\kappa\mathbf{E} + \mu\mathbf{H}, \tag{1.3}$$

where κ indicates the strength of chirality and i represents a $90°$ phase shift in response.

Such a medium is called a bi-isotropic material, since two propagating wave eigenmodes exist. The corresponding refractive indices of these two eigenmodes are $n = \sqrt{\varepsilon\mu} \pm \kappa$. In the case where $|\kappa| > \sqrt{\varepsilon\mu}$, the index can be negative without both electric permittivity and magnetic permeability being negative [51].

One important characteristics of a negative index material is its ability to resolve beyond the diffraction limit. In 2000, it was proposed by Pendry that a slab of negative index material can overcome the resolution limit of conventional lenses to achieve a perfect lens [20]. Imagine we have an infinitesimal dipole of frequency ω in front of a lens. 2D Fourier expansion of electric field yields:

$$\mathbf{E}(\mathbf{r},t) = \sum_{\sigma,k_x,k_y} \mathbf{E}_\sigma(k_x,k_y)\exp(ik_z z + ik_x x + ik_y y - i\omega t) \ , \qquad (1.4)$$

where $k_z = \sqrt{\omega^2/c^2 - {k_x}^2 - {k_y}^2}$, k_x and k_y indicate in-plane components of wavevector, and k_z is the wavevector along the propagation direction. For those components with ${k_x}^2 + {k_y}^2 > \omega^2/c^2$, k_z becomes imaginary and therefore decaying exponentially with increasing z. Information of subwavelength features that are stored in higher in-plane wavevector will be lost as the observer goes far away from the object; the resolution is thus determined from the maximum in-plane wavevector with real k_z, given by $\Delta = \frac{2\pi}{k_{\max}} = \frac{2\pi c}{\omega} = \lambda$.

However, if the medium has a negative index, the wavevector becomes opposite in sign, given by $k_z' = -\sqrt{\omega^2/c^2 - {k_x}^2 - {k_y}^2}$, meaning exponential growth of the evanescent field. This does not violate energy conservation because the evanescent field does not transport energy. A slab of negative index material can serve as a focusing lens due to negative refraction. This lens can recover not only propagating components, but also evanescent components by amplification of previously

decaying components and therefore can recover information of features smaller than a wavelength (See Fig.1.4). Ideally this lens does not have a resolution limit, and is called a perfect lens.

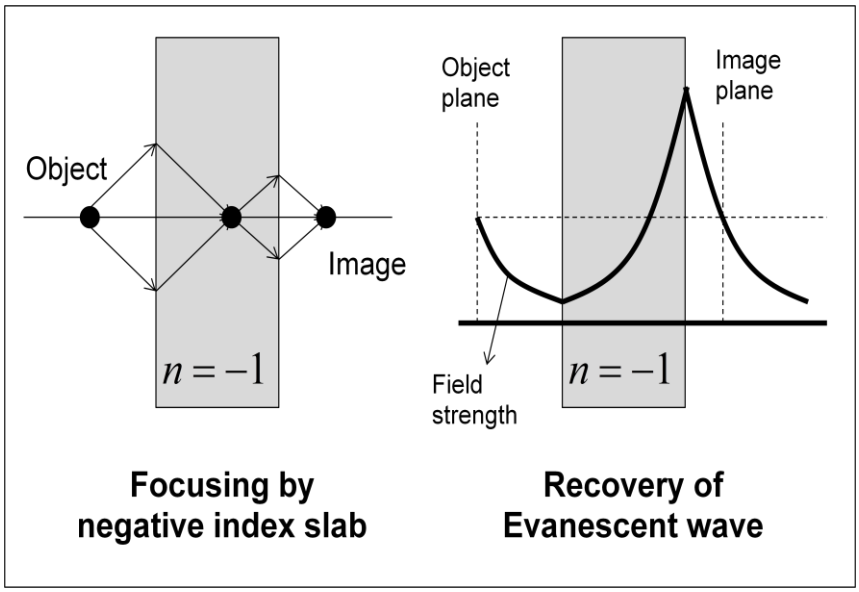

Figure 1.4 Perfect lens made from negative index material.

In reality, the resolution of a perfect lens is limited by several factors such as frequency dispersion and the size of the unit cell. It is also limited by its near-sightedness, in the sense that the object and image should be close to the lens. In a special case of quasistatic limit, even a single negative material can exhibit similar effects. In the optical regime, this concept was demonstrated using a silver slab lens by Fang et al. [21].

1.3. Thesis Organization

This dissertation is organized into five chapters. Chapter 1 provides a brief introduction and the objectives of this study. The contents of the other four chapters are organized as follows.

An active plasmonic device sometimes operates through absorption, modulation and generation of a plane light wave that is mediated by SPP. However, excitation of SPP requires a momentum-matching condition between light and SPP, which needs to be considered in the design of such devices. Nanostructures on a metallic film can provide the necessary momentum to excite SPP. One of the simplest structures is a subwavelength hole perforated on a thin metal film. Chapter 2 focuses on the interaction between such a structure and a plane light wave. Near-field scanning optical microscopy (NSOM) is employed to study the phase shift of light that is transmitted through the hole. Limitations of classical diffraction theory and the role of SPP in light transmission are explained.

Arrays of an individual plasmonic unit give rise to unique optical properties that are not available in nature. In chapter 3, the development of a fishnet, metamaterial-based, all-optical modulator for telecommunication is discussed. Based on LC circuit-based modeling and finite difference time domain (FDTD) simulation, the negative index fishnet metamaterial is designed to operate at telecommunication wavelength. Optical characterization of the fishnet slab in both the near-field and far-field regimes is performed to elucidate the role of magnetic resonance in potential applications for all-optical modulation. The coupling of local fishnet modes with a fiber-guided mode is studied for a potential on-fiber modulator. A rotated fishnet structure is proposed to improve the modulation depth in an on-fiber modulator.

To investigate light-matter interaction at the nanoscale, it is essential to develop an optical characterization technique for the analysis of subwavelength nanostructures, as well as theoretical modeling to address physical principles. In Chapter 4, a cathodoluminescence microscope (CL) is utilized to study the Purcell effect in a nanoscale bubble cavity. The design and analysis of a plasmonic metal-air-semiconductor cavity is provided to explain the relation

between strongly localized SPP modes and enhanced luminescence from the cavity. Details of experimental processes, including fabrication and optical characterization, are provided. Dipole-based modeling is proposed to explain the experimental results. The potential application of a nano-bubble cavity as a light emitting device is analyzed. Finally, Chapter 5 summarizes of the work presented in this thesis and the future outlook of active plasmonic devices based on engineered metallic nanostructures.

Chapter 2 Light Transmission through a Subwavelength Hole

2.1. Introduction

Due to the ability of concentrating photons into subwavelength dimensions, plasmonic nanostructures have enabled a new frontier in nano-photonics, with promising applications of energy transport and conversion. Investigation of the interaction between light and a single subwavelength hole or array of holes is of particular interest. Although an analytical solution of light diffracted by a subwavelength hole was first derived by H.A. Bethe in 1944 [60], it was later challenged by the pioneering work of T.W. Ebessen [65]. The transmission of light through a subwavelength hole array at optical frequencies was found to be three orders of magnitude larger than it is supposed to be based on Bethe's theory. Multiple theories were proposed and numerous experiments were performed, but there are still controversial arguments going on.

In one dimensional periodic subwavelength slit structures, the resonant excitation of delocalized, Bloch-state surface plasmon polariton waves (SPP) [11] has been proposed to explain the peaks in light transmission observed when the wavelength of SPP is tuned near integer multiples of the periodicity of the array. Also, in the two dimensional case, localized surface plasmon (LSP) modes of individual apertures that contribute to the transmission peaks associated with the periodic arrays have been suggested to explain experimental results of enhanced transmission [12].

Concomitant with research into extraordinary transmission through subwavelength hole arrays, the phase shift of incident and SPP waves has been also studied. A composite diffracted evanescent wave (CDEW) model [52] predicted a phase shift of $\pi/2$ between the incident and E_x component of the electric field diffracted in a sub-wavelength hole on a metal surface. Using finite element field simulation [53], a subsequent result showed a phase shift of π between the incident and SPP scattered wave magnetic field H_y scattered by a subwavelength-width slit. Otherwise, using field continuity condition and a simple application of Faraday's law of induction, one finds that a SPP wave is in anti-phase with the incident wave in a one-dimensional subwavelength structure [54]. However, an experimental measurement of phase shifts in subwavelength structures is still a great challenge.

Recently, due to the progress of experimental technology, it has become possible to measure the optical transmission and diffraction in a single subwavelength hole [55,56]. Also, the SPP wave generated by an isolated nano-hole on thin Au film has been detected by near-field scanning optical microscopy (NSOM) [57].

In this chapter, I study the role of SPP in transmission of light through a single subwavelength hole based on the measurement of phase. Unconventional phase shift originating from SPP excitation and scattering is observed. The existence of an in-plane dipole moment is observed, an effect not previously considered by Bethe in his diffraction theory.

2.2. Theory of Diffraction

The first systematic approach to explain the Huygens-Fresnel principle from first principles was done by Kirchhoff in 1882 [58]. Even though his theory has an inherent

mathematical flaw, it still works remarkably well in the optical domain when the size of structure is larger than the wavelength. The failure of Kirchhoff's theory is easily seen in his original scalar formulation. Let u be a scalar wave describing a diffracted wave on the right side of the screen in Fig. 2.1 (a). The boundary condition on the screen is assumed to be:

$$u_{screen} = 0,\ \frac{\partial u_{screen}}{\partial x'} = 0. \tag{2.1}$$

The Helmholtz equation $\nabla^2 u + k^2 u = 0$ can be solved using given boundary condition to get field profile at any point on the right side of the screen. Using Green's theorem with $G(\mathbf{x},\mathbf{x}') = \varphi(|\mathbf{x}-\mathbf{x}'|) = \varphi(r) = e^{ikr}/r$, we get $u(\mathbf{x}) = \int_S da\left[-\frac{\partial u_0}{\partial x'}(\mathbf{x}')\varphi(|\mathbf{x}-\mathbf{x}'|) + u_0(\mathbf{x}')\frac{\partial \varphi}{\partial x'}\right]$.

In the case of a small hole, the field is assumed to be uniform over the area, and therefore,

$$u(r) = -A\left[\frac{\partial u_0}{\partial x'}\varphi(r) + u_0\frac{\partial \varphi(r)}{\partial x}\right]. \tag{2.2}$$

On the screen outside the hole area, the second term vanishes but the first term does not, in contradiction with the initial assumption given in (2.1).

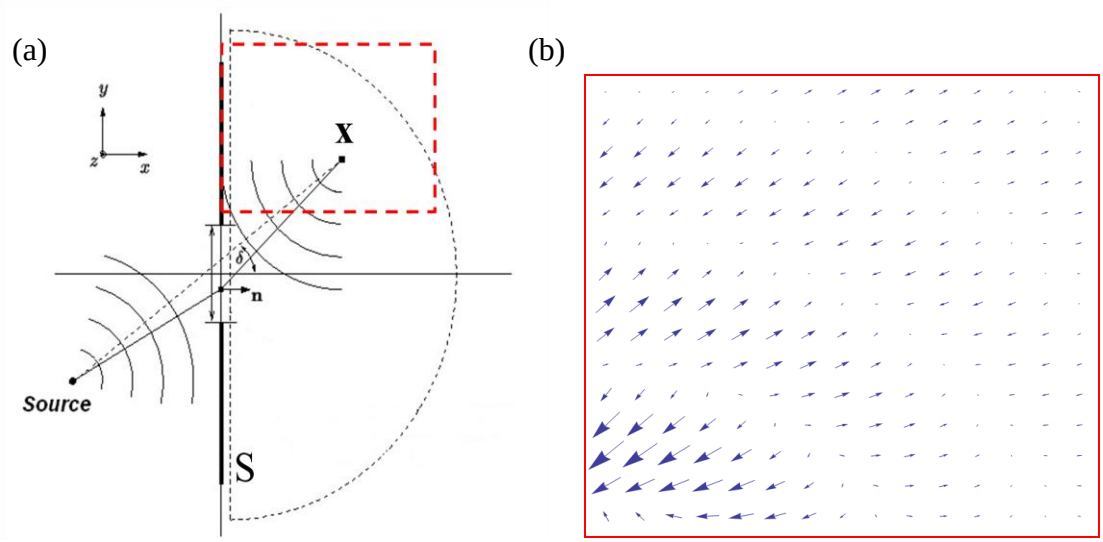

Figure 2.1 (a) Schematic drawing of diffraction by a slit (b) A plot of diffracted electric field calculated by vectorial extension of Kirchhoff's diffraction theory. The plotted area is indicated by red square in Fig 2.1 (a)

Kirchhoff's theory has an additional defect of being a scalar theory, which was extended to vectorial electromagnetic waves by several authors. Here we only quote the result from Stratton [59]:

$$\mathrm{E}(\mathbf{x}) = \frac{1}{4\pi}\int_S da\left[ik\,\mathrm{n}\times\mathrm{H}(\mathbf{x}')\varphi - (\mathrm{n}\times\mathrm{E}(\mathbf{x}'))\times\nabla\varphi - \mathrm{n}\cdot\mathrm{E}(\mathbf{x}')\nabla\varphi\right] . \qquad (2.3)$$

In the case of using perfect conducting material as a screen, naturally we have a boundary condition of $\mathrm{E}_{t,screen} = 0$ and $H_{n,screen} = 0$. In general the normal component of **E** and tangential component of **H** are not zero. In the limit of a small hole, the first and third components in equation (2.3) have tangential components of **E**, contradicting with the boundary condition. It's clear that vectorial version of Kirchhoff's theory fails in the field plot of equation (2.3), given in figure 2.1(b), assuming that the light source is a plane wave illuminating along normal direction.

In 1944, H.A. Bethe overcame the shortcomings of Kirchhoff's theory and gave an analytical solutions of the diffracted electromagnetic field for the first time in the case of a hole

that is small compared to the wavelength of light [60]. Later the solution was corrected by Bouwkamp with an additional 2nd-order term to improve the distribution near the hole region [61]. It was also shown that the same solution can be obtained by using alternative charge and current distribution [62]. The solution was experimentally tested at microwave wavelengths by several authors, and showed a good match with theoretical calculation [63,64].

The first assumption of Bethe's theory is that the screen is infinitely thin and perfect electrically conducting (PEC). Therefore the tangential component of **E** and the normal component of **H** is zero on the screen. This is usually the case for metal in the long wavelength limit. The second assumption gives the boundary condition in the hole. When the size of the hole is much smaller than the wavelength, we can ignore the effect of retardation and assume that the field is uniform in the hole. It is also assumed to be an unperturbed field which is a directly given from the incident field.

By using the continuity condition and Maxwell's equation, the boundary condition on the screen is as follows:

$n \times E_0 = 0\,,\ H_0 \cdot n = 0$ on the screen outside the hole;

$E_{1,\tan} = E_{2,\tan} = 0\,, H_{2,\tan} = \frac{1}{2} H_{0,\tan}\,, E_{2,n} = \frac{1}{2} E_{0,n}$ in the hole.

Here the subscripts 0,1 and 2 denote the incident, reflected and transmitted wave respectively.

We want to calculate the charge and current distribution satisfying the specified boundary condition. To solve this, Bethe used fictitious magnetic charge and current which do not have actual physical meaning, but yield a rather simple analytical solution. Of course, it was shown later that the same field distribution can be achieved using antisymmetric surface electric current without using any hypothetical magnetic charge or current [62], but here we will follow Bethe's original steps and address its physical meaning.

In terms of magnetic charge and current, Maxwell's equation can be written as follows [59]:

$$\nabla \cdot E = 0, \nabla \times E + \frac{1}{c}\frac{\partial \rho^*}{\partial t} = -4\pi J^*, \ \nabla \cdot H = 4\pi \rho^*, \nabla \times H = \frac{1}{c}\frac{\partial E}{\partial t} \ , \qquad (2.4)$$

where superscript * indicate magnetic charge and current. In a similar way, we can define a continuity equation, and scalar and vector potentials:

$$\nabla \cdot J^* + \frac{1}{c}\frac{\partial \rho^*}{\partial t} = 0, \ E = \nabla \times F, \psi(r) = -\int \eta(\mathrm{x}')\varphi(r)d\,\mathrm{x}', \ F(r) = -\int K(\mathrm{x}')\varphi(r)d\,\mathrm{x}', \ (2.5)$$

where η and K mean surface magnetic charge density and magnetic current density, respectively.

It is well known in electrostatics that a uniform dipole density gives uniform field distribution in the spheroid. For a very thin oblate spheroid surface, the magnetic dipole density can be approximated to be $\mu \sim \sqrt{a^2 - \mathrm{x}'^2}$, and therefore the magnetic charge density becomes

$$\eta \sim H_0 \cdot \nabla \mu = -C\frac{H_0 \cdot \mathrm{x}'}{\sqrt{a^2 - \mathrm{x}'^2}} = -\frac{H_0 \cdot \mathrm{x}'}{\pi\sqrt{a^2 - \mathrm{x}'^2}}, \qquad (2.6)$$

The corresponding magnetic current distribution is $K_m = -\frac{ik\sqrt{a^2 - \mathrm{x}'^2}H_0}{\pi^2}$ but this is one order smaller value and not enough to satisfy electric field boundary condition. An additional contribution from circular loop of magnetic current is required to fulfill the boundary condition of normal electric field: $F = \frac{1}{4}E_0 \times \mathbf{x} = -\int K(\mathrm{x}')\varphi(r)d\,\mathrm{x}', E = \nabla \times F = \frac{1}{2}E_{0,x}$ therefore, we get

$$K_E = -\frac{\mathrm{x}' \times E_0}{2\pi^2\sqrt{a^2 - \mathrm{x}'^2}}.$$

Overall, total magnetic charge and current densities are

$$\eta = -\frac{\mathrm{x}' \cdot H_0}{\pi\sqrt{a^2 - \mathrm{x}'^2}} \ , \ K = K_m + K_E = \frac{1}{\pi^2}\left(ik\sqrt{a^2 - \mathrm{x}'^2}H_0 + \frac{\mathrm{x}' \times E_0}{2\sqrt{a^2 - \mathrm{x}'^2}}\right). \qquad (2.7)$$

The field distribution of the diffracted wave can be directly calculated from given charge and current density: $\varphi_0 = e^{ikr}/r$,

$$E(\mathrm{x}) = \int K(\mathrm{x}') \times \nabla \varphi d\sigma = \frac{1}{3\pi} k^2 a^3 \varphi_0 \kappa \times (2H_0 + E_0 \times \kappa), \tag{2.8}$$

$$H(\mathrm{x}) = \int (ikK(\mathrm{x}')\varphi - \eta(\mathrm{x}')\nabla\varphi) d\sigma = -\frac{1}{3\pi} k^2 a^3 \varphi_0 \kappa \times (2H_0 \times \kappa - E_0). \tag{2.9}$$

Here κ is a unit vector of displacement, and φ is approximated to be $\varphi = \varphi_0(1 - ik\kappa \cdot \mathrm{x}')$.

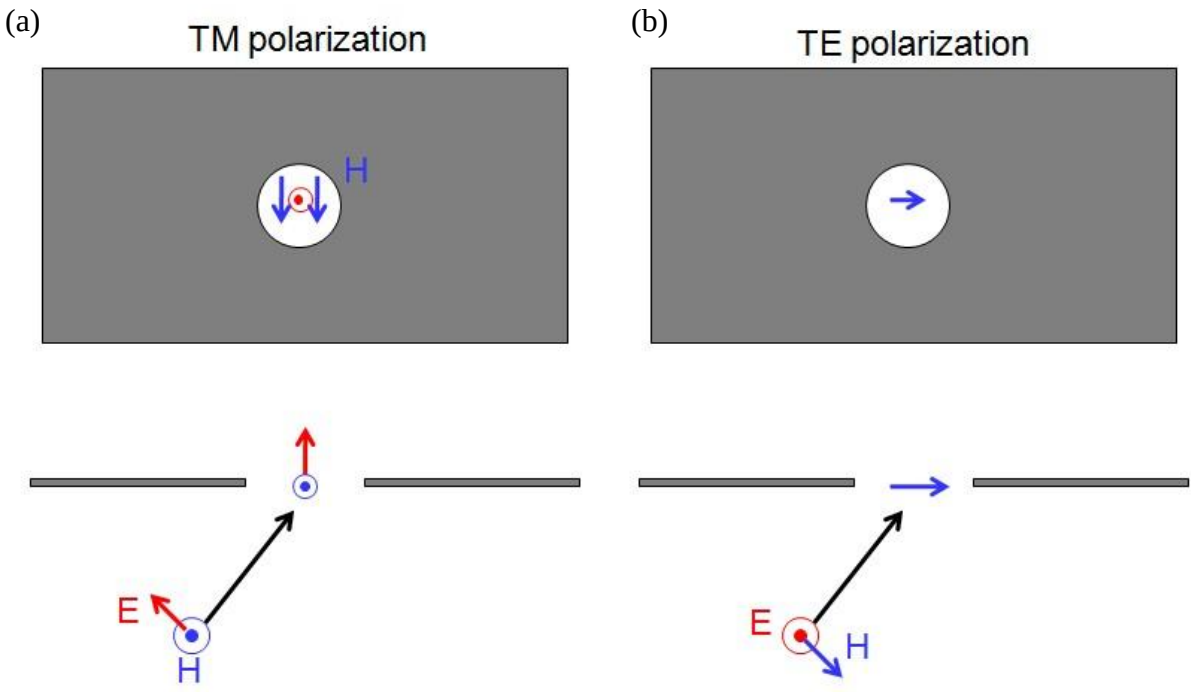

Figure 2.2 Dipole representation of diffraction through a subwavelength hole (a) TM polarization: diffracted field is represented by the radiation from a fictitious horizontal magnetic dipole and vertical electric dipole. (b) TE polarization: diffracted field can be described by the radiation from a fictitious horizontal magnetic dipole.

In fact, this field distribution (see Fig. 2.2) is exactly same as the radiation from in-plane magnetic dipole and vertical electric dipole inside the hole, as given in the following equations:

$$P = -\frac{1}{3\pi} a^3 E_0 \ , \ M = -\frac{2}{3\pi} a^3 H_0 . \qquad (2.10)$$

Essentially, in-plane magnetic dipole and normal electric dipole are generated in the hole, which can be easily seen to satisfy the boundary conditions.

The total cross section of a single hole is calculated by integration of the Poynting vector:

$$S_{tot} = \frac{c}{27\pi^2} k^4 a^6 (4{H_0}^2 + {E_0}^2) .$$

When normalized to a unit area with normal illumination, $T = \frac{64}{27\pi^2} k^4 r^4$.

2.3. Extraordinary Transmission

With recent advances of technology in nanoscale fabrication, it is now possible to fabricate structures of subwavelength size at optical frequencies. T.W. Ebbesen first reported an experimental observation of transmission through subwavelength holes at optical region in 1998. Surprisingly, the transmission through a subwavelength hole is three orders of magnitude larger than what is expected by Bethe's theory [65]. As is shown in Fig 2.3 (a), there are strong transmission peaks where the periodicity of the array matches with that of surface plasmon polaritons (SPPs), suggesting resonant excitation of SPP has a significant role in transmission. It was again confirmed that the transmission is very sensitive to the wavelength, but the physical nature of the surface mode that contributes to the transmission is still not clear [11,52,54,66]. In fact, the enhancement of transmission was observed even for randomly spaced structures [67] or for a single hole [52]. Since most of the experiments were done with array of holes or slits, there are ambiguities caused by the inherently collective nature of such phenomena. For example,

there are issues with grating effects, an effective SPP wavelength, normalization, size effects of the array, etc. In particular, while the collective phenomenon is relatively well studied [52,65,66], it is not clear what is exactly happening in the single hole case,

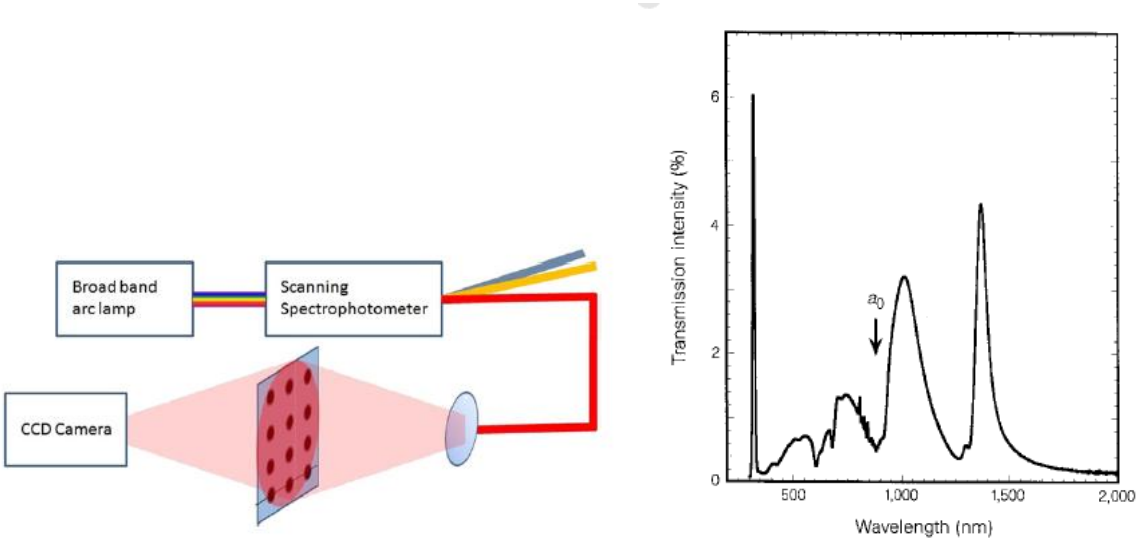

Figure 2.3 (a) Schematic describing experimental setup of transmission measurement. (b) Transmission spectrum shows sharp peak when the SPP wavelength matches the array periodicity.

2.4. Experimental Setup: Near-field Scanning Optical Microscope (NSOM)

Issues regarding the ambiguities of collective phenomenon can be avoided by focusing on a single hole. To validate or disproof Bethe's theory, it is required to investigate both spatial field profile and phase information as well as transmittance, which is challenging due to the resolution limit of conventional optical microscopes and the sensitivity required for phase measurements.

To achieve the necessary optical resolution, a home-built near-field scanning optical microscope (NSOM) is employed to probe local E-field distribution; to gather the necessary information, a few modifications that are different from conventional NSOM system were made.

As discussed below, experiments are performed in various modes depending on the purpose of the measurement.

In the case of phase measurement of light transmitted through a subwavelength hole, the experimental setup is the transmission-mode NSOM, shown in Fig. 2.4 (a). A thin metal film was intentionally used in order to provide a small amount of attenuated light, which provides a phase contrast. Typically, the background is attenuated down to 1-3%, depending on the metal thickness and the optical wavelength. As a result, we observe an interference pattern from which we can extract both phase and intensity information. To map the optical intensity along the vertical plane, i.e., to measure the height dependence of the optical intensity, the optical probe is slowly lifted during the NSOM measurement while simultaneously scanning the probe horizontally, as shown in Fig. 2.4 (b). This method produces images of the vertical plane (XZ), as shown in Fig. 2.7 (a).

Finally, a prism is used to provide evanescent excitation of the sample, which is sometimes useful in the case where additional momentum is required to excite plasmonic modes, or when one desires suppressed background noise during the measurement. (See Fig.2.4 (c).)

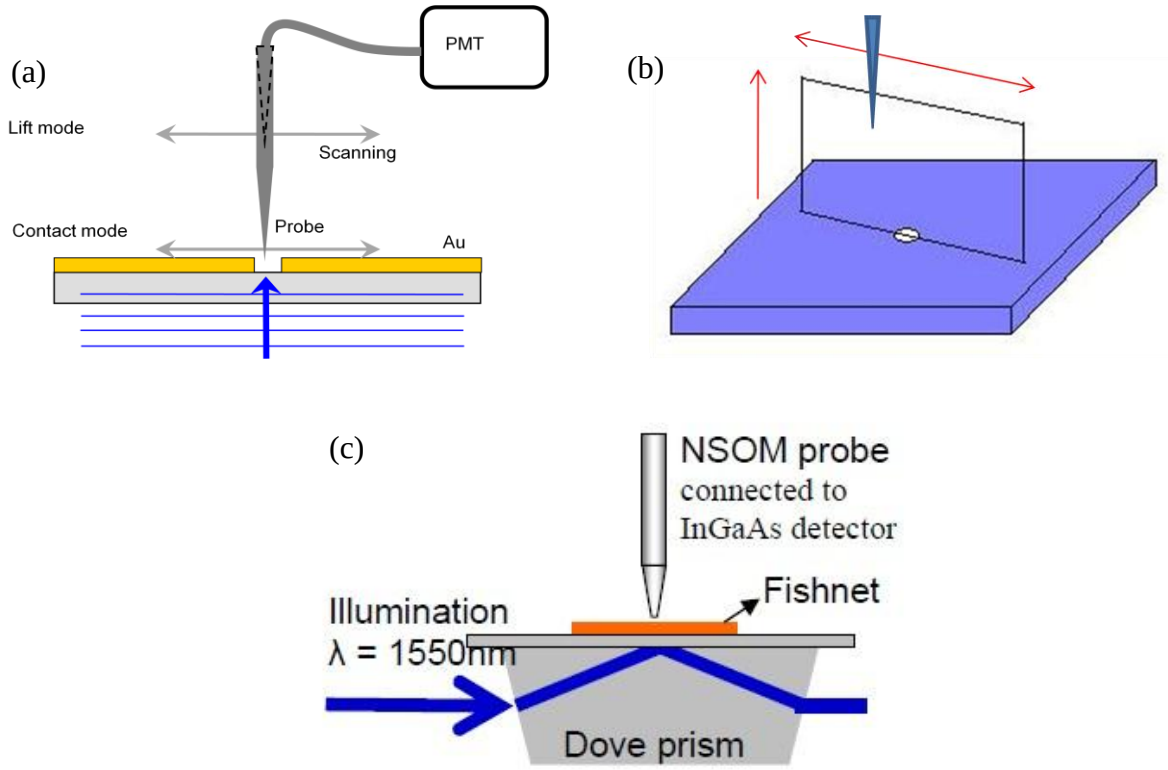

Figure 2.4 (a) Transmission-mode NSOM system. An optical probe is scanned over a horizontal imaging plane. The probe is either contacting the sample surface or lifted to a certain height. (b) XZ scanning system. NSOM probe is scanned over the vertical imaging plane. (c) Total-Internal-Reflection (TIR)-mode NSOM system: a sample is placed on top of a dove prism with index matching oil filled in between the sample and dove prism. The sample is excited by the evanescent field, and the resulting excited field is scattered by the optical probe and collected through the fiber.

2.5. A Subwavelength Hole in a Thin Metal Film

The experiments are done on different thicknesses (40nm to 120nm) of Au films sputtered onto 300μm fused quartz substrates by electric beam evaporation. Isolated holes of different diameter (100nm to 500nm) are created by focused ion-beam (FIB) milling. A near-field scanning optical microscope is used to measure the optical intensity distribution around the hole, not only on the surface of the Au film, but also a certain distance (within few microns) away from the surface. (See Fig.2.4(a).) The samples are normally illuminated from the substrate

by a laser beam from a multi-line laser, that can be treated as plane wave illumination. In the experiment, 482nm, 530nm, and 647nm laser lines from a krypton laser are chosen to illuminate the samples. Fig. 2.5 shows the pattern of optical intensity distribution measured on the sample containing a 300nm isolated hole on a 120nm thick film. Concentric rings with a dark spot in the center are observed in the lift mode image, which cannot be explained by the diffraction theory of tiny hole.

To analyze this more quantitatively, we use a simple model that a spherical wave $E_{spherical} = B\exp(ikr + i\phi)/(kr)$ from a point source is interfering with background plane wave $E_{plane} = A\exp(ikz)$. The resulting predicted interference pattern is then,

$$I(z,\phi) = (E_{plane} + E_{spherical}) \times (E_{plane}^{*} + E_{spherical}^{*}) = A^2 + \left(\frac{B\cos\theta}{z}\right)^2 + 2AB\frac{\cos\theta}{z}\cos[(kz - \frac{kz}{\cos\theta}) - \phi] \cdot$$

At $\theta = 0$, which means in the center of the interference pattern, the intensity is dominated by the phase shift φ. Systemic experiments are done by using various thicknesses of Au thin film and illuminated wavelengths to investigate the behavior of light propagating in a subwavelength isolated hole.

Focusing on 120nm thick Au film with isolated 300nm diameter hole sample, the intensity distribution illuminated by 482nm laser line on different heights were measured by NSOM setup. Fig 2.5 (a)-(d) insets show the NSOM optical images measured at heights 500nm, 750nm, 1μm, and 2μm, respectively. The intensity profiles plotted in Fig. 2.5(a)-(d) in dots are calculated by integrating the optical intensity at same distance away from the center. Observe that, as the measurement height increases, the radii of rings becomes larger and larger, but the center part remains dark.

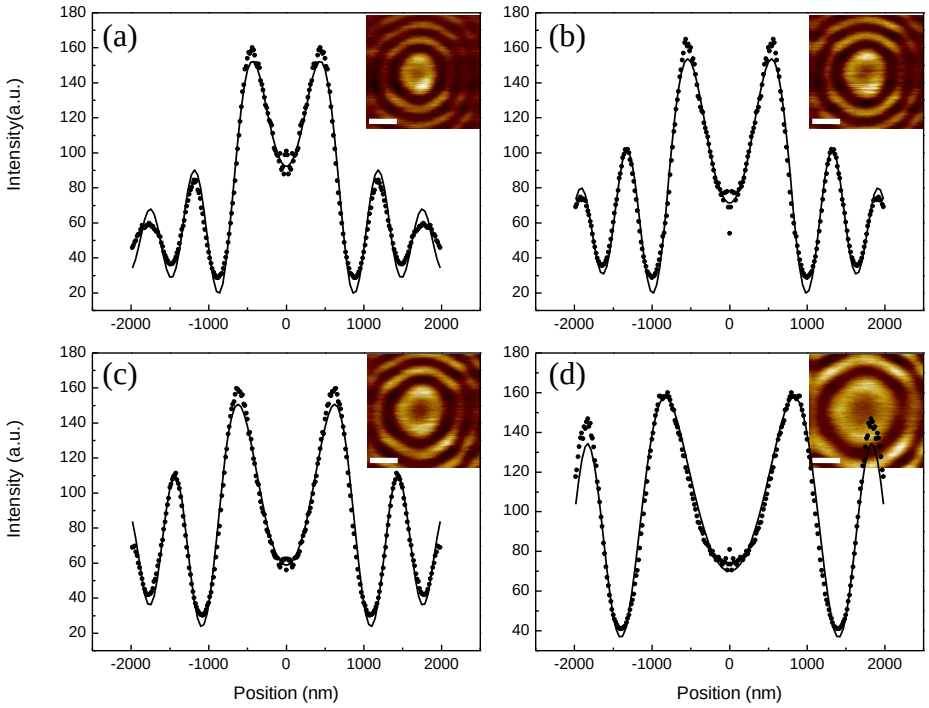

Figure 2.5 Experimentally measured interference patterns (dots) compared to the calculation from simple model. (a)-(d) The 300nm diameter isolated hole on 120nm thickness Au film is illuminated by 482nm light. The insets are NSOM optical images measured at heights of 500nm, 750nm, 1μm, and 2μm, respectively. The intensity profiles obtained from the corresponding NSOM images are plotted in dots and nonlinear fitting curves are drawn in line. The scale bar in the image is 1μm.

The experimental intensity profiles are fit with a non-linear curve, with *A*, *B*, *z* and φ as fitting parameters. The fitted profiles, drawn in solid lines in the corresponding figures, match the experimental data very well. Therefore, the model that the intensity pattern comes from the interference of a plane wave and a spherical wave seems to correctly describe this isolated subwavelength hole system for the four heights of 500nm, 750nm, 1μm, and 2μm. The retrieved phase shift φs are 89.9 º, 101.9 º, 109.8 ºand 110.0 º, respectively. Note that although the measurement height *z* can be controlled somewhat in the experiment, however, the actual height is not as accurate as input, so the height is also a variable parameter in the non-linear fitting process. The retrieved height is around 10% higher than the input value, which is reasonable

given the NSOM height control system.

The phase difference due to light passing through the metal thin film and same thickness of air layer is also considered by calculating the phase change at both interfaces (Au-quartz and Au-air) and the optical path through the thin film. Varying the thickness of the Au thin film from 0 to 120nm, the phase difference is within 10 degree for 482nm, which is not a dominant contribution to the phase shift between the transmitted and diffracted waves. The phase difference for different illumination wavelengths on Au film with various thicknesses is plotted in the Fig 2.6 inset. The frequency-dependent permittivity for Au is from Palik [68].

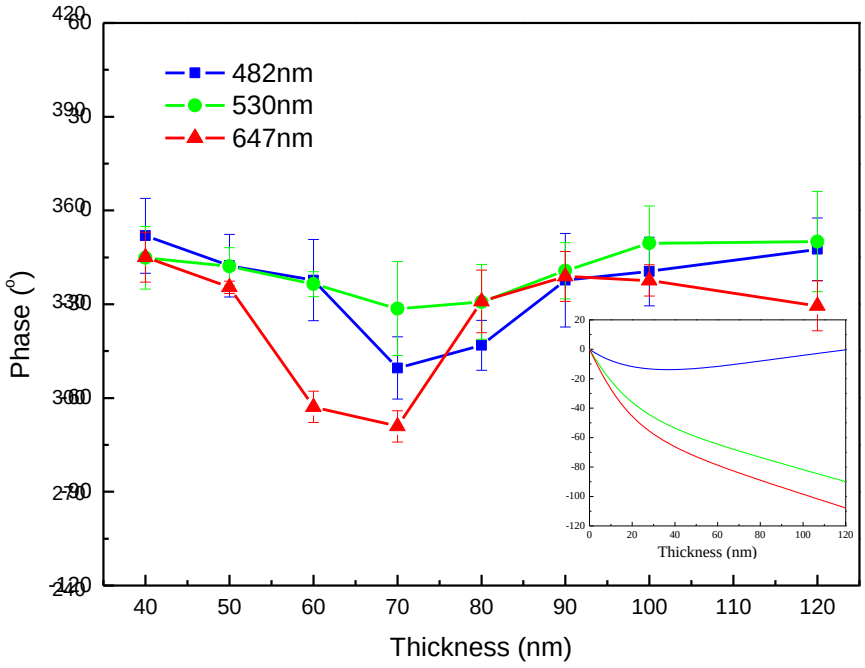

Figure 2.6 Experimentally measured phase difference of incident and diffracted waves for a 300nm isolated hole on a Au thin film with various thickness and wavelengths of illumination. The figure inset is the analytically calculated phase difference between light passing through the varied thickness of Au thin film and corresponding thickness of air.

Using different illumination wavelengths, we used an NSOM setup to measure the optical

intensity distribution of light through a subwavelength isolated hole on different Au film thicknesses. The phase shift for each case is retrieved by nonlinear fitting analysis. Usually people are most interested in the phase difference between the incident wave and excited diffracted wave. In the experimental data analysis, the retrieved phase from non-linear fitting is the phase difference between the transmitted and diffracted wave, whereas the phase retardation of the transmitted wave can be analytically calculated. By subtracting this component, the phase difference between the incident and diffracted wave can be achieved, as shown in Fig 2.6. The error bars are due to the variation of retrieved phase shift at different measurement heights. It can be seen that the phase shifts for different illumination wavelengths are almost same; however, the values are much different from Bethe's or Kirchhoff's model, which both use the perfect electric conductor assumption. In a real experimental case, the surface plasmon polaritons on the metal and dielectric interface driven by the external field, modulate the radiation phase of the spherical wave. According to the calculation of cut-off frequency in cylindrical waveguide, there is no guided mode in such small subwavelength holes, so that diffracted waves must come from the coupling of the SPPs at both interfaces.

The cross sectional intensity distribution was also measured by the NSOM and is shown in Fig. 2.7 (a). In the experiment, a 300nm isolated hole on 80nm Au thin film was illuminated by a 482nm laser line. The optical image clearly shows the radii change of the different order of the interference pattern due to the interference of the plane wave and spherical wave. Full wave numerical simulation based on finite difference time domain method were used to simulate the isolated hole on the Au metal thin film. The simulated intensity distribution of the cross section is plotted in Fig. 2.7 (b). The colored symbols in the figure are the peak positions of the measured intensity profiles at different measurement heights; these show good agreement with

the simulation results.

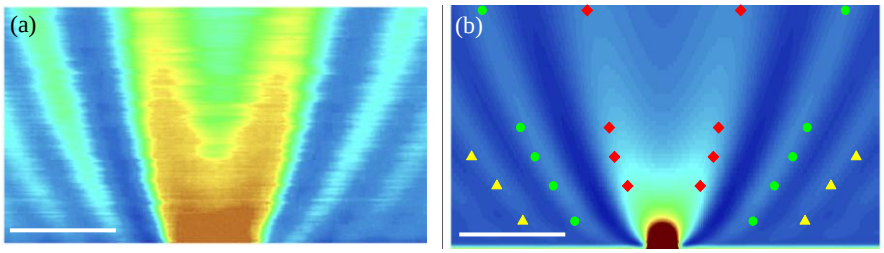

Figure 2.7 (a) 300nm-wide isolated hole on 80nm-thick Au thin film is illuminated by 482nm laser light. Cross sectional intensity distribution is recorded by NSOM vertical scanning. (b) Simulated cross sectional intensity distribution by FDTD. The colored symbols show the peak position captured by the intensity profile analysis at different heights. The scale bar is 1μm.

From the FDTD simulation result, we see that an electrical dipole moment near the hole is excited by the external electric field. The diffracted wave can be treated as the radiation of this dipole moment, which determines the phase of the diffracted wave. In the data analysis, we assumed the diffracted wave is a spherical wave, that is, we approximate the dipole radiation by ignoring higher order terms. Since the measurement position is a fairly large distance away from the dipole moment, the radiation pattern described by a spherical wave is a good assumption. The phase of the dipole moment can be modified by changing the structure of subwavelength scatter. Considering an isolated dent and equal-size disk on the same thickness Au thin film (see Fig. 2.8 (c)), due to the external electric field, the electrons accumulate near the subwavelength structure, as indicated in the figure. It is straightforward to observe the excited dipole moment is just reversed. The phase difference between these two cases should be 180 º. Experimentally, on same Au film with 100nm thickness, an isolated dent with 300nm diameter and 40nm depth was milled by FIB, while a disk with same size and 40nm height was fabricated by e-beam lithography. The intensity distribution measured by NSOM 1μm away from the top surface for dent and disk cases is shown in Fig. 2.8 (a) and 2.8 (b), respectively. The samples are illuminated

by 482nm laser line. The two intensity distributions show almost the inversed interference pattern, that means the direction flipped in the dipole moment. Same data analysis method is applied to these two cases by measuring the intensity profiles at different heights, and retrieved phases for dent and disk case are 3.4 ºand 189.8 º, respectively. The difference between these two cases is around 180 º, thereby verified our dipole moment assumption of phase.

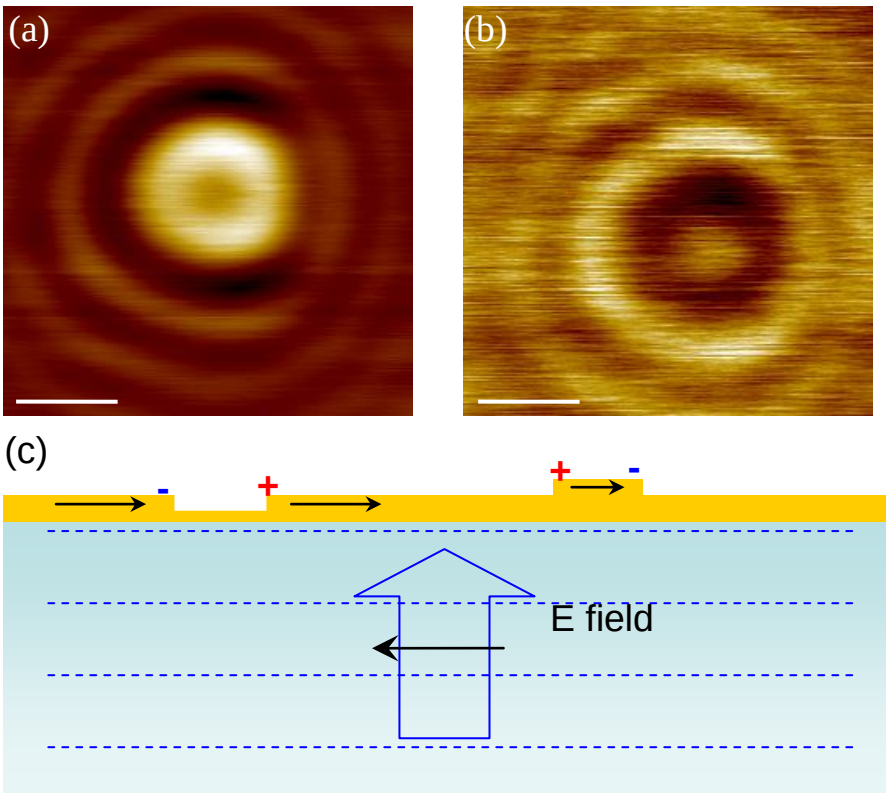

Figure 2.8 (a) and (b) NSOM optical images of isolated dent and disk on the Au thin film at 1μm height. (c) Sketch of electric field direction and induced charge accumulation near the isolated dent and disk on the thin Au film. The scale bar is 1μm.

The first assumption of Bethe's theory is that the screen is made of perfect conductor. In reality, the skin depth of metal is between 10-40nm depending on the wavelength at optical frequency and therefore a tangential electric field is no longer forbidden on the screen within the skin depth range. This give rises to an in-plane electric dipole component which contributes to

the transmission along with other two dipole terms. The interference pattern with illumination with certain angle of incidence can better fit the experimental results by adding an in-plane electric dipole contribution which, in fact, is even larger than the other two contributions. Of course, this explains why we observe stronger transmission since we have an additional channel of transmission.

To investigate the contribution of in-plane electric dipole, the angular dependence of the illuminating light is studied. According to the Bethe's theory, the radiation profile depends on the polarization of illuminating light. When the hole is illuminated by TE polarized light, we only have projected in-plane magnetic dipole, which will not change the radiation profile. In contrast, for TM polarized light, there is a vertical electric dipole that comes into play and tilts the maximum radiation direction toward the direction on incident wave as shown in Fig. 2.2.

Since our system measures the interference between diffracted and attenuated wave, the contribution from direct transmission through metal film should also be considered. The position of the intensity peak is calculated and compared with experimental results. The estimated peak shift for TE and TM polarization based on Bethe's theory is 912 and 816nm respectively. Experimentally, the measured values are 820nm and 840nm, respectively, with approximate error ranges of 20nm. Such discrepancy is mainly due to the contribution of in-plane electric dipole as is discussed in Fig. 2.8. The ratio of dipole contribution from in-plane electric dipole and magnetic dipole can be extracted by fitting the peak position measured by experiment with theoretical calculation. The result indicates the contribution of in-plane electric dipole is 4.3 times larger than that of magnetic dipole with illumination wavelength of 482nm.

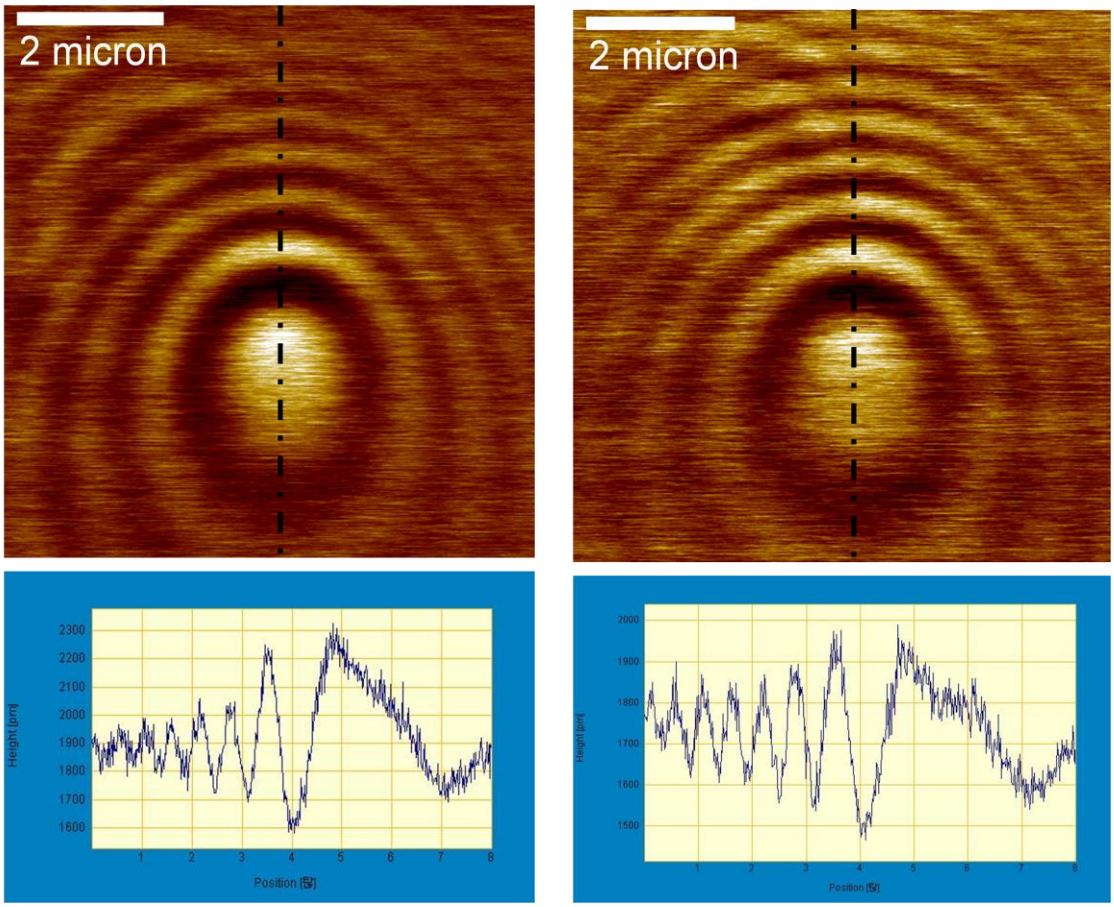

Figure 2.9 Interference pattern with light illumination with 30 degrees angle of incidence. (a) The polarization of incident wave is TE. (b) The polarization of incident wave is TM.

The control of phase in light is traditionally done by increasing or decreasing the optical beam path in the application such as an interferometer and a modulator, which require rather bulky optical components. Subwavelength hole arrays, shown in Fig. 2.10 (a), can be used to control the phase of transmitted light with its phase dependent on the density of holes in the array. It is demonstrated that the region with higher density of subwavelength holes is darker in terms of optical intensity. Such effect is due to the destructive interference between light transmitted through holes and light transmitted through a thin metal film. It is possible to control the average phase of transmitted light by changing the density of holes. An effective control of phase by such a simple planar structure would be advantageous in applications such as

holography.

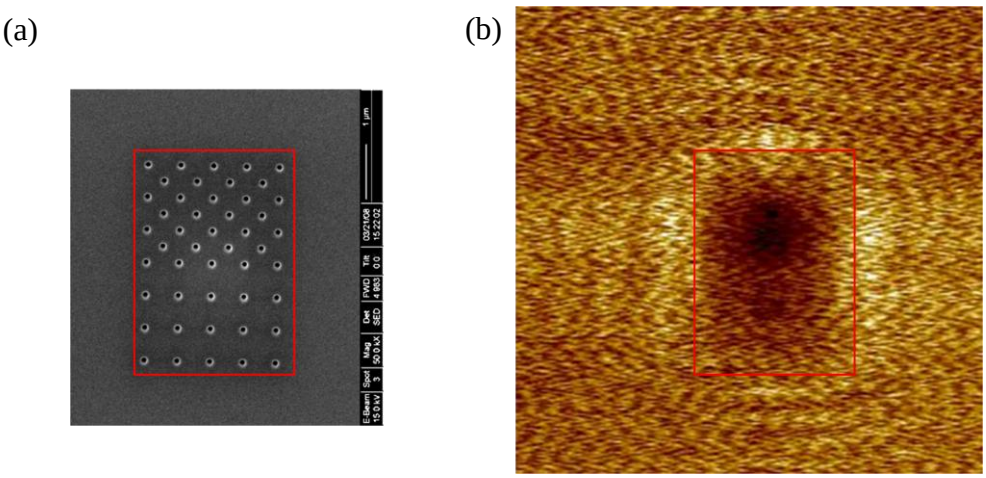

Figure 2.10 (a) SEM images of subwavelength hole array. Diameter of each hole is 100nm and the spacing between holes is 600nm on the sparse side, and 424nm on the denser side. (b) NSOM optical image of hole array with probe to sample distance fixed at 500nm. Optical intensity is weaker if hole array is denser.

2.6. Subwavelength Holes in a Fishnet Metamaterial

In the previous chapter, light transmission through a subwavelength hole in a thin metal film is studied. The surface modes on the metallic film affect the phase and intensity of light transmission through a subwavelength aperture. One interesting case is when the metallic film is replaced by a planar metamaterial. In this chapter, light transmission through a few subwavelength holes in a fishnet metamaterial is measured at the wavelength where the optical index of the fishnet metamaterial is near zero. Due to the near-zero phase change through the metamaterial, a spatial broadening of transmitted light is observed.

A point spread function (PSF), which is a measure of responses from a point light source, characterizes the resolution of an optical component. It was used to study the near-field imaging

of a point dipole by using a lossy metamaterial slab, demonstrating the ability of subwavelength resolution [69]. In addition, it is also a powerful tool to determine the interaction of a point source with the slab of metamaterial in the near-field region [70].

The PSF forms the basis for an optical imaging. Assuming linearity, an image of a random object can be constructed from the PSF using the convolution integral:

$$I(x_i, y_i) = \iint O(u, v)\mathrm{PSF}(x_i - Mu, y_i - Mv)dudv, \tag{2.11}$$

where (u, v) is the position of the source, and M is the magnification of the system, which is unity in our case. The PSF can be directly obtained by measuring the response of a point like object or a source, as can be seen from equation (2.11) by replacing $O(u, v)$ with Dirac delta function. However, since the actual system uses a finite-sized aperture instead of an ideal point source, we have performed full wave simulation with an aperture with finite size. By assuming Gaussian profile for both incident and transmitted beam, we have extracted the PSF from the result, which is represented by:

$$\mathrm{PSF}(x - u, y - v) = A\exp[-\frac{(x-u)^2+(y-v)^2}{2B^2}], \tag{2.12}$$

where A is a constant for the amplitude, and B is the width of the distribution. By fitting the measured intensity profile with this equation, the parameters can be retrieved to determine the broadening effect of light from the point source through the fishnet optical modulator.

To perform an experimental study, we have designed and fabricated a fishnet modulator. A series of e-beam evaporation of 50nm Cr / 30nm SiO_2 / 28nm Ag / 50nm SiO_2 / 28nm Ag was done on a glass substrate. Here Cr layer, which is opaque from visible to near IR range, serves as a mask to block direct transmission. The first SiO_2 layer works as a spacer, while the second SiO_2 is a dielectric layer sandwiched by two metal layers forming LC resonant circuits. Focused ion beam (FIB) milling is done to make both the fishnet structure and the aperture. The lattice

constant of the fishnet is 600nm and the width of vertical and horizontal wires are 125nm and 325nm, respectively. The fishnet metamaterial with such dimension parameters has a magnetic resonance wavelength near 1.55μm, which is confirmed by the spectrum measurement shown in Fig. 2.11 (b). It is noted that the spectrum shown here was measured on a control sample with same dimensional parameters but without Cr layer. The point source was fabricated by FIB milling of a deep aperture all the way through the Cr mask layer at the designed location, while remaining area of fishnet pattern is milled only through Ag-SiO_2-Ag layers. The sketch of the cross section for the fishnet sample is shown in Fig. 2.11 (a). The size of individual aperture is 475nm x 275nm, which is exactly one opening on the fishnet, and the overall 2 x 2 adjacent apertures were drilled to achieve the necessary signal to noise ratio. The reason to have multiple holes is to improve the signal to noise ratio, and it is noted that the total size of the aperture is still subwavelength, compared to the operation wavelength.

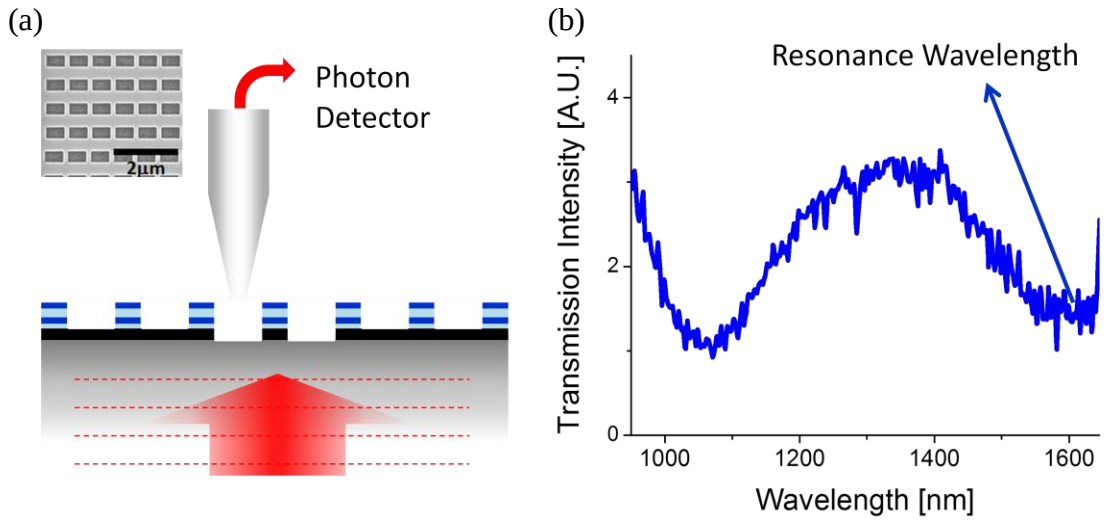

Figure 2.11 (a) Schematic view of the experimental setup. The sample is illuminated from the bottom, and the NSOM probe collects scattered near-field from the top surface of the fishnet metamaterial. The black layer indicates the Cr layer which serves as a mask, and the blue and light-blue layer represent Ag and SiO2 layers of the fishnet. The inset is the SEM image of the corresponding fishnet structure. Scale bar is 2μm. The aperture is made of 2x2 hole array to ensure the necessary signal to noise ratio. (b) The measured spectrum of the fishnet metamaterial shows that the resonance wavelength is around 1.55μm.

As shown in Fig 2.11 (a), Near-field scanning optical microscope (NSOM) running in transmission-mode was employed to measure the PSF of light transmitting through the aperture. The measurements were done at both visible and IR wavelengths, which represent pump and probe beam respectively. Kr laser line at 482nm and semiconductor laser diode at 1.55μm, which are off-resonance and on-resonance wavelengths respectively, were used to illuminate the sample. The fishnet metamaterial with Cr mask was illuminated from the bottom. The subwavelength opening on the Cr layer serves as a point light source. The NSOM probe scans over the sample around the aperture and collects the scattered near-field, monitoring how the point light source interacts with fishnet structure at different frequencies.

The near-field intensity distribution captured by the NSOM at 482nm and 1.55μm (two polarization directions) are shown in Fig. 2.12 (a), (b) and (c) by using pseudo-colors. The line intensity profiles along the vertical and horizontal directions which are indicated by dashed lines in Fig. 2.12 (a), (b) and (c) are plotted in Fig. 2.12 (d), (e) and (f), respectively. At the pump wavelength with electric field along the vertical wire, the full width at half-maximum (FWHM) of the intensity profile is around 1.7 μm, which is calculated from the measured data with the assumption of Gaussian profile. It is mentioned that the beam broadening is partly due to the NSOM probe itself since an uncoated fiber was used as the NSOM probe in the experiment to ensure the good signal to noise ratio. Also, some of the broadening effect can also be attributed to the excitation of surface modes and scatterings, as we can see in the optical image. For the electric field along the horizontal wire, a similar result was observed. However, at the probe wavelength which is close to the resonance of the fishnet metamaterial, the result is quite different and shows strong dependence on the polarization. Here one polarization excites fishnet

mode (when E-field is aligned along the vertical wire) while the other one cannot and therefore serves as a control experiment. The measured FWHM of the PSF for each case is 6.9μm and 3.4μm, respectively.

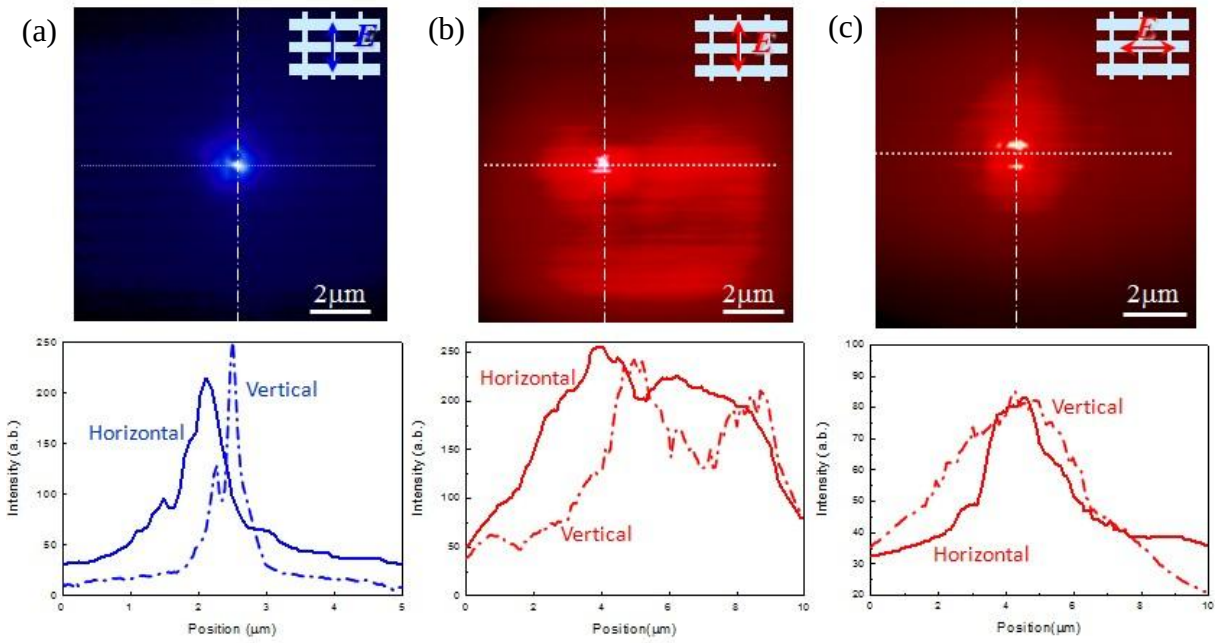

Figure 2.12 Upper row: the NSOM images at (a) 482nm, and (b),(c) 1.55μm. The insets indicate the direction of the electric field applied to the fishnet structure. Lower row: the corresponding intensity profiles along the vertical and horizontal direction. It is noted that the Cr mask layer is thick enough to block the direct transmission other than through-aperture transmission, so it does not show any interference fringes which were shown in Fig. 2.5 and Fig. 2.8.

The broadening of the point source is mostly due to the interaction of the electromagnetic wave and the fishnet structure. A simple 2-dimensional simulation is done to explain such effect at off-resonance and on-resonance wavelengths by assuming the fishnet structure as a thin homogeneous layer with an appropriate effective refractive index [71]. The finite element method based commercial software, COMSOL Multiphysics, was used to calculate the field distribution. A 30nm-thick Cr layer followed by a 96nm-thick metamaterial layer was set on the

top of the SiO_2 substrate. An aperture with 900nm width was opened on the Cr layer. The structure was illuminated by the TM mode plane wave from the bottom at the off- and on-resonance wavelengths. The electromagnetic parameters for Cr and SiO_2 are taken from Palik [68], while the effective index of fishnet metamaterial is from Ref [71]. Due to the limited availability of the effective index in the reference, the off-resonance wavelength in the simulation was chosen to be 1.3μm with the effective index of 1.0+0.01i. The field distribution with the corresponding intensity profile at 50nm above the metamaterial layer is plotted in Fig. 2.13 (a) and (b). It is noted that, in the experiment, we chose 482nm for the off-resonance wavelength due to the limited availability of the laser source. Since the wavelength is far away from the resonance of the fishnet metamaterial, the effective index is similar to the one we used in the simulation.

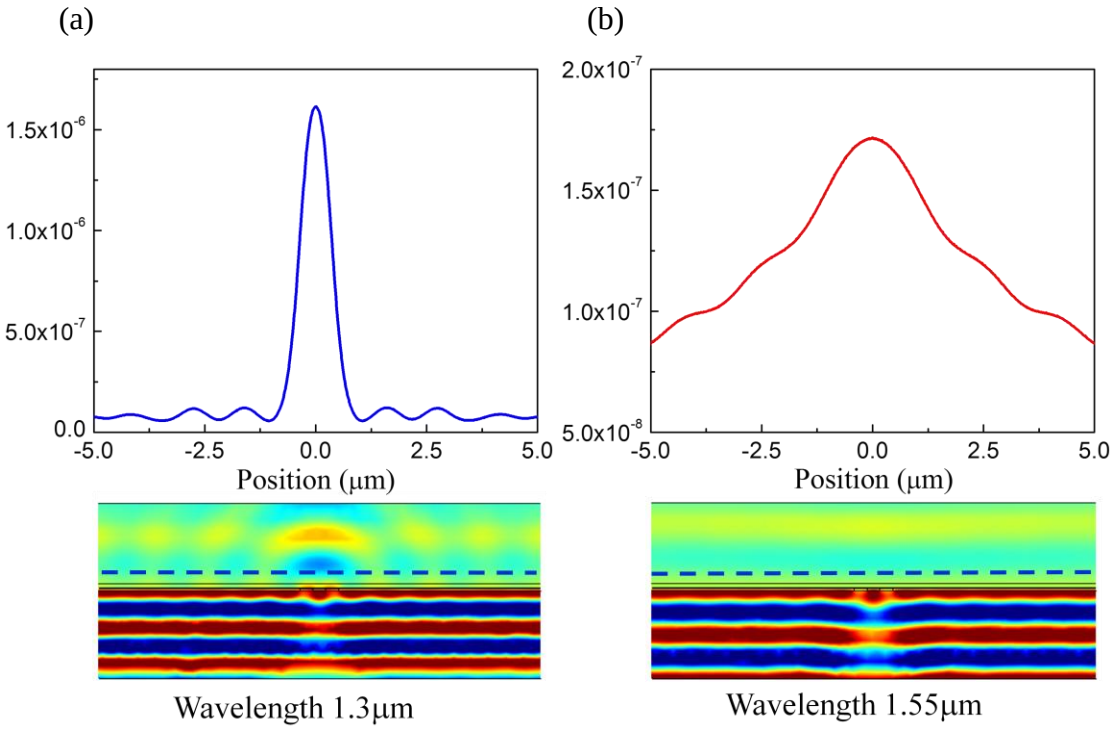

Figure 2.13 (a) The field distribution (lower) with the corresponding intensity profile at 50nm above the metamaterial layer (indicated by the dashed line) at off-resonance wavelength (1.3μm) (b) the field distribution (lower) with the corresponding intensity profile at on-resonance wavelength (1.55μm).

Therefore, the simulation result at 1.3μm can represent the physics of the electromagnetic wave interacting with the fishnet metamaterial at off-resonance wavelength. After the Gaussian fitting of the intensity profile, the FWHM is measured to be around 1μm, which is similar to the size of the opening on the Cr mask. When the wavelength of incident light is tuned to 1.55μm, which is very close to the resonance wavelength of the fishnet metamaterial, the real part of the effective index is near zero. In the simulation, 0.01+0.05i was chosen for the metamaterial layer. The field distribution and the corresponding intensity profile are plotted in Fig. 2.13 (a) and (b). The calculated FWHM is around 5μm. The broadening of the point source is mainly due to the resonance of the fishnet metamaterial. Near the resonance wavelength, the effective index is close to zero which means the phase of the electromagnetic wave inside the metamaterial remains same as it propagates. And the wave will radiate out in phase at the interface, so that a broad spatial profile is formed even though it is excited by a subwavelength light source. It is noted that the experimental measurement shows an even broader profile, which is due to the surface mode and inhomogeneity of the fishnet which are not considered in the simulation.

According to the experimental measurement and numerical simulation, it is clearly observed that the off-resonance beam (pump beam) maintain its beam size when transmitted through the fishnet, while the on-resonance beam (probe beam) broadens significantly. Assuming the width of the probe beam is 5μm in real application, which is around 3λ at the telecommunication wavelength, the beam size on the other side will be around 8.5μm according to the equation (2.11) and (2.12). This sets the size limit of fishnet device functioning as an optical modulator, which is only about 5-6 times of the operating wavelength. It will

significantly reduce the spatial dimension and required energy for operation of the optical modulator.

2.7. Summary and Conclusion

The phase retardation through an isolated subwavelength hole on a metal thin film has been experimentally studied by analyzing the interference pattern captured by the NSOM. The large phase shifts cannot be explained by previous theoretical model. An in-plane electric dipole moment excited by the external field which is not considered in Bethe's model should be considered for the contribution of diffracted wave. Diffraction is one of the oldest and most fundamental phenomena that were studied for more than a hundred years. Better understating of such effect is an important step in physics research. Application-wise, a subwavelength hole can be a basic unit to manipulate the interaction between light and nanostructure with possible controllability over phase and intensity. It is potentially useful for a holography or an optical metamaterial application.

Chapter 3 Optical Modulation in Metamaterial

3.1. Introduction

Conventional optical modulators are usually composed of two units: an active medium and an interferometer. The former is a material whose refractive index can be controlled by external stimulus. The index modulation in turn induces phase modulation of light that is interacting with the medium. And the latter converts the phase modulation into the intensity modulation. An active medium is modulated most commonly by the electro-optic effects, or sometimes by an acousto-optic or a magneto-optic effect. In any case, the induced change in refractive index is very small, and as a result, it requires either long interaction length in the device or a highly resonant cavity in the beam path of interferometer to provide a reasonable on-off ratio.

Metamaterial offers a capability of controlling the effective permittivity, permeability and therefore refractive index and impedance at certain frequency. With additional degrees of freedom, the response of the active medium can be improved in different ways. An active metamaterial device operating at terahertz regime was demonstrated [39]. The amount of the index change in the active medium is improved more than 16 times at telecommunication wavelengths with ultrafast response time of 1ps [48]. At optical frequencies, a fishnet metamaterial [46,47,72] is one of the most promising candidates for an all-optical modulation. The anti-parallel current flow surrounding the dielectric medium induces a magnetic resonance, achieving negative permeability. By replacing the dielectric medium by photon sensitive semiconductors, such as Si or Ge, the effective index of the metamaterial can be modulated by the external optical pump.

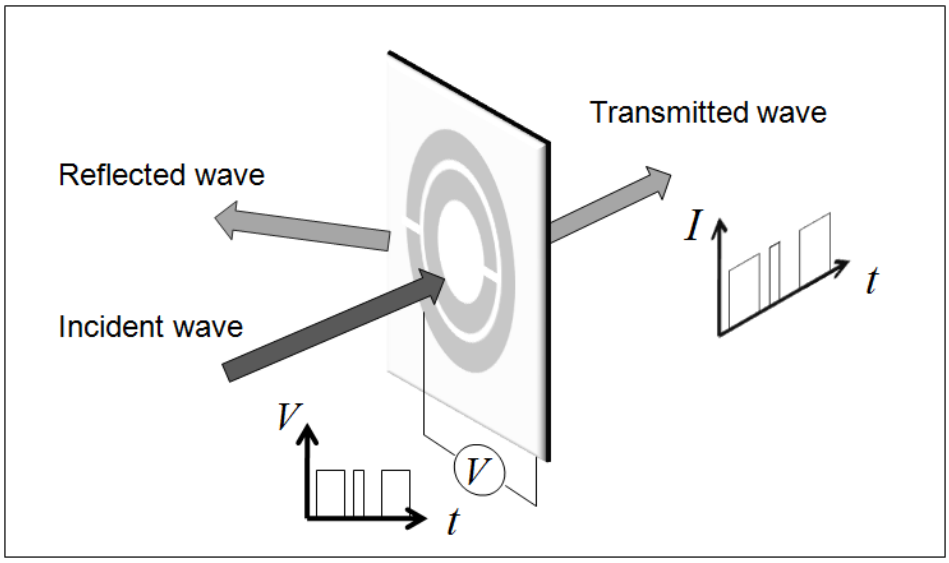

Figure 3.1 Conceptual drawing of a metamaterial based modulator

This can be understood based on the equivalent circuit modeling of a magnetic resonator. In the case of split ring resonator (SRR), the effective permeability of the metamaterial composed of LC resonators can be described by $\mu_{eff} = 1 - \frac{F\omega^2}{\omega^2 - \omega_0^{\,2} + i\omega\Gamma}$, where $\omega_0 = 1/\sqrt{LC}$. With the traditional active medium placed near the capacitive gap of SRR, an active metamaterial is built, where an external stimulus can affect the resonant frequency through the capacitance modulation. (See Fig.3.1) Researchers have been using active mediums such as semiconductors, liquid crystal, electro-optic polymer and etc. For example, when semiconductor is used, depletion and accumulation of free carriers can induce conductance change which in turn modulates capacitance, resonance frequency and then magnetic permeability. After all, transmission and reflection through metamaterial slab can be modulated by applied electric field. It is noteworthy that the active material does not necessarily interact with the light that is being modulated; rather it is controlling light

through SRR unit. Due to the resonant nature of SRR, if it is operated near the resonance wavelength, one can have a steep change in the magnetic permeability which leads to the larger index change.

In this chapter, I demonstrate ultrafast all optical modulation based on the so-called "fishnet" metamaterial at telecommunication wavelength. Detailed analysis including the LC circuit modeling and full wave simulation are done to design the effective parameters for a high performance optical modulator. The fishnet metamaterial is experimentally characterized in both near-field and far-field regime. Finally, all-optical modulation is demonstrated by using the pump-probe technique.

3.2. Modeling and Optimization of NIM Modulator

The macroscopic properties of a metamaterial can be represented by effective parameters such as the electric permittivity and the magnetic permeability [20]. In a fishnet metamaterial, at a certain wavelength near the resonance, the electric permittivity is negative due to the metallic wires parallel to the field direction and the magnetic permeability can be also negative due to the LC resonance of individual units. It is shown in a semi-analytical equation as follows.

$$\mu_{eff} = 1 - \frac{F\omega^2}{\omega^2 - \omega_0^{\,2} + i\omega\Gamma}, \text{ where } \omega_0 = \frac{1}{\sqrt{LC}} \text{ and } \Gamma = Z_s / L. \tag{3.1}$$

According to the circuit model of fishnet metamaterial [73], effective inductance and capacitance can be determined from geometrical parameters [73].

$$C \sim \frac{lw}{t}, \ \frac{1}{L} \sim \frac{w_n}{l_n t} + \frac{w_s}{l_s t}, \tag{3.2}$$

where *w* and *l* are the width and length of wire, respectively, and *t* is the thickness of dielectric layer in the unit cell (*n* and *s* indicate thicker and thinner part of the unit cell).

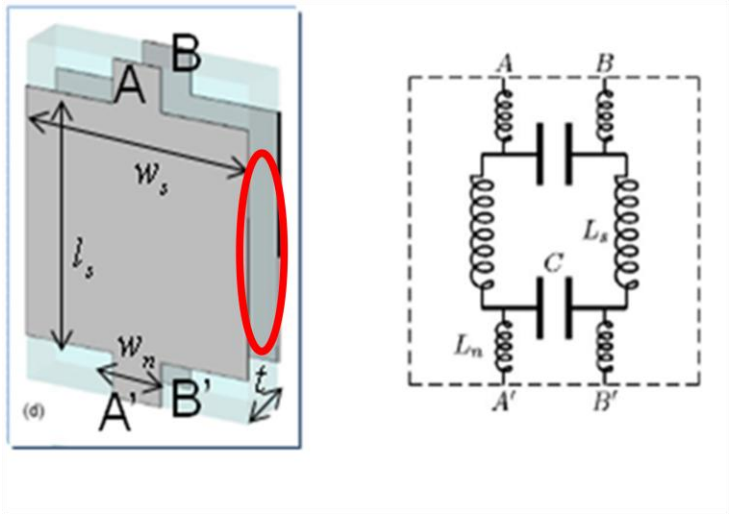

Figure 3.2 LC circuit modeling of an individual unit cell in a fishnet metamaterial [73].

With effective parameters given, transmission and reflection coefficients of a metamaterial slab is calculated using Fresnel equation,

$$T = \frac{n_1}{n_3}\left|\frac{t_{12}t_{23}e^{ikd}}{1+r_{12}r_{23}e^{2ikd}}\right|^2,\ R = \left|\frac{r_{12}+r_{23}e^{2ikd}}{1+r_{12}r_{23}e^{2ikd}}\right|^2, \tag{3.3}$$

where $k_i = \sqrt{\varepsilon_i\mu_i(\omega/c)^2 - k_x^{\,2}}$, $r_{ij} = \dfrac{k_i/\mu_i - k_j/\mu_j}{k_i/\mu_i + k_j/\mu_j}$ and $t_{ij} = \dfrac{2k_i/\mu_i}{k_i/\mu_i + k_j/\mu_j}$. ($i$ and j indicate the two medium connected at the interface.)

Assuming the change of the dielectric constant of active medium is very small, the depth of modulation is written as $\dfrac{\Delta T}{T} = \Delta\varepsilon_d \dfrac{dT}{d\varepsilon_d}\dfrac{1}{T}$. Since the effect of optical pumping is essentially a change of dielectric constant of the active medium, therefore we can model it as a change in the capacitance of the resonant LC circuit, which is proportional to the dielectric constant.

After differentiation and simplification using the fact that the thickness of metamaterial slab is very thin compared to the wavelength and the hosting medium is air, we get the modulation sensitivity equation for the transmission and reflection as follows,

$$\frac{dT}{d\varepsilon_d}\frac{1}{T} = \frac{2A}{d}\left|\frac{\omega_0^2(1-\mu_2)^2}{F\omega^2 C}\right|\left|\frac{-2r(1-e^{2ikd})}{(1-r^2e^{2ikd})(1-r^2)}\right|\left|\frac{\sqrt{\varepsilon_2}}{\sqrt{\mu_2}(\sqrt{\varepsilon_2}+\sqrt{\mu_2})^2}\right| . \qquad (3.4)$$

$$\frac{dR}{d\varepsilon_d}\frac{1}{R} = \frac{2A}{d}\left|\frac{\omega_0^2(1-\mu_2)^2}{F\omega^2 C}\right|\left|\frac{(1+r^2e^{2ikd})}{r(1-r^2e^{2ikd})}\right|\left|\frac{\sqrt{\varepsilon_2}}{\sqrt{\mu_2}(\sqrt{\varepsilon_2}+\sqrt{\mu_2})^2}\right| . \qquad (3.5)$$

It is expected from the equations that the modulation is maximized when μ is near zero and the imaginary part of μ is maximized, or $\mu \approx \varepsilon$.

The first question to be asked is where to operate the modulator. The sensitivity of the modulation upon the external pumping is plotted in Fig. 3.3(a) and (b). As shown in the graph, the highest modulation ratio is expected at the dip position of the spectrum which corresponds to the absorption peak for the transmission modulation, and most negative μ region for the reflection modulation. (See Fig. 3.3 (c)) It is expected to achieve the larger modulation ratio ($\Delta T / T$, $\Delta R / R$) when transmission or reflection is minimized, but it's not necessarily the case that the maximum change in intensity (ΔT or ΔR) takes place at the same wavelength. In fact, we observe ΔT or ΔR to be the largest where the slope in intensity spectrum is most steep, while the ratio is maximized when the intensity is the smallest. To use a metamaterial slab as a modulator in actual application, we need not just a high ratio of modulation but also a reasonable amount of energy transferred when the modulator is on. For example, the reflection dip has the highest modulation ratio but the loss of energy is too significant (>90%) to be operated as a modulator. Considering these two factors, the best position to operate a metamaterial slab modulator without any external optical component is at the absorption peak (Fig.3.3 (c)) for both transmission and reflection cases.

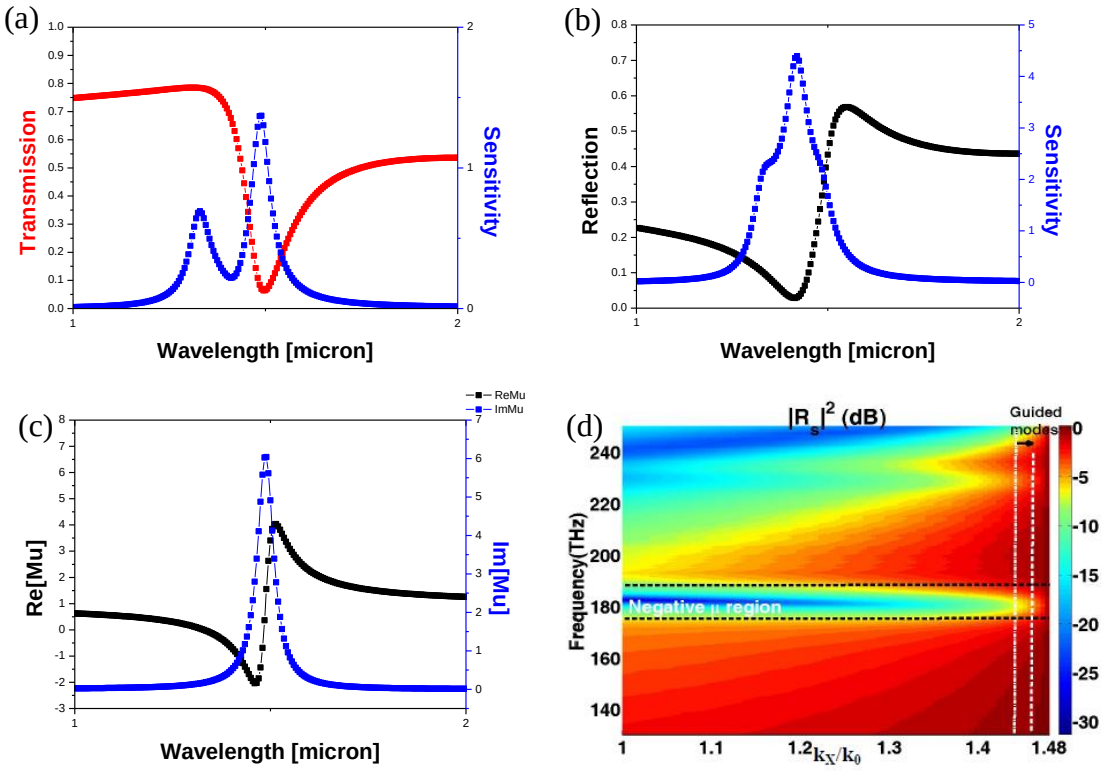

Figure 3.3 (a) Transmission and modulation sensitivity vs. wavelength, (b) the reflection and modulation sensitivity vs. wavelength, (c) real and imaginary part of the magnetic permeability vs. wavelength, (d) the modulation depth with oblique incidence ($\theta = \sin^{-1}(k_x / nk_0)$).

Even though the resonant wavelength should be fixed at around 1.55 μm, there are still certain degrees of freedom in designing the geometrical parameters and selecting the active dielectric medium for the fishnet modulator. The sensitivity of modulation is plotted versus various parameters in Fig. 3.4. First of all, the modulation depth will be significantly increased with smaller effective capacitance and therefore larger inductance in the LC resonant circuit. This is because the large inductance decreases the current and therefore reduces the ohmic loss and in turn sharpens the resonance. It can be achieved by changing the geometrical parameters in equation (3.3). The easiest way is to increase the thickness of active medium which increases the inductance and decreases the capacitance without changing the resonant wavelength. Because this model is an approximation especially at the optical wavelength range, further modification

of width is needed to correct the deviation of the resonant wavelength. There is a limitation of this approach due to the complication coming from Fabry-Perot effect as the thickness of sandwiched dielectric layer gets thicker. Since we have relatively high index Si as the active medium, the thickness is limited below 90nm to avoid the Fabry-Perot effect near the transmission dip.

The alternative way is to use low index active dielectric materials. For example, if we use a mixture of half Si and half SiO_2 instead of pure Si layer, we can effectively reduce the dielectric constant down to 60% of its original value. Even though there will be a reduction of modulation in a dielectric constant itself upon the external pumping, overall we get improved modulation depth as long as the sensitivity vs. capacitance curve is steep enough. Using the parameters in Fig.3.3 and $C = 4 \times 10^{-19} F/m$, we get 2.5 times larger modulation depth by mixing Si with SiO_2.

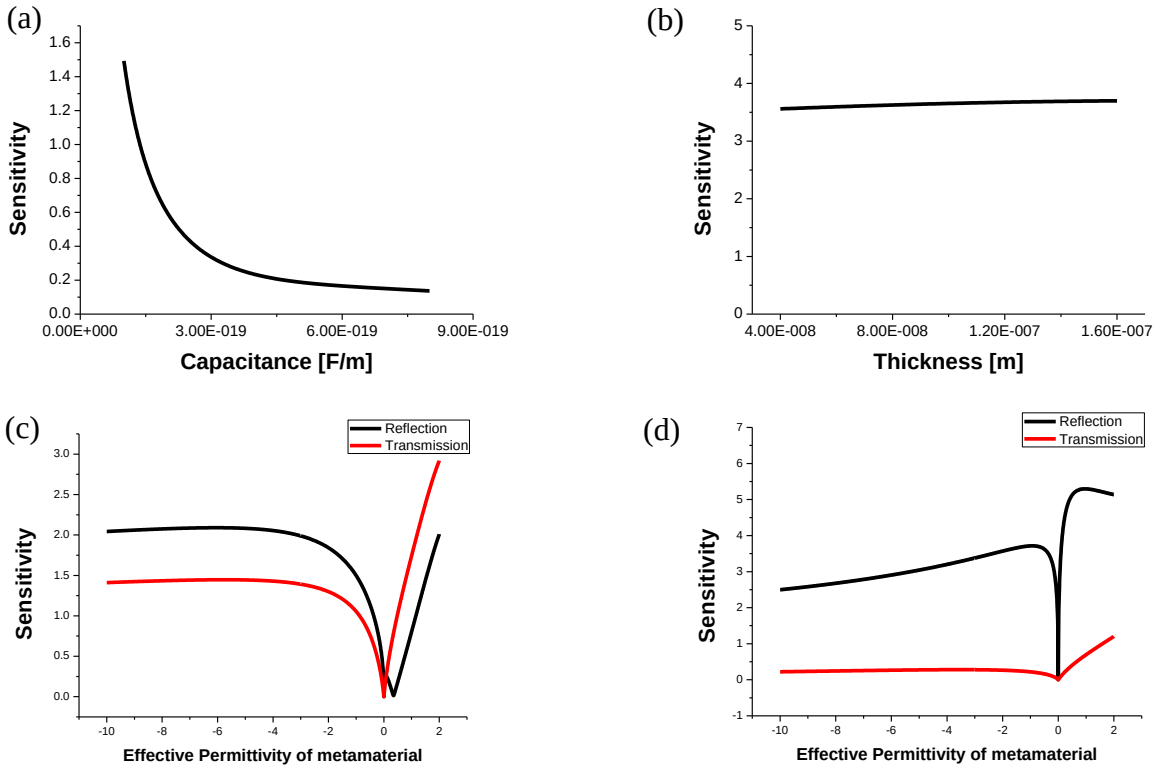

Figure 3.4 (a) Modulation sensitivity vs. capacitance in LC circuit, (b) the modulation sensitivity vs. thickness of effective medium, (c) the modulation sensitivity vs. effective permittivity at $\lambda = 1.5\mu m$, (d) the modulation sensitivity vs. effective permittivity at $\lambda = 1.4\mu m$.

The modulation depth also changes with other variables such as the overall thickness of the effective medium or the effective permittivity of the fishnet structure as shown in Fig.3.4 (b)-(d). The dependence of thickness is almost ignorable considering that there is not enough room for further increasing the thickness due to Fabry-Perot effect. It is interesting that the modulation depth can actually become larger with positive effective electric permittivity at certain cases, but it's not realistic to achieve using fishnet metamaterial since the dielectric constant of silver at near IR wavelength range is very negative and the filling ratio of metal is relatively large.

3.3. On-Fiber NIM Modulator

In real applications of NIM modulator, in order to reduce the complexity in alignment and coupling loss, attaching the modulator directly on the sidewall of an optical fiber or a waveguide might be the best way. The small footprint and self-alignment of the modulator will further reduce the cost of additional components and space. We explore the coupling of the guided optical signal in the optical fiber with the NIM on the side wall as shown in Fig. 3.5 (b). Our numerical studies indicate that fiber-guided modes strongly couple to the fishnet metamaterial near its resonance frequency, which gives a dip in the fiber transmitted output. Experimentally, the transmission through the fiber is measured on the etched D-shaped optical fiber by attaching the NIM on the sidewall. A transmission dip due to the coupling of the guided mode in the fiber and NIM is observed, which is in good agreement with the simulation result.

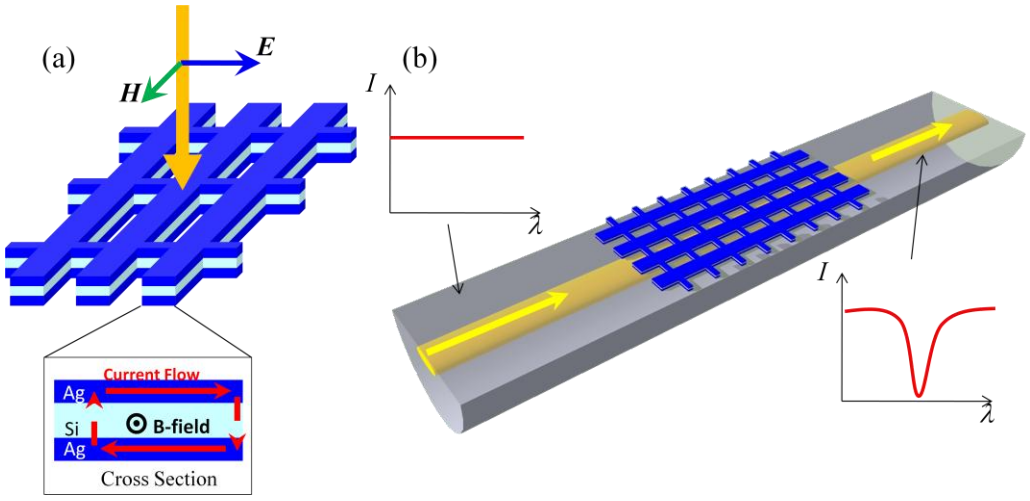

Figure 3.5 (a) Sketch of metal-dielectric metal fishnet structure with negative refractive index. The magnetic resonance is excited by the electric field along the thinner wire as shown in the figure. The current flow at the cross section of multilayer structure is indicated in the inset. (b) The concept of the on-fiber NIM configuration. The through fiber transmission is modulated due to the coupling of guided mode in the fiber and the mode in the NIM near the resonance wavelength.

The geometric parameters of the fabricated $Ag/SiO_2/Ag$ fishnet metamaterial are determined by performing the numerical 3D electromagnetic analysis using the commercial software package CST Microwave studio. These parameters are adjusted so as to obtain a desired resonant frequency (at fiber-communication wavelength) in the scattering parameters. The effective medium properties of fishnet metamaterial (ε_{eff}, μ_{eff}, n_{eff}) are retrieved from the scattering parameters using the method described in Ref. [50].

The on-fiber NIM is based on the resonant coupling among the modes in a fiber core and the modes in the metamaterial. This coupling occurs when the effective indices of waveguides, or equivalently, when the propagation constants in the two waveguides match [74]. To identify the propagation constant, wavelength, and bandwidth of the coupled mode we perform a dispersion study. Fig. 3.6 (a) depicts the schematic of the geometry used for computation. To simplify the calculation we model the fishnet metamaterial as a continuous effective index medium with ε_{eff} and μ_{eff} obtained from scattering parameters [48]. The fiber core (germanium doped silica) is modeled as a semi-infinite planar substrate with $\varepsilon = 2.1786$ and $\mu = 1$. In an actual sample, there is a thin cladding layer separating the fiber core and the fishnet metamaterial which has been neglected in the dispersion study for the sake of simplicity. We utilize the transfer-matrix method based on the Fresnel transmission and reflection coefficients to obtain the $\omega(k)$ dispersion plot.

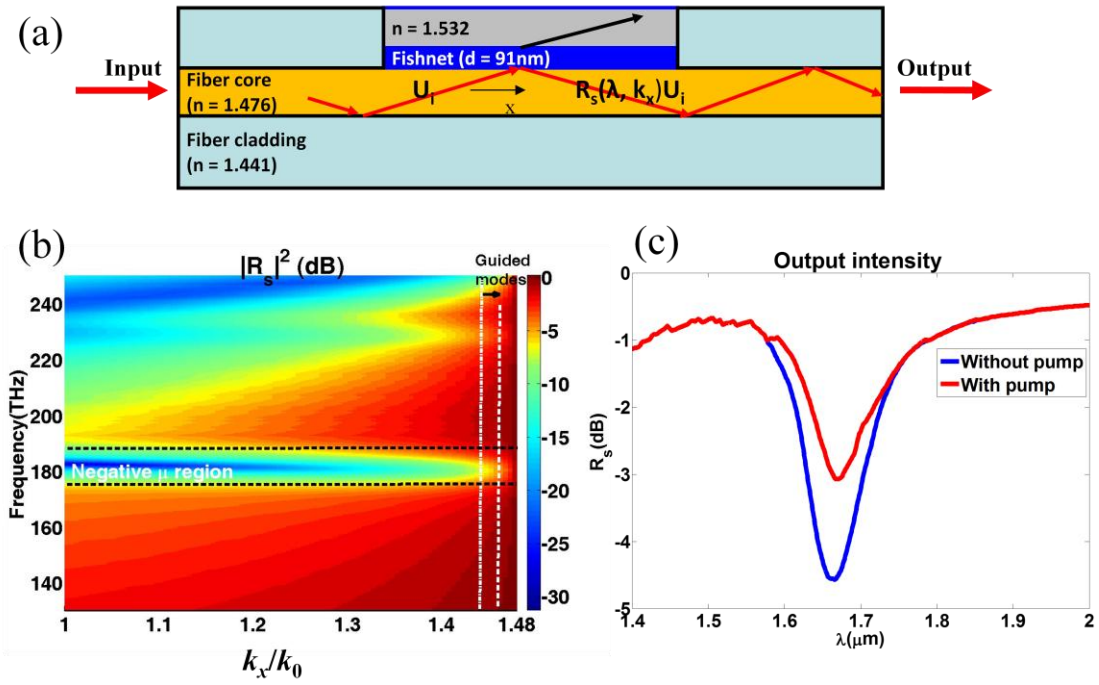

Figure 3.6 (a) Schematic illustration of fishnet modulator geometry used in the dispersion study. U_i denotes the incident field, and R_s represents the reflection coefficient for S-polarized light. (b) Dispersion plot for the reflected intensity (output). (c) Blue curve: output for a particular guided mode shown by white dashed line in (b) (k_x= 1.46k_0); modulated output from the fiber when the effective index of fishnet is changed with pumping.

Fig. 3.6 (b) shows the dispersion diagram for S-polarized light (TE mode). The color scale represents the reflected intensity (in dB). Since the overall interaction length of the fishnet modulator is short, we assume that the reflected intensity for the guided modes remain unchanged as they propagate through the fiber. Hence, the dispersion diagram directly corresponds to the fiber output. It should be noted that only the modes with k_x>1.441k_0 are guided by the fiber core due to total internal reflection from cladding. Fig. 3.6 (c) shows the reflected intensity in blue curve for such guided mode (k_x= 1.46k_0).

Earlier studies have suggested that the optical modulation of the effective properties of the fishnet metamaterial can be accomplished with Ag/Si/Ag heterostructure by photoexcitation of carriers in Si layer. It was experimentally demonstrated that the effective refractive index of

fishnet can be modulated by as much as 40% with relatively low pump fluence (~320 μJ/cm^2) [48]. Based on the results of this study, we investigate the modulation of output intensity through the fiber when the effective index of fishnet is changed due to free carrier excitation in the Si layer. The red curve in Fig. 3.6 (c) shows the modulation of the output intensity for the guided mode (k_x= 1.46k_0) with the external pumping. Modulation depth of 1.5dB is observed at the resonant wavelength. By incorporating a gain medium and increasing the length of NIM, it is expected that the modulation depth can be further increased.

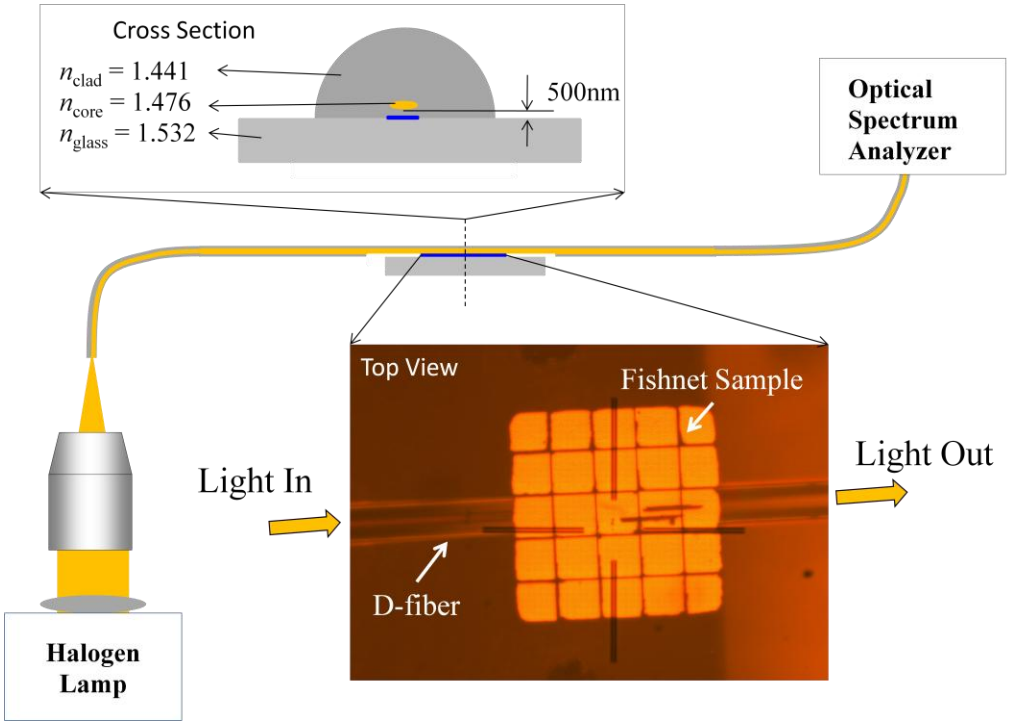

Figure 3.7 Sketch of the through-fiber configuration for transmission measurement. Side-polished and etched D-fiber is placed on top of the fishnet structure fabricated on the glass substrate. The light source from halogen lamp is coupled into the optical fiber by using the objective lens at one end, and the other end is connected to the spectrum analyzer to measure the through-fiber signal. Left-top inset is the sketch of the cross section and right-bottom inset is the optical image of the top view.

Commercially available D-shaped fiber (KVH industries) is employed to fabricate the fishnet metamaterial on the side of the fiber core. This D-fiber has a step index elliptical core

(4x2μm) and maintains polarization along the long axis of the ellipse, which fits our purpose. The index is 1.476 for the Ge-doped core and 1.441 for the F-doped cladding, supporting single mode propagation at 1.55μm. Initially, the cladding width on the flat side of the D-fiber is about 14μm, which turns out to be too thick to effectively couple the guided mode with fishnet mode. Therefore the flat side of the fiber was wet-etched using HF as described in Ref. [75]. The cladding width is gradually reduced until the evanescent field in the fiber core is exposed. As a first step, we performed transmission and reflection measurements for the fishnet metamaterial on the glass substrate with light incident from normal direction to identify resonance characteristics, which is presented in Fig. 3.8 (a). The polarization of the incident light is maintained along the thinner wire of the fishnet to excite a magnetic resonance. The sample is fabricated using the nanoimprint lithography (by HP Lab), which can provide large area fabrication (600x600 μm die is used in this specific case). To demonstrate the concept of evanescent coupling, spectrum of light propagating through the fiber is measured. Broadband light of halogen lamp is coupled into the fiber using the microscope objective lens, and the spectrum is obtained at the other side when the fiber using spectrum analyzer as illustrated in Fig. 3.7. An index matching fluid and appropriate weights are used to control the gap between fiber core and fishnet structure which is crucial for evanescent coupling. Estimated distance between fiber core and fishnet structure is between 500~700nm depending on the etching condition of the D-fiber. It is noted that the thinner wire of the fishnet structure is aligned perpendicular to the fiber propagation direction so that the electric field of guided light can excite the magnetic resonance in the fishnet due to the property of D-fiber. The through-fiber signal is normalized by performing the control experiment with the similar configuration but without the side-coupled fishnet structure.

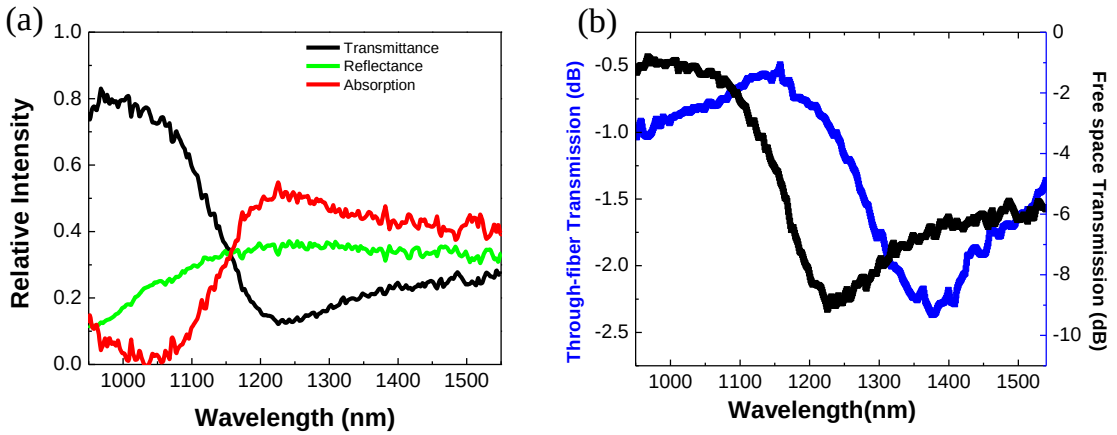

Figure 3.8 (a) Optical spectrum of the fishnet structure with the illumination from the normal direction. (b) Through-fiber transmittance (blue curve) compared with the free-space transmittance (black curve).

As shown in Fig. 3.6(a), a high reflectance from the fishnet allow the input signal pass through the whole fiber and give a high transmittance while a low reflectance from fishnet gives a low transmittance through the fiber. Thus, the experimental result shown by blue curve in Fig. 3.8 (b) is qualitatively in good agreement with the theoretical prediction (blue curve in Fig. 3.6(c)). We have observed 1.5dB of transmission dip which is weaker than theoretical prediction considering the size of the fishnet (more than 10 reflections while light is propagating through the fiber). This is due to the residual cladding of etched D-fiber and the diminished resonance strength with large angle of incidence and anisotropy of the fishnet metamaterial. The comparison of the spectrum with normal illumination is shown by the black curve in Fig. 3.8 (b). This measurement is done on the same area of the fishnet sample with normal illumination. We have observed a shift in resonance wavelength due to the index difference of the substrate for the different configuration and the inherent anisotropy when light is incident with an angle.

To achieve smaller footprints, we have performed the same experiment with the fishnet metamaterial fabricated directly on the etched D-fiber as depicted in Fig. 3.9 (a). Ag-SiO_2-Ag

(28-35-28nm) tri-layer is deposited by the e-beam evaporation on the flat side of the etched D-fiber. The thickness of each layer is obtained by the 3D electromagnetic analysis using the commercial software package (CST Microwave Studio). Finally, the fishnet structure is fabricated by using focused ion beam (FIB) milling. The size of the unit cell is 600nm and the width of the thicker and thinner wires are 300nm and 100nm respectively. Each pattern made on the core is 12 x 10μm in size, which is about 8 times larger than free space wavelength.

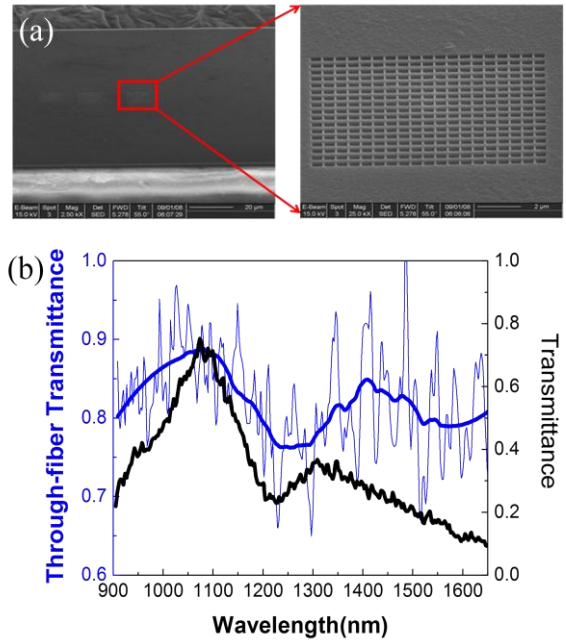

Figure 3.9 (a) FIB milling of the fishnet structure on Ag-SiO_2-Ag coated D-fiber. (b) Through-fiber transmission spectrum of the fishnet patterned D-fiber (thinner blue curve: original data; thicker blue curve: smoothened curve by averaging ten adjacent data) and the comparison with the normal-incidence illumination spectrum of the fishnet structure fabricated on the glass substrate.

Since the reference spectrum is measured first and then the signal spectrum is taken under the different bending condition of the fiber, after the FIB milling is done. The normalized transmission spectrum is rather rough due to the random bending loss of the fiber. Smoothening of curve reveals the coupling effect between guided modes and fishnet mode, which is shown in Fig. 3.9 (b). It is also observed that the red shift of resonance dip which is similar compared to

the result of the previous experiment. The depth of the transmission dip is shallower because of the smaller size (smaller number of reflection). It is noted that the resonance frequencies differ in two experiments mostly due to the thickness difference of multi-layers and the errors in dimension control during the sample fabrication.

3.4. Rotated Fishnet All Optical Modulator

Although the optical modulator based on the fishnet metamaterial successfully shows the modulation at the near-IR frequency range with photoexcitation of carriers in silicon layer [48], it has certain drawbacks. First, the fiber guided mode couples weakly to the resonance mode of the metamaterial compared to free-space coupling and secondly, as a result, the modulation depth is relatively moderate. Under fiber-guidance, light is incident on the metamaterial at steep angles, and therefore it reduces the resonance strength because some of the diffracted modes start to propagate through the metamaterial. In this section, a rotated fishnet design (See Fig. 3.10 (a)) is proposed for a potential optical modulator integrated on the fiber.

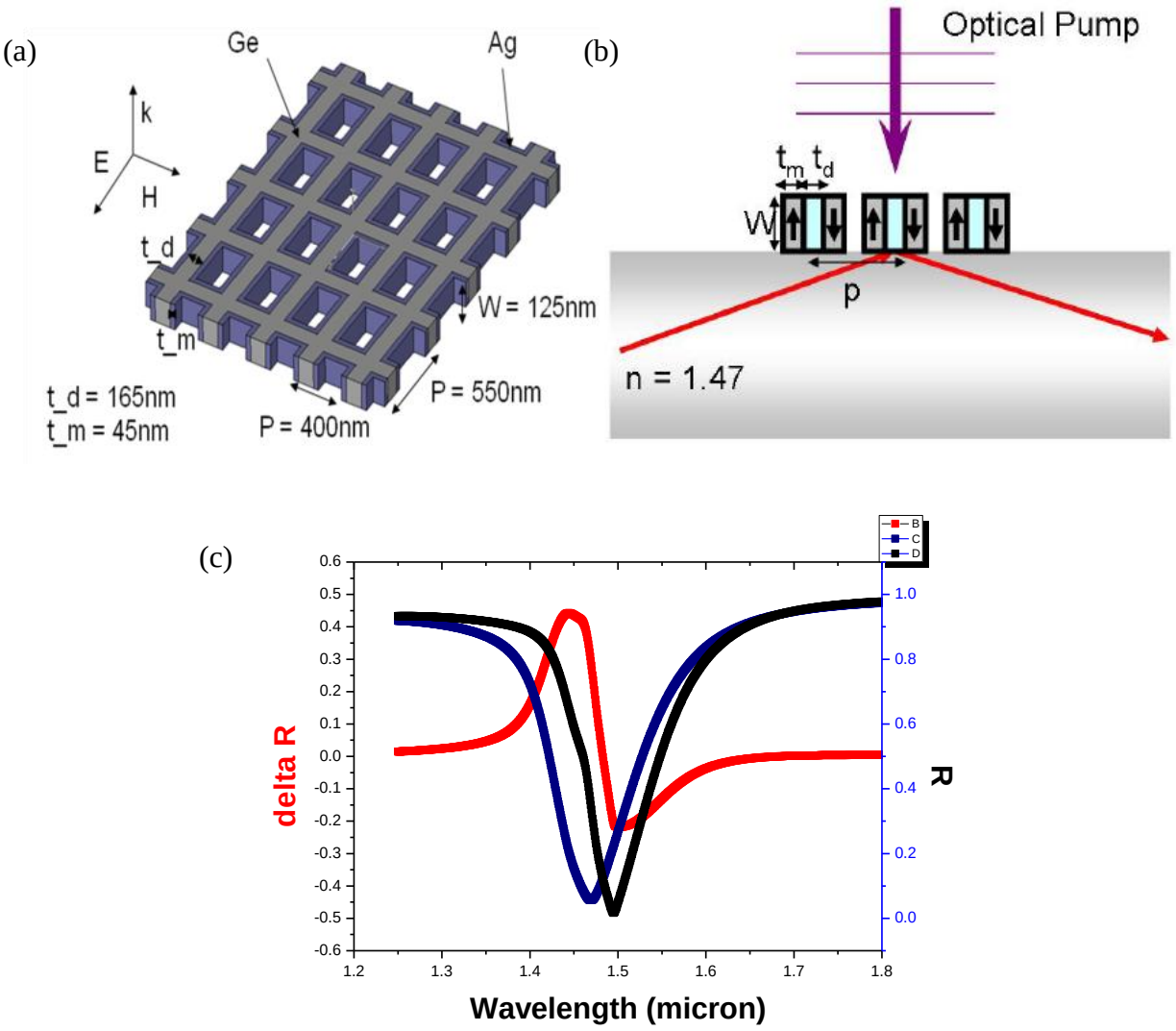

Figure 3.10 (a) Schematic of rotated fishnet design modified for an optimization. (b) Schematic illustration of a rotated fishnet modulator design in waveguide configuration. (c) 3D FDTD simulations of reflection coefficients and ΔR

To quantitatively understand the behavior of rotated fishnet when integrated onto a fiber, we have performed numerical simulations with oblique angles of incidence. The methods of simulating metamaterials at normal angle of incidence using finite difference time domain (FDTD) are well established [76], and the simulated results for rotated-fishnet modulator are shown in Fig. 3.10 (c). However, a simulation of broadband off-normal incidence poses a unique problem to the FDTD approach. In broadband simulations, the source injects a field with a

constant in-plane wavevector for all frequencies. This implies that the actual injection angle varies as a function of frequency. Multiple simulations are required to gather simulation data at various frequencies for a fixed angle of incidence [77]. We have investigated the rotated metal-dielectric-metal resonator design at various oblique angles of incidence. A parametric sweep for various angles of incidence is done within the wavelength range of interest. Bloch boundary conditions are used along the periodic direction of the metamaterial. For simplicity, we have considered a two-dimensional case where the electric rods such as in fishnet design are eliminated. The data obtained from these simulations is irregularly spaced and has been interpolated to a rectangular grid of angle of incidence and wavelength for ease of plotting.

Fig. 3.11 (a) shows the dispersion plot of the transmission response of rotated resonators against frequency and angle of incidence. It is observed that the resonance becomes narrower with increased angle of incidence. This is attributed to reduced losses as increasing oblique incidences start to support anti-phase currents in adjacent units of rotated resonators. To illustrate the operation of a rotated fishnet as an integrated fiber modulator, we have plotted the field intensity and phase at probe wavelength of 1550nm (See Fig. 3.11 (b)). Light is incident from the fiber side at an angle of 70 º. Vector plot of the electric field depicting the phase is shown in Fig. 3.11 (c). It is observed that the phase (along the solid black lines) in the two metal regions differs by ~164 º. This suggests that the conduction currents in the two metal strips are almost anti-parallel.

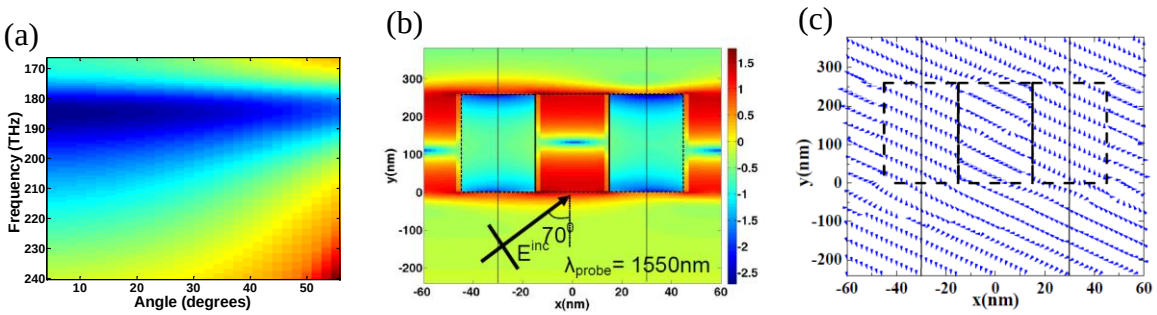

Figure 3.11 (a) Dispersion plot for rotated fishnet design computed with FDTD simulations. (b) Field distribution (log scale) at probe wavelength (λ = 1550nm). Light is incident from the bottom (fiber core, n = 1.47) at an angle of 70 º. The metal-dielectric metal sandwich structure is marked by black dashed lines for clarity. (c) Vector plot of the electric field, showing counter-propagating current direction in the two metal layers. Phase difference in metal regions along the two vertical black lines is 164 º.

The sample was fabricated using a sequence of e-beam evaporation, FIB milling, and electrochemical etching. First, 125nm-thick α-Ge and 15nm-thick SiO_2 are deposited using e-beam evaporation on a glass substrate. Rotated fishnet structure is fabricated by FIB milling, as shown in Fig. 3.12 (a). A sputtering of silver is followed to cover the sidewalls of α-Ge wires, and then an electrochemical etching is done to remove the top silver layer. The SEM image of the final structure is shown in Fig. 3.12 (b). A thin layer of SiO_2 was added to improve the quality of FIB milling and to prevent the over-etching of Ag sidewalls, and it does not cause any significant change in the resonance wavelength according to the full field simulation.

An ellipsometry measurement is done for an e-beam evaporated α-Ge film to retrieve the index parameters. It is quite similar to that of crystalline Ge but it shows near-zero imaginary part of index (k < 0.01) around 1.55 μm even with an existence of indirect band gap at 1.7 μm. It is found that the high vacuum level below $5\times10^{-7} torr$ is critical to maintain low-loss optical property at operating wavelength.

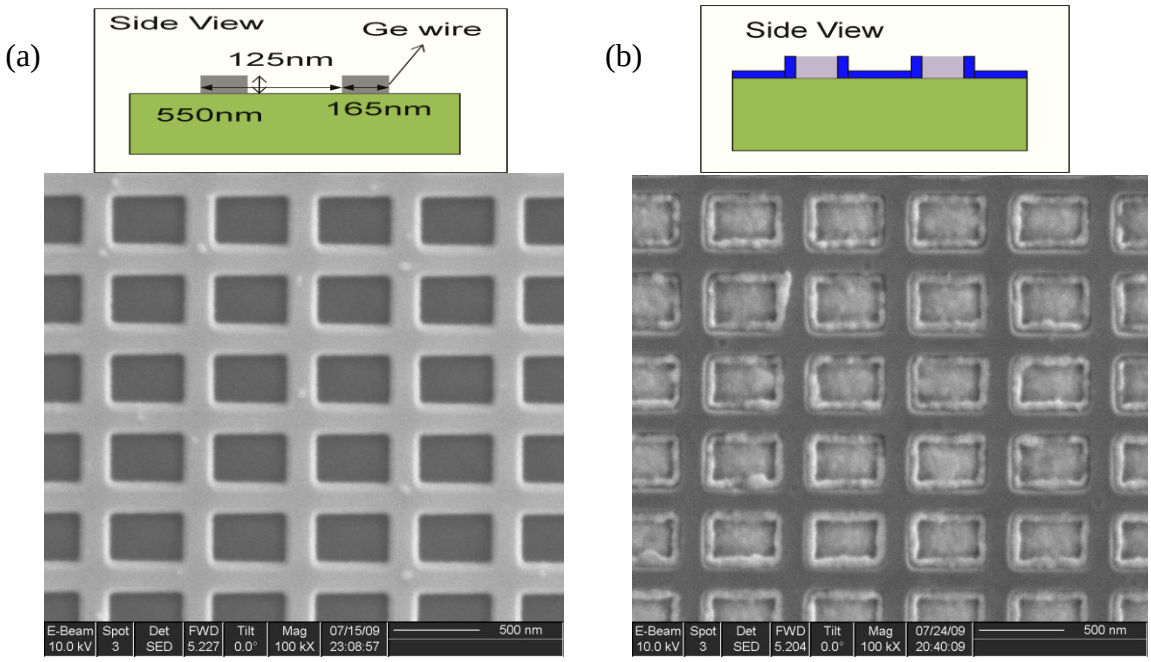

Figure 3.12 Fabrication of the rotated fishnet metamaterial. (a) Schematic drawing and SEM image of patterned Ge wires by FIB milling. (b) Schematic drawing and SEM image of rotated fishnet modulator after the electrochemical etching of top Ag layer.

Normal incidence optical spectra are measured using a reflection microscope with an attached spectrum analyzer, as shown in Fig. 3.13 (a). The reflection and transmission indicate a resonance around 1300nm for the rotated-fishnet sample. The modulation depth of the device is done in a pump-probe system [48]. The dependence of pump fluence is measured at the wavelength of 1300nm, and is shown in Fig. 3.13 (b). The depth of modulation is linearly proportional to the pump fluence, which is the case for the conventional fishnet too. The time response is around 2 ps (see Fig. 3.14), which is slightly slower than the time response of pure α-Ge film.

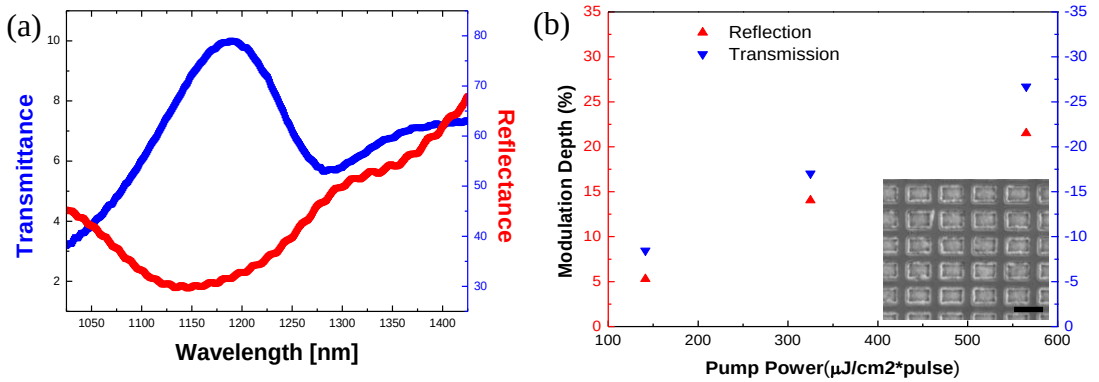

Figure 3.13 (a) Transmission and reflection spectrum of rotated fishnet modulator. (b) Pump fluence dependence of the modulation depth at the wavelength of 1300nm. Inset shows a SEM image of rotated-fishnet modulator.

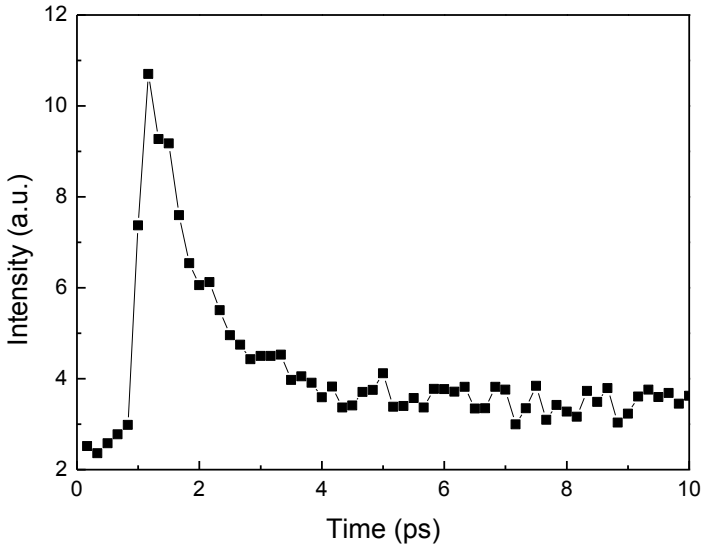

Figure 3.14 Temporal response of modulation measured by pump-probe technique.

3.5. Summary and Conclusion

To summarize, an all-optical modulator based on a fishnet metamaterial is designed, fabricated and demonstrated. A theoretical modeling followed by the FDTD simulation indicates the

effective refractive index change of active medium is amplified more than 10-fold due to the localized field originated from the magnetic resonance. Near-zero refractive index nearby the resonance wavelength of the fishnet structure results in the broadening of PSF up to 6.9μm according to the NSOM experiment, which is also confirmed by the simulation using homogenized effective mediums. This gives a guideline to the minimum size of the optical modulator that can be built, which is only about 5 times of the operation wavelength. Toward building a compact and small footprint on-fiber optical modulator, coupling effect between the fishnet mode and the fiber-guided mode is investigated. 1.5dB transmission dip due to the evanescent coupling of such modes is observed. A rotated fishnet structure is designed to maximize the modulation depth in an on-fiber modulator design. Due to the reduced ohmic loss and effective pumping of the active medium, a free-space modulation depth of 40% with an ultrafast temporal resolution of 2ps is demonstrated.

Chapter 4 Plasmonic Nano-Bubble Cavity

4.1. Introduction

Plasmonics opens a new era in variety of applications in the fields of optical storage, optical imaging and photonic signal processing [29,78,79,80,81]. One of the essential constituents in such applications is a subwavelength light source. Radiative characteristics of active medium such as semiconductor bulk medium or fluorescent molecules can be improved by being placed in a micro-cavity or photonic crystal due to an increased local optical density of states (LDOS) as noted by Purcell [33]. However, such incorporation comes with sacrifice in size [82]. In this respect, the role of plasmonics falls into a sweet spot, providing means of manipulating light-matter interaction while maintaining the overall dimension below the wavelength scale [34,35,36,37].

The earliest experiment identifying the effect of surface plasmon on fluorescence is performed by Drexhage *et al.*, where radiation intensity depends on the distance from a nearby thin metal film [83]. Such effect is well explained within the boundary of classical electrodynamics based on the oscillating electric dipole model [83,84,85]. With sophisticated designs of composite metal-dielectric nanostructures, the rate of radiation can indeed be significantly enhanced, which leads to the plasmonic laser [34,35,36,37] as was predicted theoretically [86].

Among them, metal-insulator-semiconductor (MIS) structure is particularly interesting because of their potential incorporation with semiconductor electronics [87,88]. In MIS

geometry, the energy is strongly confined within a low index insulator due to mode hybridization and strong index contrast between insulator and semiconductor layers [89,90], which results in a relatively low ohmic loss in the metal layer. Obviously, such confinement effect strongly depends on the gap width profile of the insulating layer [35,37,90]. Although lifetime measurement shows that the enhancement of the spontaneous emission is accounted for the plasmonic cavity, localized nature of such enhancement is not directly observed so far.

In this chapter, I demonstrate the generation of nanoscale light from a nano-bubble trapped in between metal and semiconductor with a subwavelength resolution. First, theoretical modeling based on a dipole radiation is proposed to explain the results of the interaction between a local light source and plasmonic modes. And then Cathodoluminescence (CL) imaging is performed to study local optical density of states (LDOS) experimentally, as shown in Fig. 4.1.

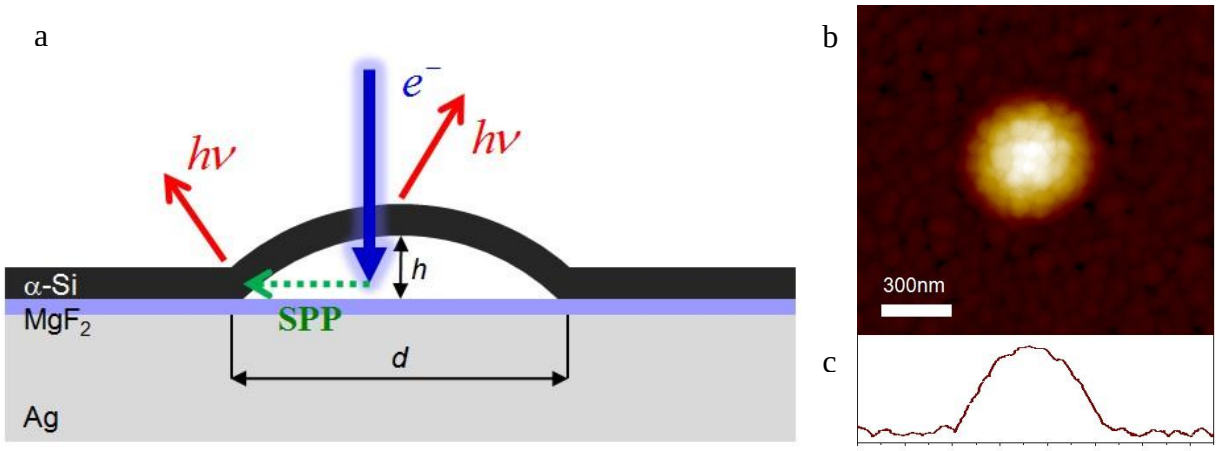

Figure 4.1 Electron beam induced photon emission. (a) Schematic view of α-Si/Air/MgF_2/Ag nano-bubbles. Thickness of α-Si, MgF_2, Ag is 25nm, 5nm and 250nm respectively. An air bubble is trapped in between α-Si and MgF_2. Ag is thick enough to block any light emission from Si wafer substrate. 50nA electron beam accelerated by 30kV is focused and scanning over the sample, while induced photons are collected into the PMT by a parabolic mirror covering 1.4π solid angle. Both scattered SPP and direct radiation contribute to the photon count. (b),(c) An AFM image of a nano-bubble and its line profile. The ratio of height to diameter varies from 1/4 to 1/9 depending on the dose of ion beam exposure.

4.2. Dipole Modeling of a Point Light Source

In the regime of classical electrodynamics, the light emission from a fluorescence molecule is modeled by an oscillating electric dipole with radiation. Although one also needs to consider quantum mechanical processes to fully explain the phenomenon, it's been demonstrated that such simple model can successfully explain the change in radiation intensity when the molecule is placed nearby the metallic layer [83,84,85]. The energy transfer from a molecule to local optical modes can be calculated by considering the work done by the dipole. Total power dissipation from the oscillating electric dipole can be evaluated by an inner product of electric dipole moment and total electric field applied on the dipole, where the electric field is originated from the reflected dipole fields [85].

$$\mathrm{P} = \frac{\omega}{2}\,\mathrm{Im}(\boldsymbol{\mu}^{*}\cdot\mathbf{E}) = \frac{\omega|\boldsymbol{\mu}|^{2}}{2\varepsilon}\,\mathrm{Re}\int_{0}^{\infty} dk_{\parallel}\,\frac{k_{\parallel}^{3}}{k_{\perp}}[1+r_{total}^{p}]\,, \tag{4.1}$$

where ω, $\boldsymbol{\mu}$, ε, $k_{\parallel}$, $k_{\perp}$ and r_{total}^{p} are angular frequency, electric dipole moment, dielectric constant of α-Si, in-plane wavevector, out-of-plane wavevector, and total reflection coefficient respectively.

Total reflection coefficient is calculated by a series summation of Fresnel coefficients of multiple reflections at the interfaces above and below the dipole, as shown in Fig. 4.2.

$$[1+r_{total}^{p}] = 1 + r_{213}^{P}e^{2ik_{\perp}d} + r_{213}^{P}r_{21}^{P}e^{2ik_{\perp}t_{Si}} + (r_{213}^{P})^{2}r_{21}^{P}e^{2ik_{\perp}(t_{Si}+d)} + \ldots$$
$$+ r_{21}^{P}e^{2ik_{\perp}(t_{Si}-d)} + r_{21}^{P}r_{213}^{P}e^{2ik_{\perp}t_{Si}} + (r_{21}^{P})^{2}r_{213}^{P}e^{2ik_{\perp}(2t_{Si}-d)} + \ldots = \frac{1 + r_{213}^{P}e^{2ik_{\perp}d} + r_{21}^{P}e^{2ik_{\perp}(t_{Si}-d)} + r_{213}^{P}r_{21}^{P}e^{2ik_{\perp}t_{Si}}}{1 - r_{213}^{P}r_{21}^{P}e^{2ik_{\perp}t_{Si}}}$$

, where $k_{\perp} = \sqrt{\varepsilon_{Si}\omega^{2}/c^{2} - k_{\parallel}^{2}}$, $k'_{\perp} = \sqrt{\omega^{2}/c^{2} - k_{\parallel}^{2}}$, $t_{12}^{p} = 1 + r_{12}^{p}$, $t_{13}^{p} = 1 + r_{13}^{p}$ and

$$r_{213}^{P} = r_{21}^{P} + t_{12}^{p}t_{21}^{p}r_{13}^{p}e^{2ik'_{\perp}g} + t_{12}^{p}t_{21}^{p}r_{13}^{p}e^{2ik'_{\perp}g}\cdot r_{12}^{p}r_{13}^{p}e^{2ik'_{\perp}g} + \ldots = \frac{-r_{12}^{p} + r_{13}^{p}e^{2ik'_{\perp}g}}{1 - r_{12}^{p}r_{13}^{p}e^{2ik'_{\perp}g}}\,.$$

Total power dissipation is proportional to the decay rate of dipole moment, and therefore proportional to the LDOS, representing so-called “Purcell factor” at the position where dipole is placed.

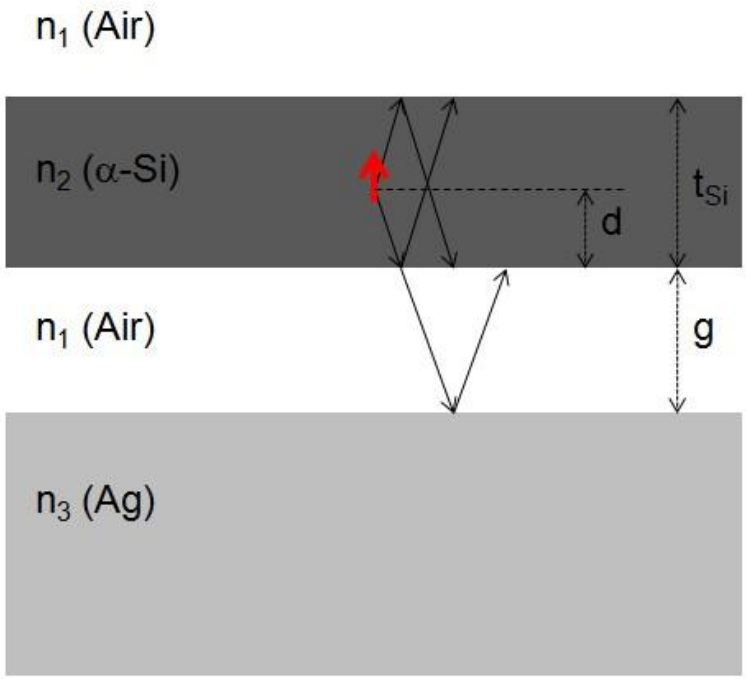

Figure 4.2 Schematic view of α-Si/Air/Ag planar geometry. The position of electric dipole is shown by a red arrow. t_{Si}, d and g indicate the thickness of α-Si, position of the dipole and the width of the air gap, respectively. First few components of multiple reflections at each interface are shown in black arrows.

4.3. Experimental Setup: Cathodoluminescence Microscope (CL)

Conventional optical microscope provides neither a subwavelength light source nor a capability of measuring local optical fields due to the diffraction limit. Near-field scanning optical microscope can achieve a subwavelength resolution but it is limited by a perturbation due to the metal-coated probe sitting on the structure [91]. Recently, an optical imaging based on electron microscopy such as cathodoluminescence (CL) microscopy and electron energy loss

spectroscopy (EELS) brought a new attention in the field of plasmonics [91,92,93,94,95,96,97,98]. Due to the strongly localized field near the electron, the induced photon is also highly localized, and thus provides a resolution beyond the diffraction limit with a capability of exciting high momentum modes such as the surface plasmon mode. Most of the studies are so far focused on identifying resonant plasmonic modes in metallic nano-particles or cavities [91,92,93,94,95,96,97,98]. The generation of photon is modeled as an oscillating vertical electric dipole in the case of simple air/metal interface [91], but it is not clear for the complicated structures. In this experiment, electron beam induced luminescence from an α-Si layer, which serves as a strongly localized light source, makes it possible to map two dimensional LDOS of a nano-bubble cavity via measuring an enhanced luminescence with subwavelength resolution.

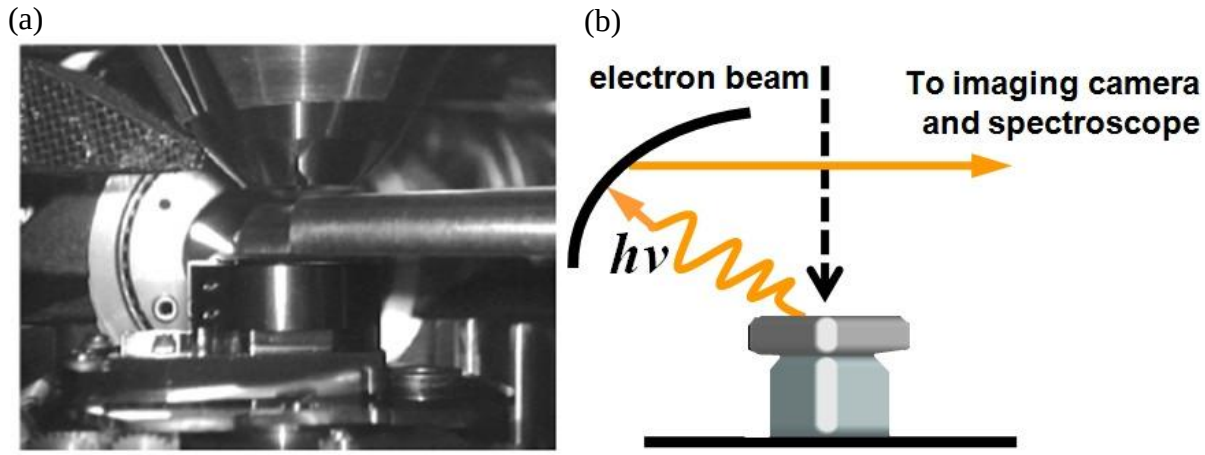

Figure 4.3 Experimental setup. (a) Inside view of a SEM chamber with a parabolic mirror mounted. (b) Schematic view of the setup. Electron beam from a SEM gun is bombarding the sample, while induced photon is collected by the parabolic mirror.

A high energy electron beam (30keV, 50nA) is tightly focused on the structure to induce photon generation. While the beam is scanning over the sample area pixel by pixel, generated photons are collected by the photomultiplier tube (PMT) at each pixel, which give rises to an optical image. Fig. 4.1a depicts two major processes of photon generation and collection. First,

the induced photons with low horizontal momentum are radiated into the free space possibly after multiple reflections in the structure. Second, some part of the energy is coupled into the surface plasmon polariton (SPP), which propagates toward the bubble boundary and then scatters into the free space. The energy of emitted photons has a broad spectrum over the visible range, and therefore, a set of bandpass filters centered at 650nm, 550nm and 450nm with bandwidths of 40nm, 80nm and 40nm respectively, is installed in the optical path to provide wavelength dependent information.

4.4. Sample Fabrication

The nano-bubble cavity, as shown in Fig. 4.1, is generated by a focused ion beam (FIB) exposure on α-Si/MgF_2/Ag tri-layer which is deposited on a silicon wafer. The gradient of the air gap width in the bubble provides a unique opportunity to study optical modes and corresponding LDOS of the MIS structure. First, 5nm thick MgF_2 and 25nm thick α-Si layers are deposited using an e-beam evaporation and a DC sputter coating, respectively, on top of an optically thick silver film. Then, nano-bubbles are generated by exposing the sample with FIB (30keV Ga+ ion) in a raster mode. The role of MgF_2 is crucial since it demotes the adhesion of the top α-Si layer and also adsorbs molecules that can be released later by FIB exposure. Bubble generation in polymer is reported [99] but it is for the first time in the case of Si to the best of our knowledge. Although it is random in nature, the average size of nano-bubbles can be controlled by the dose and the scan rate of ion beam, as is shown in Fig. 4.4. In general, a slower scan rate results in larger bubbles. α-Si film is likely to be damaged if the beam current is too high, so it should be lowered accordingly as the scan rate decreases.

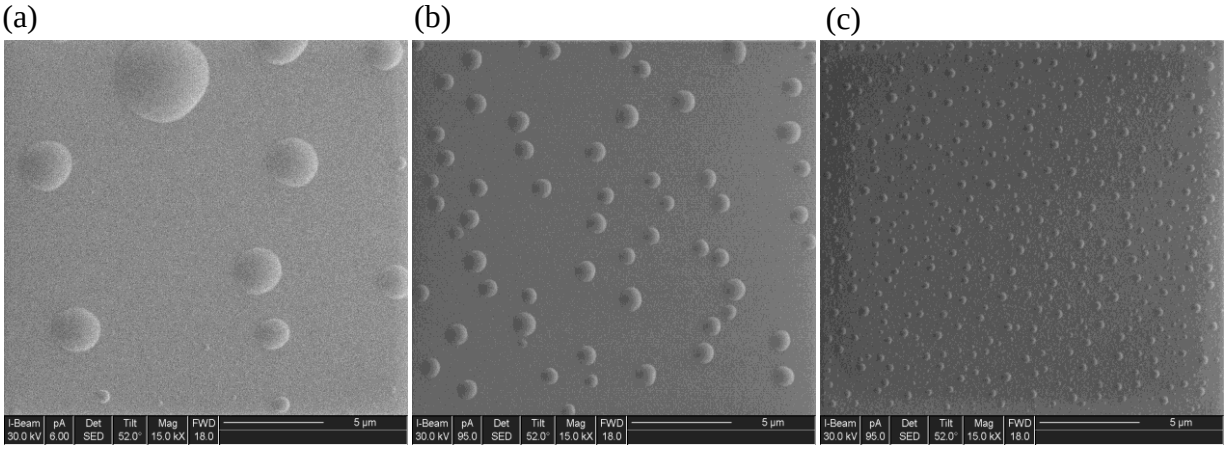

Figure 4.4 SEM image of generated bubbles with the different ion beam dose and scan rate. (a)-(c) the average size of bubbles are 2.0μm, 680nm and 190nm, respectively. The scan rate and beam currents are 40ms/line with 6pA, 12ms/line with 28pA and 1ms/line with 95pA, respectively.

4.5. Results and Discussion

As is shown in Fig. 4.5, multiple fringes are observed with their peak position dependent on the size of bubble and wavelength. It is observed that the rim of bubbles always shine up, while the additional fringes only appear on the larger bubbles. The position with peak luminescence is strongly dependent on the gap size just as in the case of the Newton's Ring where an interference of reflected light from different interfaces dominates the phenomenon. The width of the light rim is measured to be 96±19nm for the blue wavelength, which clearly demonstrates subwavelength capability of the CL system. Although there is a surprising similarity, the physical origin is not the same. It is noted that, in the case of bubbles of irregular shapes, light ring is closely following the geometrical boundary, indicating that this is not due to standing SPP mode along lateral direction, which is the case in other studies [96,97,98].

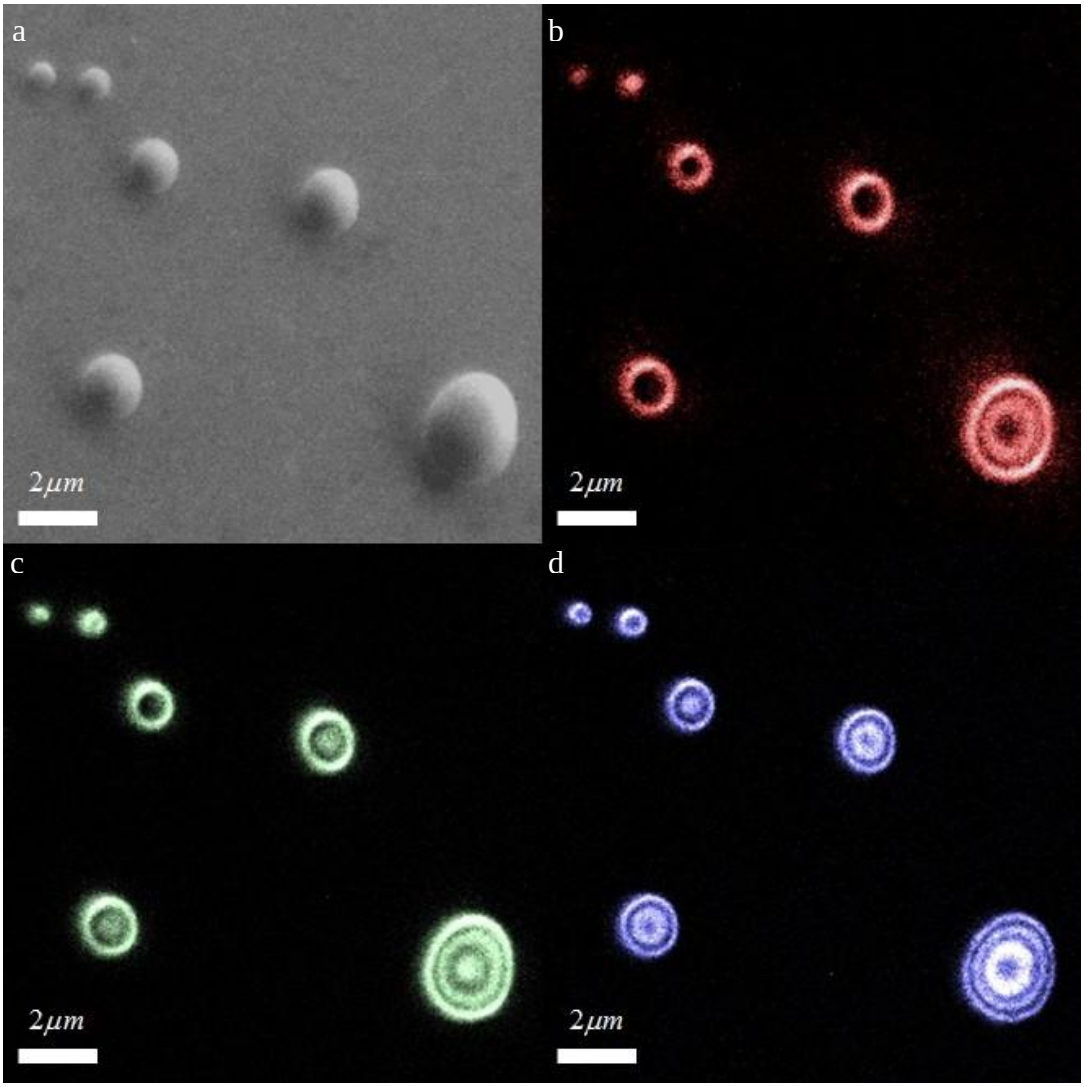

Figure 4.5 Cathodoluminescence optical images of nano-bubbles. (a) A SEM image of nano-bubbles simultaneously taken with the CL images. (b)-(d) Subwavelength optical images of nano-bubbles captured by CL microscope. The color of each image indicates the center wavelength of bandpass filters that are used during the collection of photons, which are 650nm, 550nm and 450nm respectively. The brightness in each image is normalized and does not depict the actual light intensity. The diameter of the largest bubble at the right bottom corner is 2230±39nm along the horizontal direction.

The enhancement in CL intensity is a result of interactions between a local photon source in the α-Si layer and optical modes, which are characterized by LDOS. First, dispersion

diagrams of one dimensional structure with air gap of 50nm and 500nm are plotted in Fig. 4.6 (a) and 4.6 (b) to investigate optical modes. In the former case, there is only SPP mode at α-Si/Air/Ag available in the visible range. In the latter, additional cavity modes appear due to the trapped TM waves within the air gap, denoted by TM_2, TM_3 and TM_4. Second, the local photon source in the α-Si layer is modeled by an oscillating vertical electric dipole to calculate LDOS. Power transfer spectrum as a function of the wavenumber, which is given in Eq. 4.1, is plotted together in Fig. 4.6 (c) and 4.6 (d).

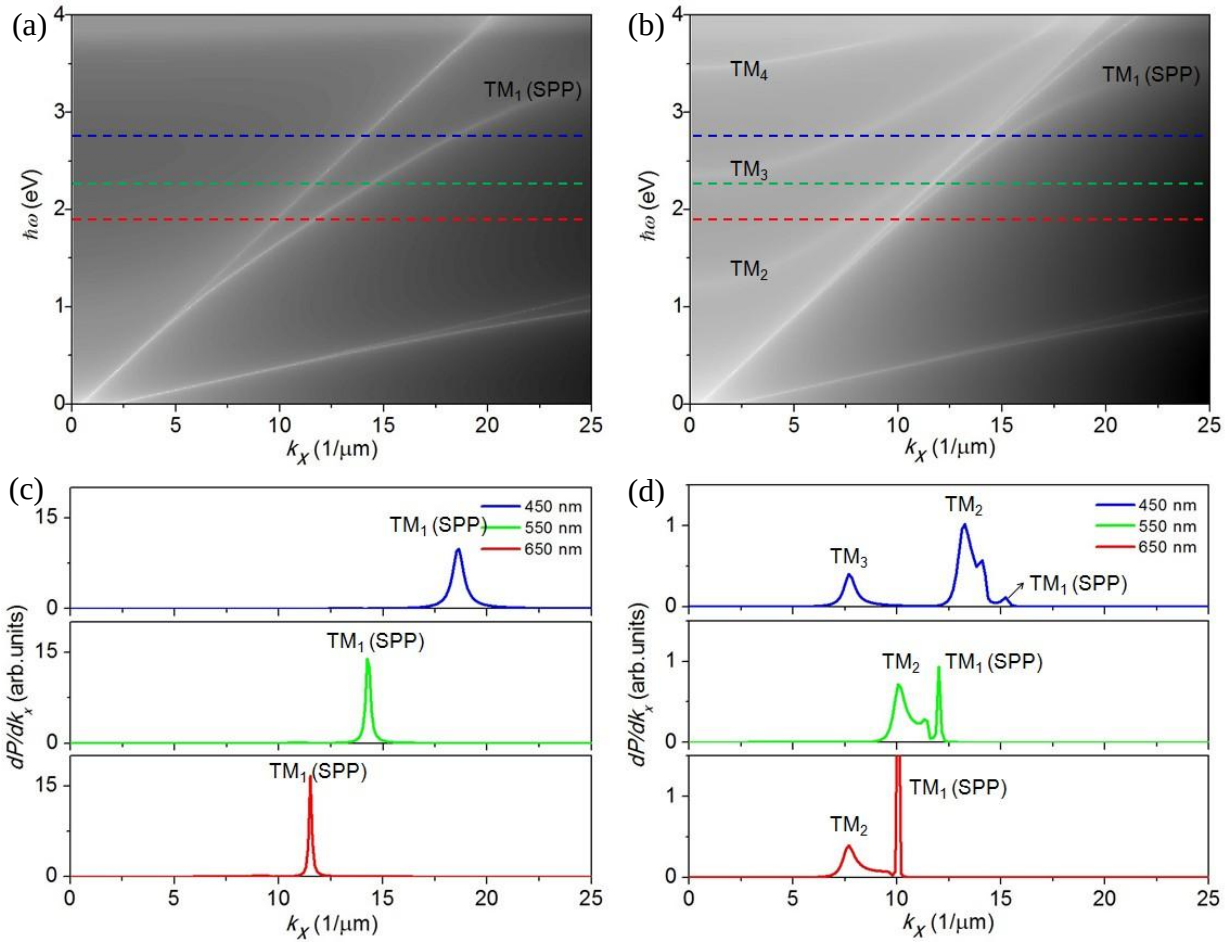

Figure 4.6 Dispersion and power transfer spectrum as a function of in-plane wavevector. Dispersion diagrams of Ag/Air/α-Si structure with air gap of (a) 50nm and (b) 500nm respectively. Dotted lines in red, green and blue indicate the wavelengths of 650nm, 550nm and 450nm respectively. (c)-(d) Power transfer spectrum as a function of in-plane wavevector k_x. Energy is mostly coupled into surface plasmon with an air gap of 50nm, while coupling into leaky TM_2 or TM_3 modes becomes dominant with an air gap of 500nm. It is noted that the peak positions in each energy transfer spectrum correspond to the crossover of dispersion curve and dotted lines.

In the case in-plane wavenumber k_x of SPPs varies slowly as it propagates ($\left|d(k_x)^{-1}/dx\right| << 1$), mode conversion can be fully adiabatic [100]. Wave propagating along x can be written in the form of eikonal approximation, $\Psi(x,z,t) = A(x)f(x,z)e^{i\int_0^x k_x(x')dx' - i\omega t}$ [101]. SPPs generated near the center of nano-bubble initially propagate adiabatically, but are

eventually scattered near the boundary where the air gap changes rapidly and so is the wavenumber k_x. $\left|d(k_x)^{-1}/dx\right|$ can be calculated from the dispersion plot given in Fig. 4.6. At 30nm distance from the boundary for the largest bubble, $\left|d(k_x)^{-1}/dx\right|$ is calculated to be 0.33, 0.34 and 0.28 for wavelengths of 450nm, 550nm and 650nm respectively. This indicates the scattering of SPPs mostly happens near the boundary [100]. Therefore the total CL intensity is now sum of low k_x component and high k_x SPP component that is scattered at the boundary with scattering coefficient S;

$$I_{CL} = \int_0^{0.7k_0} dk_{\|} \frac{dP}{dk_{\|}} + \int_{k_0}^{\infty} dk_{\|} \frac{dP}{dk_{\|}} \cdot S \cdot e^{-\int_{|x|}^{d/2} \mathrm{Im}[k_{SPP}(x)]} . \quad (4.2)$$

The decay rate P indicates the power transferred from the local photon source into the structure and free space. In Fig. 4.6 (c) and 4.6 (d), power transfer spectrum $\frac{dP}{dk_{\|}}$ is plotted as a function of $k_{\|}$. The energy transfer peaks when $k_{\|}$ is the same as that of TM and SPP modes.

Although different modes are clearly separated in the momentum space as shown in the plot of power transfer spectrum, it is not necessarily the case in the position space. The power transfer spectrum as a function of the position and the in-plane momentum is plotted in Fig. 4.7(a)-(c), by replacing the fixed air gap width as a function of the position in the bubble. This is basically a one-dimensional approximation which ignores the effect of slope in the α-Si layer. In the case of the largest bubble in Fig. 4.5, the size and height are measured to be 2230 ± 39nm and $383\text{nm} \pm 7$nm by AFM. However, the actual height is assumed to be 575nm to explain the observed peak position. This discrepancy is due to the expansion of nano-bubble by heating effect from the high energy electron during the experiment. Fortunately, there is a dominantly contributing mode at different positions which give rises to a peak CL intensity, as shown in Fig.

4.7 (d)-(f). Here the SPPs are responsible for the light generation at the rim, while the conventional TM modes account for the inner rings.

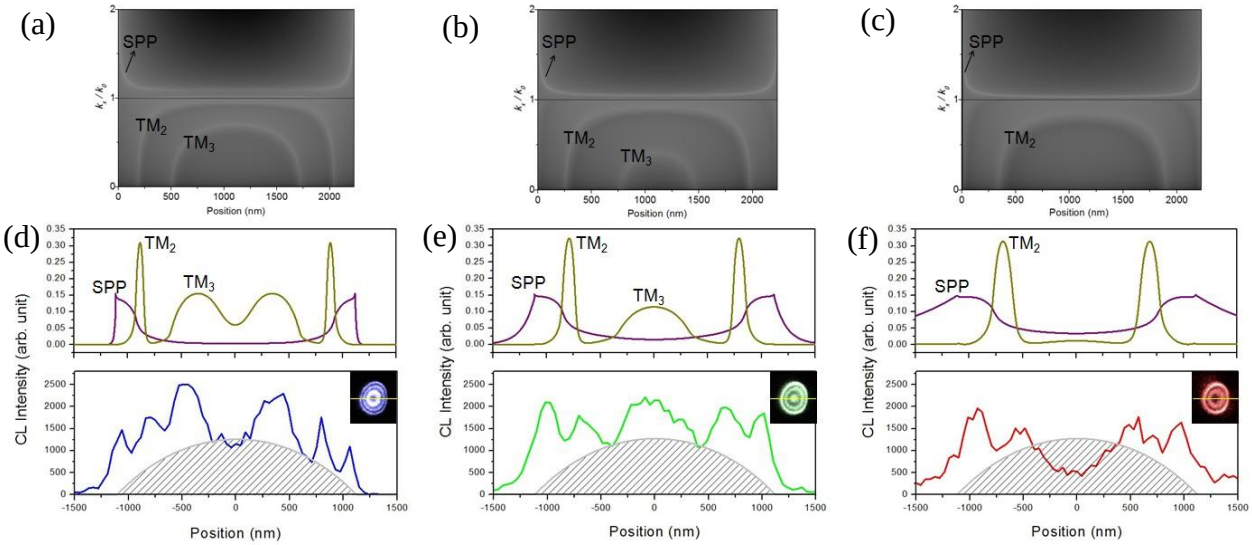

Figure 4.7 2D power transfer spectrum as a function of position and k_x. (a)-(c), Power transfer spectrum as a function of lateral position of dipole in the bubble and in-plane wavevector $k_{||}$ at the wavelengths of 450nm, 550nm and 650nm respectively. A vertical electric dipole is assumed to be in the thin α-Si layer above 5nm from α-Si/Air interface. (d)-(f), Line profiles of the calculated (top) and measured (bottom) CL intensity across the nano-bubble as is shown in the insets.

Although multiple fringes are explained purely by the gap dependent changes of LDOS, it is desirable to perform a control experiment to eliminate the possibility of exciting horizontally confined SPP modes, as is often the case reported in other literatures [93,95,96]. In Fig. 4.8 (a), a SEM image of nano-bubble with a slit that cuts partially into the bubble is shown. A panchromatic and a monochromatic CL imaging of the corresponding structures (in Fig. 4.8 (b)-(c)) show that the CL intensity in the rest of the bubble is not affected by the slit, which indicates the observed optical modes are neither Bessel modes nor whispering gallery modes. It is also noted that the circular slit surrounding the nano-bubbles (shown in Fig. 4.8 (d)) does not affect

the CL signal, which means the excitation of SPPs outside the bubble does not affect the observed optical modes.

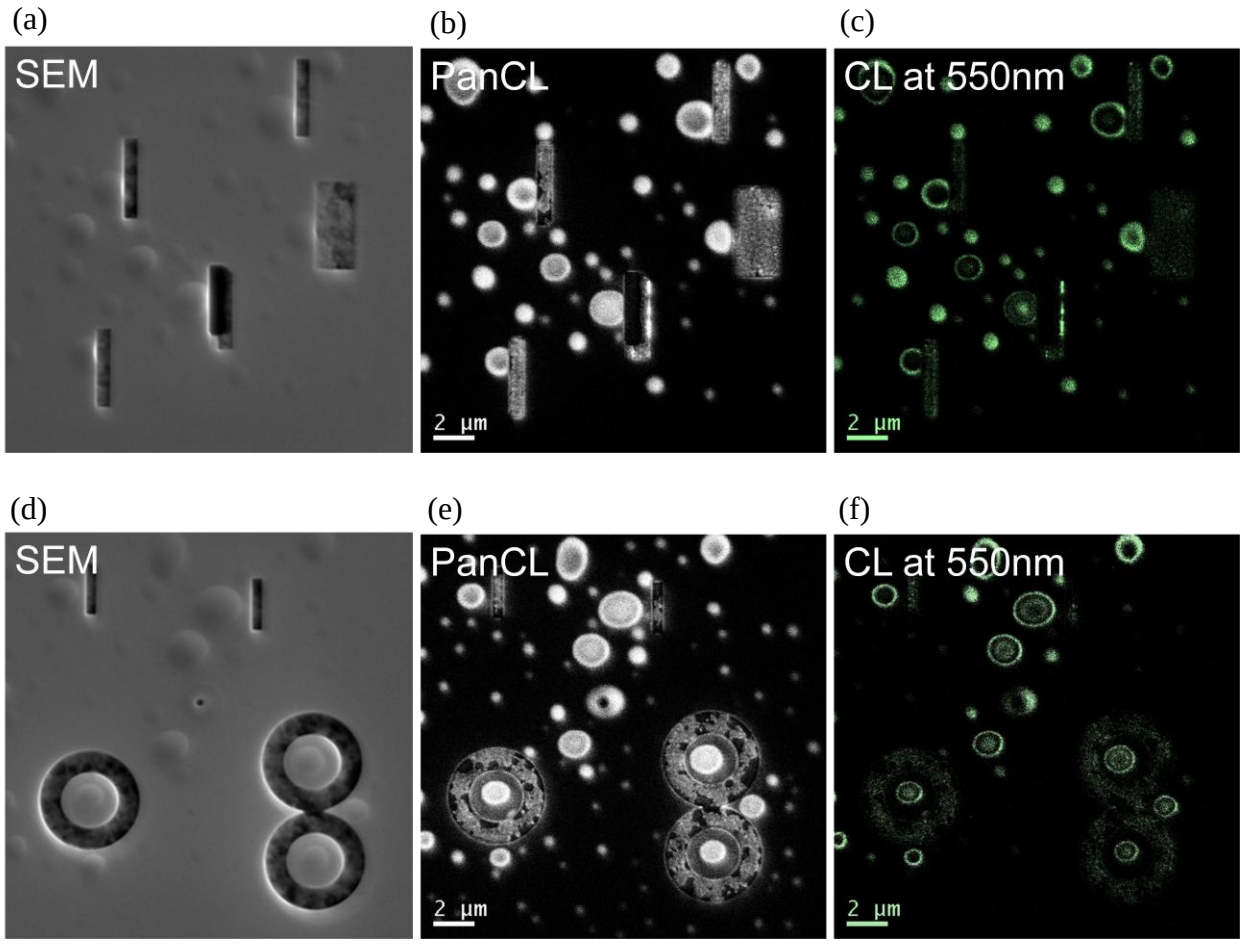

Figure 4.8 SEM and CL images of nano-bubbles with slit cuts. (a),(d) SEM images of the nano-bubbles with square and circular slit cuts. (b),(c),(e),(f) Panchromatic images and monochromatic images at the wavelength of 550nm.

4.6. Summary and Conclusion

I have demonstrated the localized light generation from the nano-bubble cavity probed by CL microscopy. Newton's Ring like fringes with their widths below the diffraction limit is

observed. A mode analysis and an electric dipole based modeling indicate that the bright rings are due to the enhancement of luminescence from the cavity effects: outer ring from a plasmonic cavity and inner rings from a conventional cavity. Using CL, the contributions from different modes are successfully separated, mapping two dimensional LDOS in the thin α-Si membrane. The MIS bubble structure is potentially useful as an effective light emitting device to enhance the internal quantum efficiency of gain medium or to improve the light extraction from the device. Also, continuous metal and semiconductor films provide an advantage for the potential electric-optic LED application.

Chapter 5 Summary and Future Work

5.1. Summary

This dissertation has dealt with the design and characterization of active plasmonic devices. I have addressed individual plasmonic structures as well as arrays of resonant structures forming a homogenized metamaterial with unconventional optical properties designed for applications in active plasmonics. Novel characterization techniques were investigated to probe the subwavelength information in nanoscale plasmonics structures. Theoretical modeling was provided to explain the underlying physical principles.

After a brief overview of recent advances in the field of nano-optics, the second chapter investigated the role of SPPs in transmission through a subwavelength hole. Optical phase measurements using NSOM showed an unusually large phase shift due to the coupling and re-radiation of SPPs, which is not explained by the traditional diffraction theory. The same concept is extended to the case of metamaterial, where the broadening of PSF is measured due to near zero magnetic permeability of metamaterial.

In the third chapter, NIM fishnet metamaterial is developed for an all-optical modulator. A rotated fishnet structure is designed, based on the LC circuit modeling and 3D FDTD simulation. Both near-field and far-field optical characterization is done to investigate local optical modes and their resulting effect in terms of modulation. The refractive index change of an active medium is amplified more than 10-fold, and as a result, a 40% modulation depth with ultrafast response time of 2ps is observed, according to the pump-probe measurement.

Finally, chapter 4 described light generation from a plasmonic nano-bubble cavity measured by CL microscopy. Newton's ring-like fringes with an unprecedented optical resolution is demonstrated to show luminescence enhancement due to the Purcell effect of the plasmonic cavity. Each ring is originated from increased LDOS, due to the optical mode formation, including plasmonic and TM modes. Such a structure is potentially useful for light-emitting devices with improved quantum efficiency.

5.2. Future Work

This work presents a unique platform to investigate both theoretical and experimental aspects of plasmonic nanostructures. Based on the understanding gained so far, there are certain key directions that would benefit from further consideration.

- Improvement of cathodoluminescence microscope, including the addition of capability for angular measurement, which can be useful in separating different contribution of generated light, such as SPP and transition radiation.
- Improvement of modeling to explain the dependence of CL signals in electron acceleration voltage.
- Experimental demonstration of nanoscale light emitting diode, made out of plasmonic bubble, by replacing amorphous silicon with direct bandgap semiconductor. Lifetime measurement of generated photon is a complimentary experiment to verify Purcell effect.
- Experimental demonstration of an electro-optic modulation using plasmonic structures for potential incorporation with CMOS electronics.

- Development of an effective active medium for active plasmonic devices. One of the promising candidates is transparent conducting oxides, such as ITO, due to its high carrier density and low refractive index. Graphene is also of great interest on account of its high carrier mobility.

Appendix A Ultrathin Absorber for Optoelectric Devices

A.1. Zero Reflection Induced by π/4 Optical Phase Difference

Effective collection of photons in optoelectric devices such as a photodetector or a solar cell is crucial to improve efficiencies of the devices. In this chapter, I show a simple concept that can be used to achieve near perfect absorption with only about half-quarter wavelength thick absorbing layer at visible wavelength.

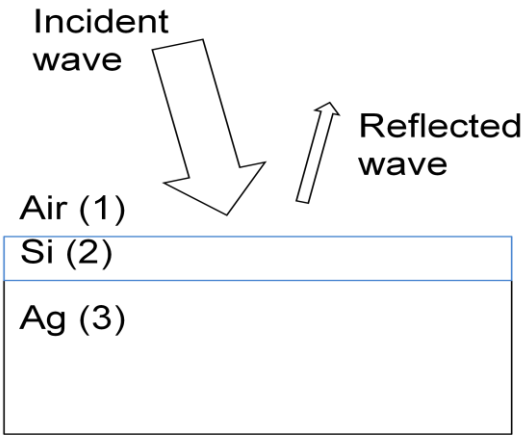

Figure A.1 Schematic view of tri-layer structure with α-Si as an absorbing medium and Ag as a reflective back plate.

For the sake of simplicity, a normal incidence case is first considered. Using Fresnel's equation, total reflection coefficient is calculated to be $r_{123} = \frac{r_{12} + r_{23} e^{2ik_2 d}}{1 + r_{12} r_{23} e^{2ik_2 d}}$,

where $r_{12} = \frac{n_2 - n_1}{n_2 + n_1}$, $r_{23} = \frac{n_3 - n_2}{n_3 + n_2}$.

To have zero reflection, which is when $r_{123} = 0$, it is necessary to have $r_{12} = r_{23}e^{2ik_2 d}$ which means $|r_{12}| = |r_{23}e^{2ik_2 d}|$ and $Arg(r_{12}) = Arg(r_{23}e^{2ik_2 d}) = 0$. If the layer 3 is metallic and layer 2 is high index dielectric with relatively small imaginary term, zero reflection is achieved with phase matching condition of $k_2 d \approx \pi / 4$ with an appropriate imaginary dielectric constant of layer 2 determined from the condition given by $|r_{12}| = |r_{23}e^{2ik_2 d}|$.

A.2. Experimental Results and Discussions

At the wavelength of 600nm, $d \approx 20nm$ and $\mathrm{Im}(n_2) \approx 0.5$. In this case, near-zero reflection is achieved only with only 20nm thick semiconductor layer placed on top of highly reflective surface. Such effect is calculated and plotted in Fig A.2 (b) using reference optical constants of silver and amorphous silicon. In Fig.A.2 (b), corresponding experimental results are plotted.

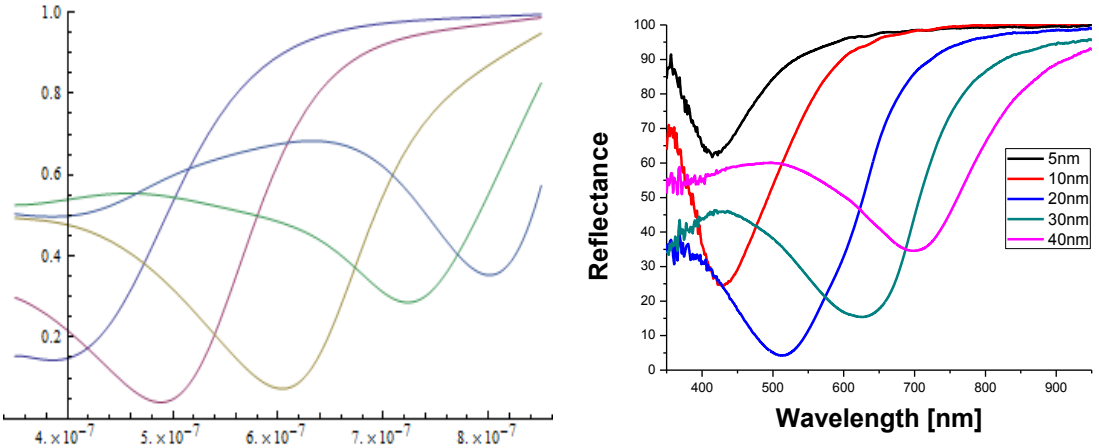

Figure A.2 (a) Calculated reflectance of ultrathin absorbers with varying the thickness of α-Si layer. (b) Experimental measurements of reflectance spectrum.

In optoelectric application, it is desirable that the absorption happens inside the active semiconductor region so that one can take advantage of photo-generated carriers. The absorption in each medium is plotted by calculating the gradient of Poynting vector in Fig. A.3. It is also observed that such effect is omni-directional, showing near-zero reflection up to 60 degree angle of incidence.

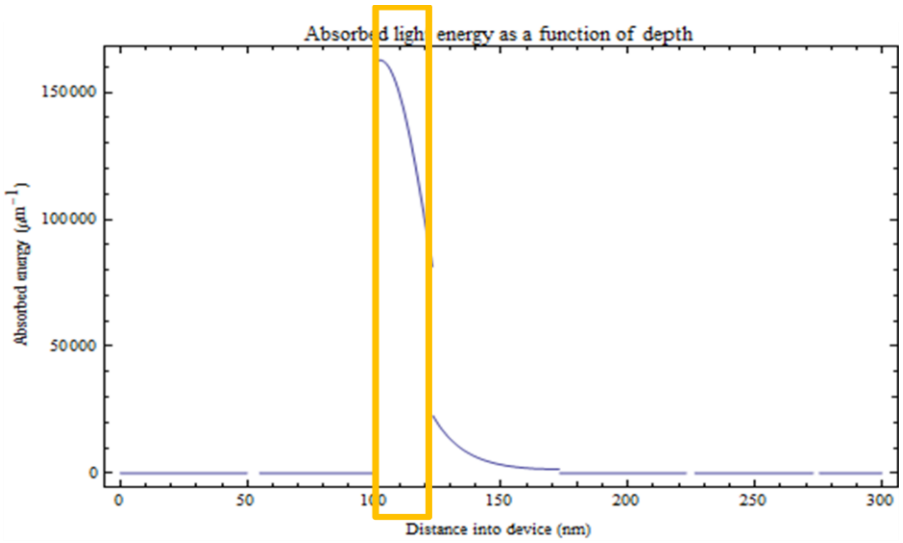

Figure A.3 Calculated absorption profile across the medium. 91% of total photon energy is absorbed in the amorphous silicon region. The yellow rectangular are indicates where amorphous silicon is placed.

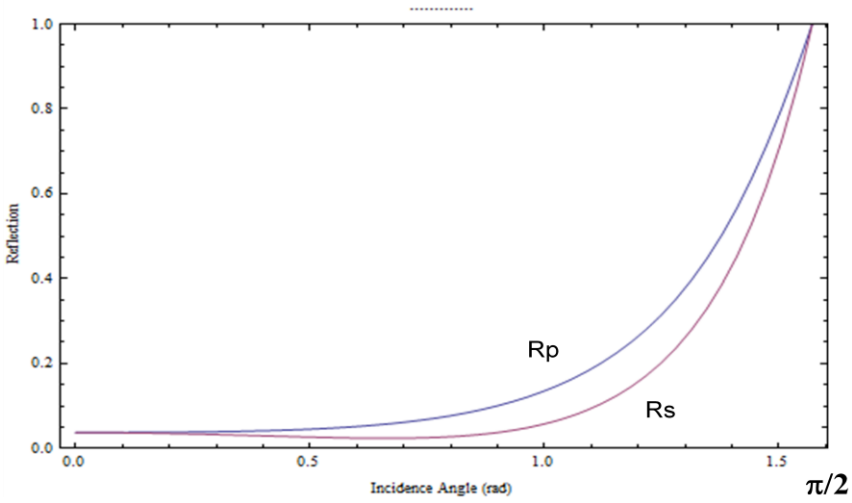

Figure A.4 Calculated reflectance as a function of the angle of incidence. Near-zero reflection is achieved up to 60 degree angle of incidence.

Similar effects are also observed by replacing the silver with other lossy metallic layers such as Cr, W and Mo. However, due to the loss in the metallic layer, the portion of light that is absorbed in the semiconductor active layer becomes significantly smaller, which limits its application.

Appendix B Metal-Dielectric-Metal Plasmonic Waveguide

B.1. Background and Motivation

Metal-dielectric-metal (MDM) waveguides are one of the promising structures to realize a negative group velocity for propagating SPPs [102,103]. In this chapter, I demonstrate an experimental study of SPPs propagating through MDM waveguide using near field scanning optical microscope (NSOM).

In Fig. B.1, dispersion diagrams of both plasmonic and dielectric modes is plotted. Negative slope of dispersion curve indicates negative group velocity. At the interface of two waveguides with a mode matching condition but different sign in group velocity, the negative refraction is expected.

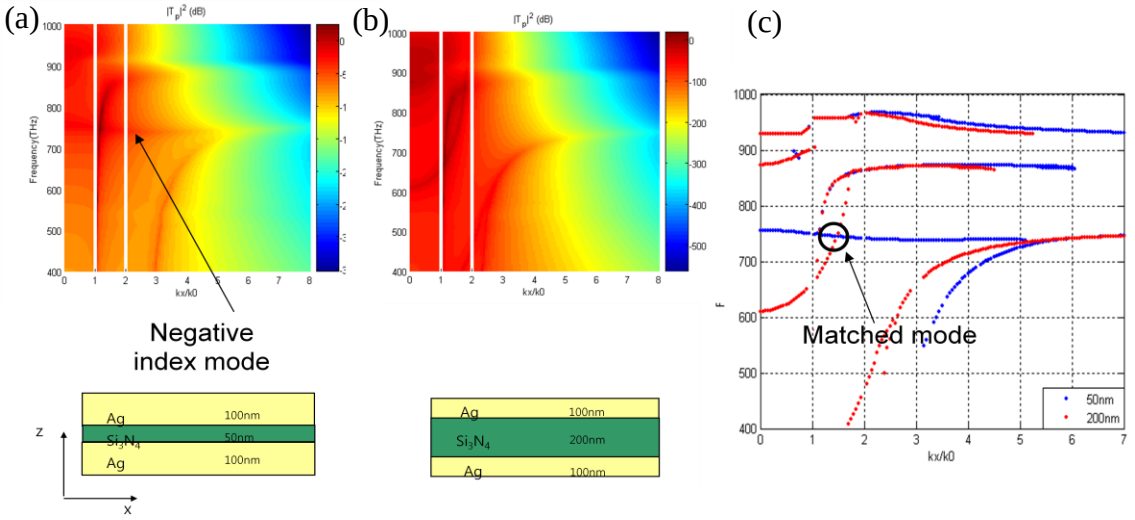

Figure B.1 Dispersion plots of metal-dielectric-metal waveguides. (a) If two metal layers are placed closely, interaction between SPP on top and bottom layer splits the plasmonic mode into

two. Negative slope indicates negative group velocity. (b) With 200nm-thick silicon nitride dielectric layer, TM modes of waveguide starts to show up. (c) The plasmonic mode and the TM mode overlap at 750Thz. Negative refraction is expected at this region. (Courtesy of Dr. Shu Zhang)

B.2. Experimental Results and Discussions

The MDM waveguide is fabricated using a shadow mask deposition utilizing an extremely thin silicon nitride membrane that is commercially available [104]. In Fig. B.2, focused ion beam milling is used to make a designed pattern on the mask membrane. A 0.5nm-thick Cr adhesion layer and a 50nm-thick Ag layer are deposited through the mask membrane on the sample membrane using e-beam evaporation. The other side of the sample membrane is coated with Au to form the Ag-Si_3N_4-Au hetero MDM structure. The resulting structure is shown in Fig. B.3.

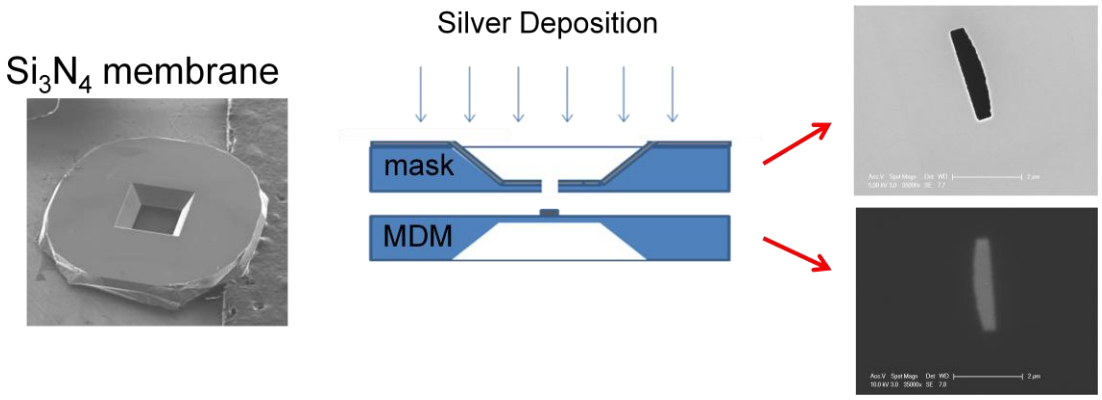

Figure B.2 Fabrication of MDM waveguides on the silicon nitride membrane using the shadow mask deposition.

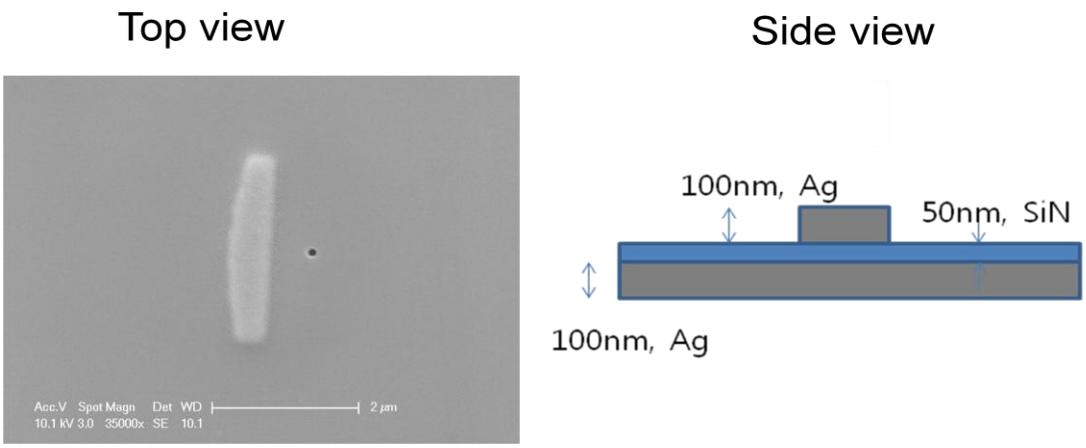

Figure B.3 Top and side views of the MDM lens fabricated on the Si_3N_4 membrane

The NSOM is employed to measure the propagating SPP waves along the membrane surface. Fig. B.4 shows how SPP wave that is launched from the slit propagates at the interface of MD and MDM. The refraction of SPP wave is observed. In Fig. B.5, SPP propagation through the MDM lens is measured. In both cases, SPPs are launched by focusing a laser beam with 482nm wavelength onto the thin slit cut on the membrane.

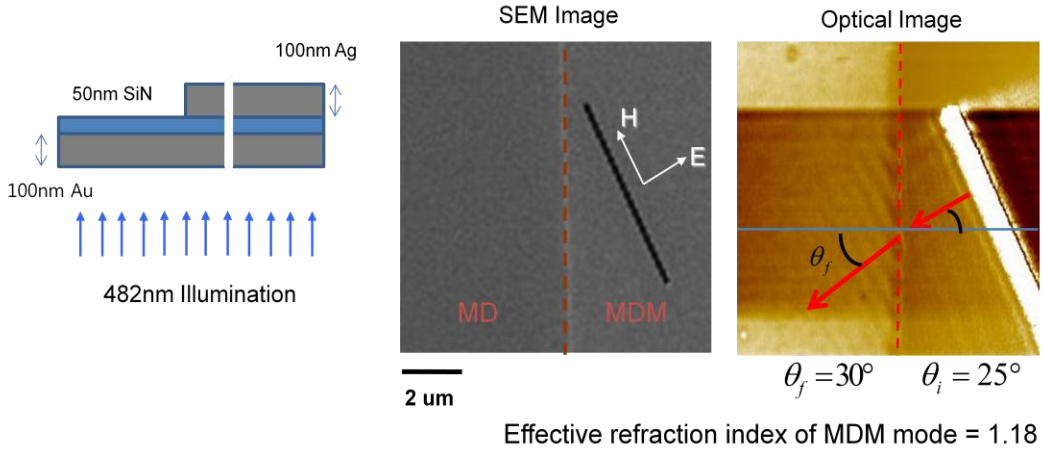

Figure B.4 Refraction of surface plasmon wave at MDM / MD interface

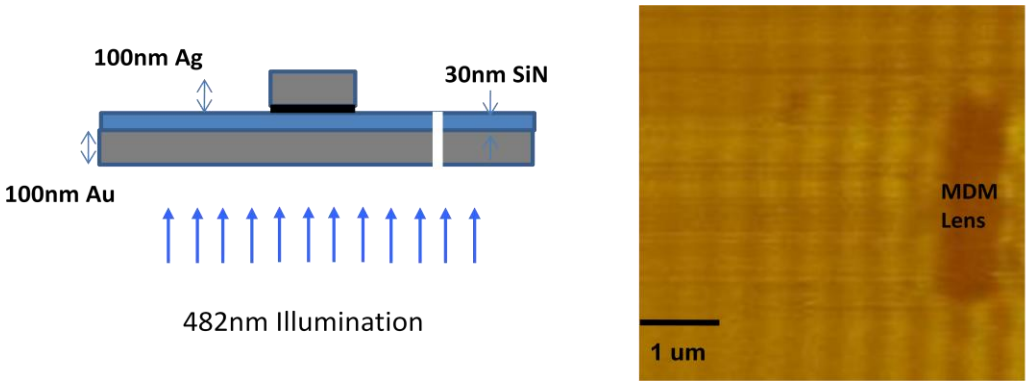

Figure B.5. Refraction of surface plasmon wave by the MDM lens

Appendix C Light Transmission through a Subwavelength Hole Measured by Confocal Microscope

C.1. Background and Motivation

A scanning confocal microscope provides a quick and easy-to-access focused light beam with high z-axis resolution although the focused light is still diffraction limited. A focused beam is used to excite plasmonic modes in a subwavelength hole, and the transmitted light is collected by the PMT. Optical fringes due to the interference between the through-hole transmission and through-metal film transmission is observed. This is very similar to the case discussed in chapter 2. The underlying mechanism is not clear enough to explain observed pattern, yet it shows a strong potential in using confocal microscope to study the phase effect in plasmonic systems.

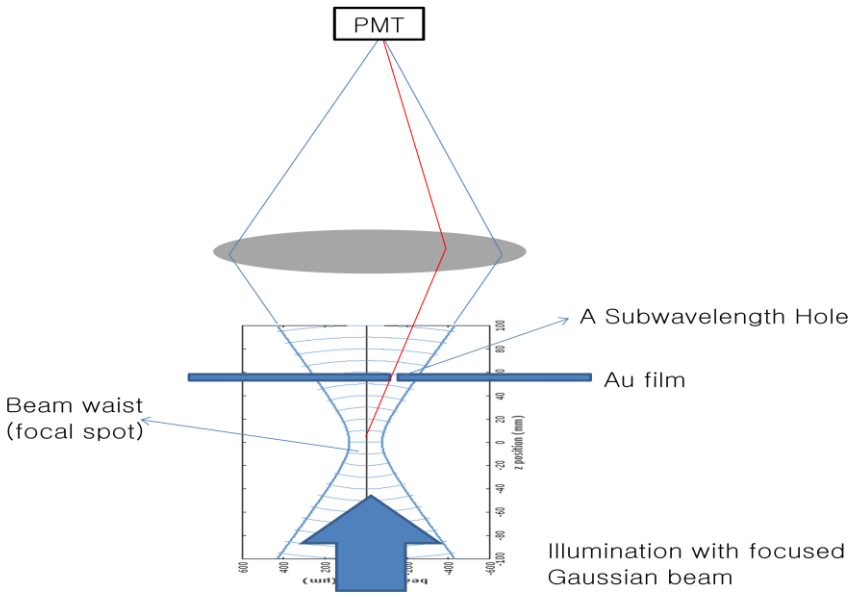

Figure C.1 Schematic view of the system representing the sample illumination and collection of transmitted light. A red beam path indicates the contribution of light transmitted through a subwavelength hole.

C.2. Experimental Results and Discussions

Subwavelength holes with different sizes (800, 500, 300, 200 and 100nm in diameter) are milled through 60nm thick gold film using FIB. A laser beam with the wavelength of 488nm is focused and scanned over the sample in XY plane and XZ plane. The transmitted light is collected by the PMT as shown in Fig. C.1. The resulting interference images are shown in Fig. C.2, C.3 and C.4. Interestingly, there is a vertical displacement of interference fringes in the case of a metallic dent compared to a through hole, shown in Fig. C.4. This is due to the difference in the phase change through a hole and a dent.

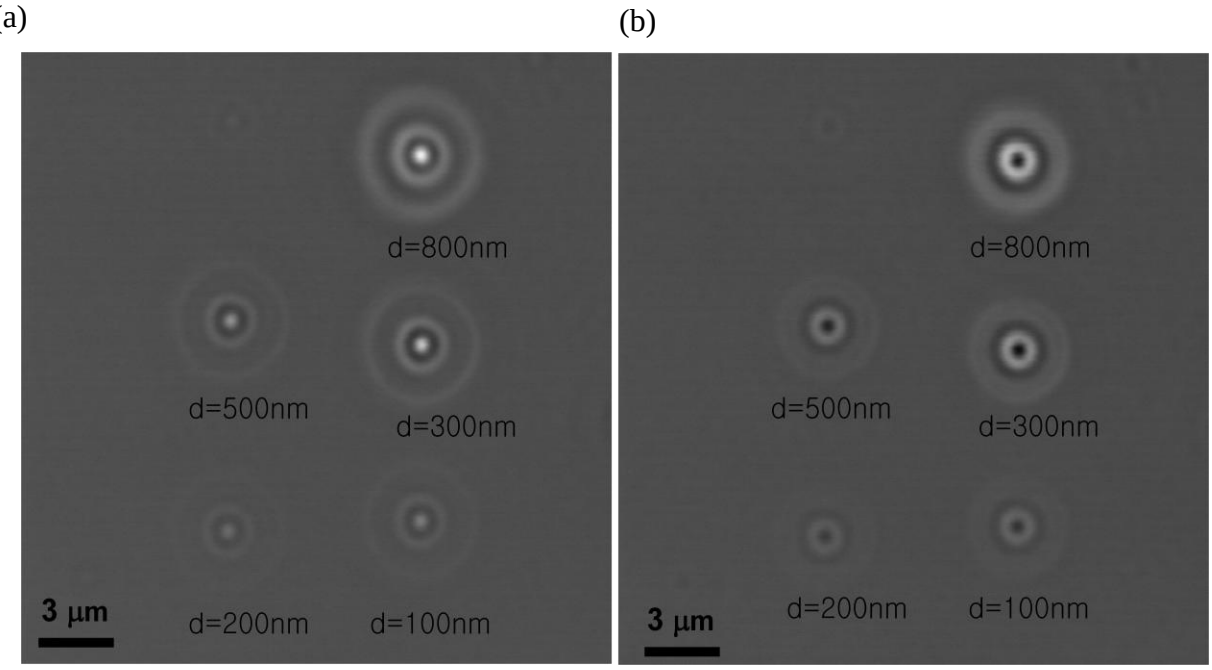

Figure C.2 Fringes measured under the XY scan mode with various hole sizes at fixed height.

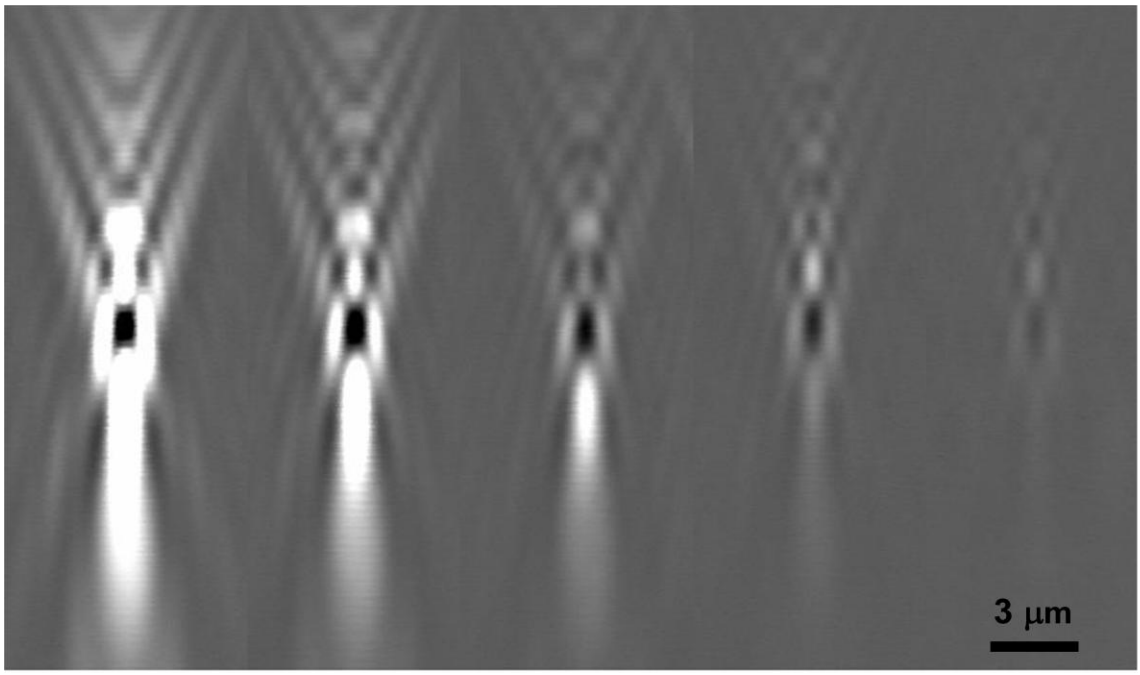

Figure C.3 Fringes measured under the XZ scan mode with various hole sizes. The vertical imaging plane crosses the center of the subwavelength holes. The size of the holes is 800nm, 500nm, 300nm, 200nm and 100nm from left to right.

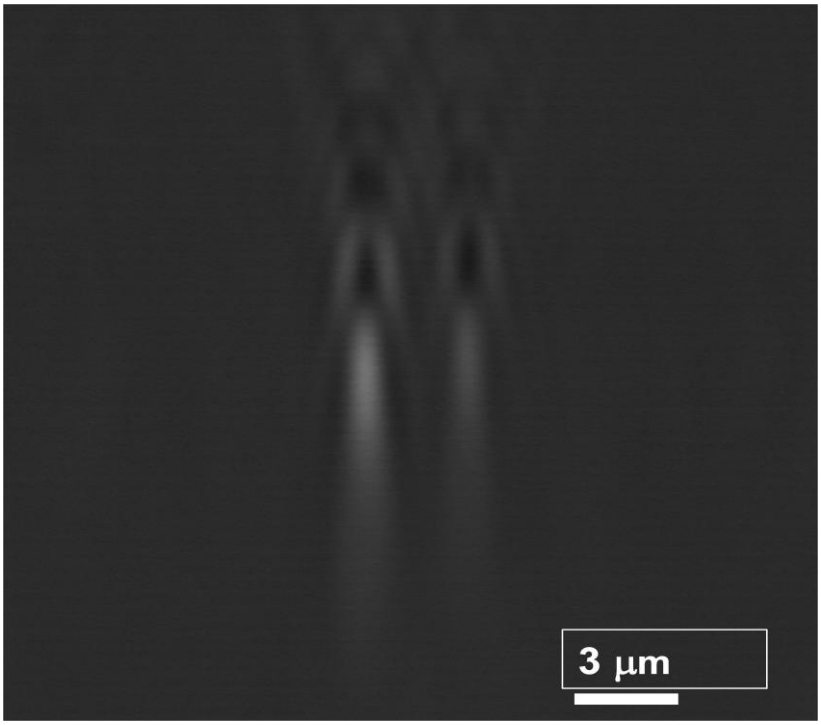

Figure C.4 Interference fringes for a hole (left) and a dent (right). There is a displacement of fringe in vertical direction due to the difference of phase in light transmitted through the hole and dent.

Appendix D Electric Modulation of Rotated Fishnet Optical Modulator

D.1. Background and Motivation

Toward building an on-chip optical modulator integrated with traditional semiconductor electronics, it is desirable to perform an optical modulation with electrical pumping. A preliminary experiment for an electric modulation of fishnet metamaterial modulator is given in this chapter.

D.2. Experimental Results and Discussions

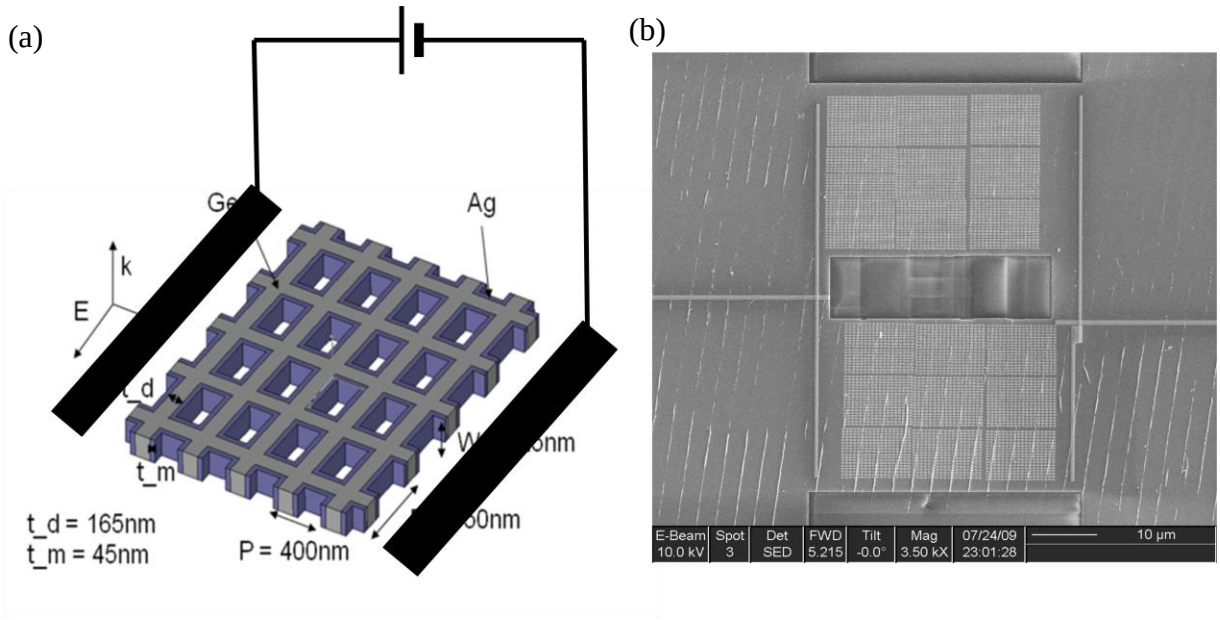

Figure D.1 (a) Schematic view of rotated fishnet modulator for the electric modulation. (b) A SEM image of rotated fishnet metamaterial with Pt electrodes.

A rotated fishnet structure is fabricated according to the design give in the chapter 3. Additionally, a Pt electrode is deposited at the boundary of the fishnet region, as shown in Fig. D.1. Considering that the sample was made on a glass substrate and a thin layer of α-Ge is highly resistive to the electric current, most of the current is flowing through the fishnet structure. To prevent any shortage, the top silver layer is eliminated except for the fishnet region.

As a preliminary experiment, photoconductive current is measured. (See Fig. D.2.) It is shown that the nature of electric contacts between α-Ge and Ag in the fishnet structure is ohmic, showing no voltage barrier or hysteresis. It is also observed that the photo-induced carrier results in higher current when there is an external optical pumping of 20mW continuous wave laser focused on 30μm by 30μm area.

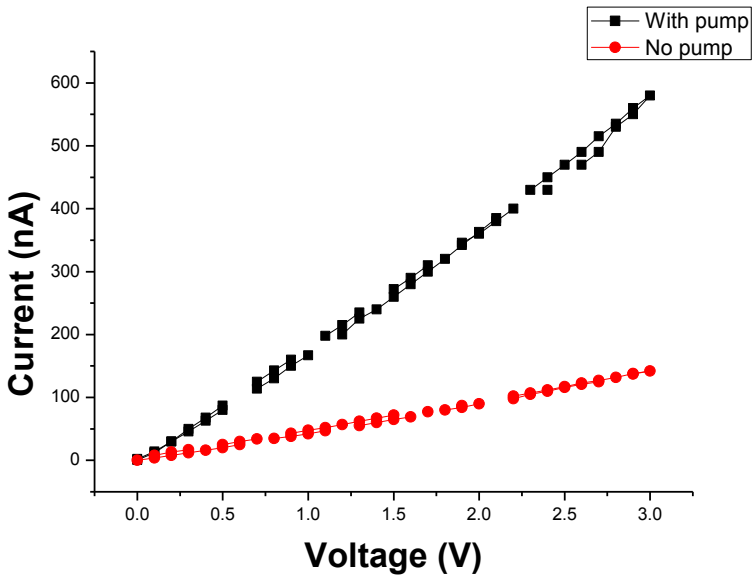

Figure D.2 Experimental measurements of IV curves with and without external optical pumping. The measured curve indicates linear relationship between the voltage and current. As an external pumping, 20mW continuous wave laser beam at 482nm wavelength is focused into the area of approximately 30μm by 30μm. No hysteresis or threshold voltage is observed; indicating the nature of the contacts between α-Ge and Ag are ohmic.

Appendix E Cathodoluminescence Imaging of Nano-discs and Slits

E.1. Background and Motivation

The ultrahigh imaging resolution of cathodoluminescence microscope makes it a perfect choice to probe local optical modes in plasmonic nanostructures. In the case of samples with planar geometry, CL can be modeled using a simple dipole picture, as is shown in chapter 4. In principle only radiative optical modes are being captured by the CL imaging, however, non-radiative modes can be also collected via scattering at the surface [91]. Depending on the sample geometry, interferences between radiative modes and scattered non-radiative modes can complicate the understanding of measured CL spectra or images. This chapter is dedicated to some representative cases which require further improvements in modeling to fully understand the CL microscope.

E.2. Experimental Results and Discussions

Various plasmonics nanostructures such as slits, discs and arcs are made on a silicon substrate. Tri-layer deposition of optically thick silver, 5nm thick MgF_2 and 25nm thick α-Si are done on a silicon wafer. And then, various nanostructures are fabricated using focused ion beam (FIB) milling, as shown in Fig. E.1 – E.4.

Panchromatic CL imaging indicates that there is a strong radiation from the sharp corner of metallic nanoparticles, as shown in Fig. E.1. It is observed that the curvature of the particle affects the CL intensity regardless of resonant optical modes in the system. The exact opposite effect, a weak radiation from concave structure is also observed, as shown in Fig. E.2.

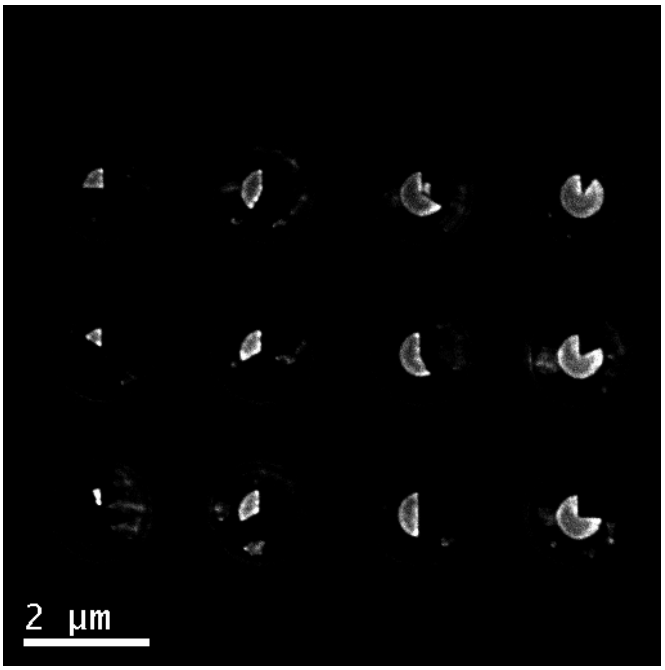

Figure E.1 Demonstration of curvature effect in the CL image of nano-particles.

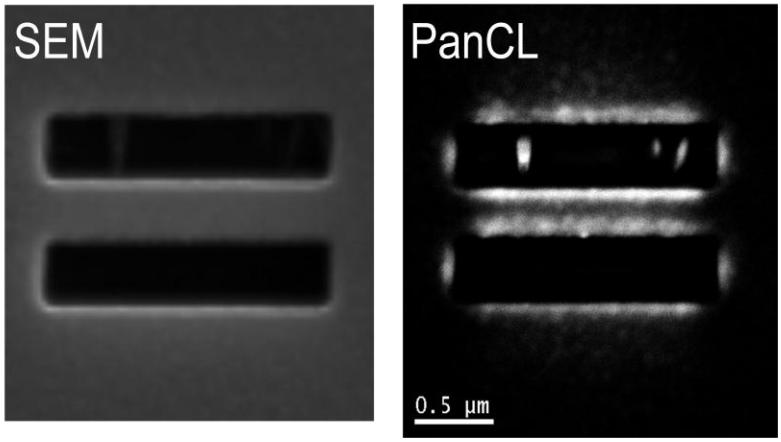

Figure E.2 (a) SEM image of double slits. (b) The corresponding optical images measured by the CL microscope.

It is shown that the intensity of CL becomes stronger as the size of the disc becomes smaller, as shown in Fig. E.3. It is also noted that the intensity of CL is dramatically enhanced nearby the sharp edges, while the other areas remain unchanged. (See Fig. E.4.)

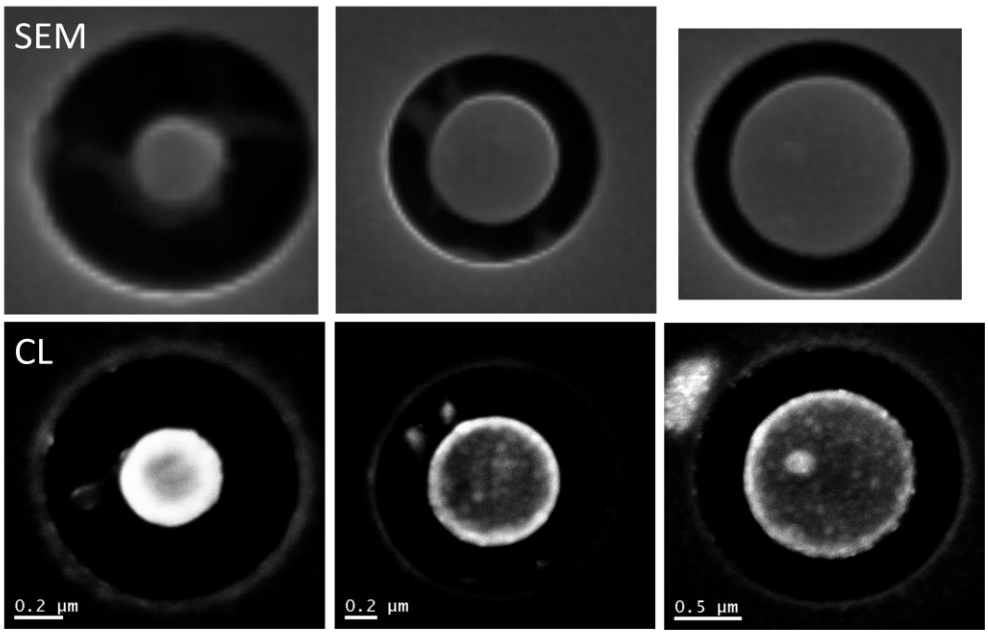

Figure E.3 Cathodoluminescence imaging of nano-discs.

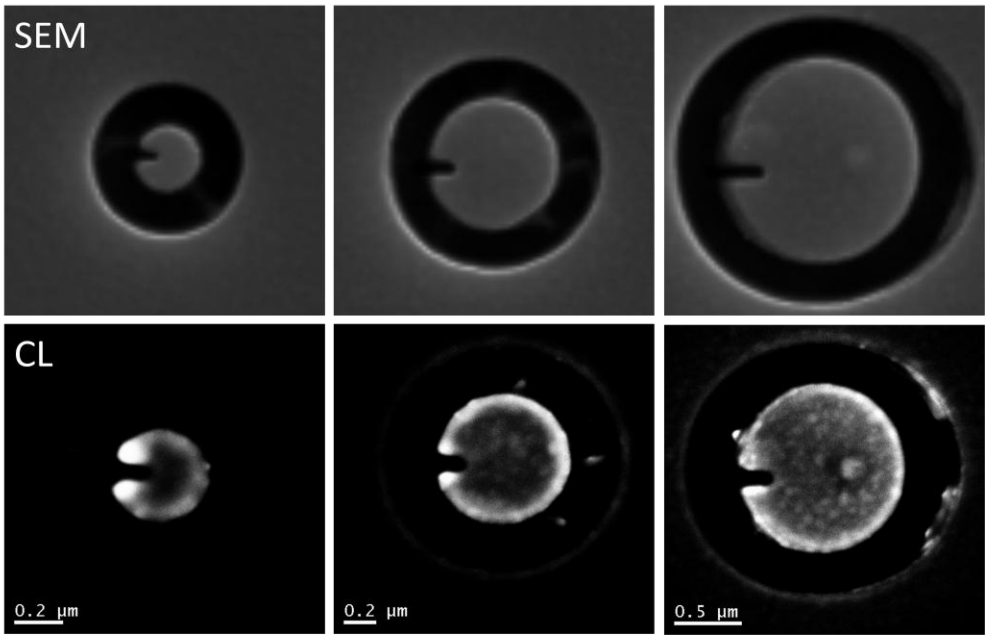

Figure E.4 Cathodoluminescence imaging of nano-discs without side-cuts.

References

[1] Abbe, E., *Arch. Mikroskop. Anat*. **9**, 413-420 (1873)

[2] Rayleigh, L., Investigations in optics, with special reference to the spectroscope. *Phil. Mag*. **8**, 261-274/403-411/477-486 (1879)

[3] Förster, T., *Modern Quantum Chemistry* **3**, 93-137 (1965)

[4] Jares-Erijman, E.A. et al. FRET imaging. *Nature Biotechnology* **21**, 1387-1395 (2003)

[5] Hell, S.W. Far-field optical nanoscopy. *Science* **316**, 1153-8 (2007).

[6] Willig, K.I. et al. STED microscopy reveals that synaptotagmin remains clustered after synaptic vesicle exocytosis. *Nature* **440**, 935-9(2006).

[7] Betzig, E. et al. Proteins at Nanometer Resolution. *Science* **1642**, (2011).

[8] Rust, M.J. et al. Imaging by stochastic optical reconstruction microscopy (STORM). *Nature Methods* **3**, 793-795 (2006).

[9] Betzig, E., Near Field Scanning Optical Microscopy (NSOM): Development and Biophysical Applications. *Biophysical Journal* **49**, 269-279 (1986).

[10] Ebbesen, T.W. et al. Extraordinary optical transmission through sub-wavelength hole arrays. *Nature* **391**, 667-669 (1998).

[11] Porto, J.A. et al. Transmission resonances on metallic gratings with very narrow slits, *Phys. Rev. Lett.*, **83**, 2845-2848 (1999).

[12] Degiron, A. et al. The role of localized surface plasmon modes in the enhanced transmission of periodic subwavelength apertures, *J. Opt. Pure Appl. Opt.*, **7**, S90-S96 (2005).

[13] Yin, L. et al. Subwavelength focusing and guiding of surface plasmons. *Nano letters* **5**, 1399-402 (2005).

[14] Bozhevolnyi, S.I. et al. Channel plasmon subwavelength waveguide components including interferometers and ring resonators. *Nature* **440**, 508-11 (2006).

[15] Barnes, W.L. et al. Subwavelength optics. *Nature* **424**, 824-830 (2003).

[16] Gramotnev, D.K. et al. Plasmonics beyond the diffraction limit. *Nature Photonics* **4**, 83-91 (2010).

[17] Schuller, J. et al. Plasmonics for extreme light concentration and manipulation. *Nature materials* **9**, 193-204(2010).

[18] Liu, Z.-W. et al. Surface plasmon interference nanolithography. *Nano letters* **5**, 957-61 (2005).

[19] Anker, J.N. et al. Biosensing with plasmonic nanosensors. *Nature materials* **7**, 442-53 (2008).

[20] Pendry, J.B. Negative refraction makes a perfect lens. *Physical review letters* **85**, 3966-9 (2000).

[21] Fang, N. et al. Sub-diffraction-limited optical imaging with a silver superlens. *Science* **308**, 534-7 (2005).

[22] The top ten advances in materials science. *Materials Today* **11**, 40-45 (2008).

[23] Veselago, V.G. The electrodynamics of substances with simultaneously negative values of ε and μ. Sov. Phys. Usp. 10, 509–514 (1968)

[24] Shelby, R.A. et al. Experimental Verification of a Negative Index of Refraction. *Science* **292**, 77-79 (2001).

[25] Wolf, E. et al. Controlling Electromagnetic Fields. *Science* **312**, 1780-1782 (2006).

[26] Schurig, D. et al. Metamaterial electromagnetic cloak at microwave frequencies. *Science* **314**, 977-80 (2006).

[27] Saleh B. et al. *Fundamentals of Photonics*. Wiley-Interscience (1991)

[28] Sze S.M. et al. *Physics of Semiconductor Devices*. Wiley-Interscience (2007)

[29] Ozbay, E. Plasmonics: merging photonics and electronics at nanoscale dimensions. *Science* **311**, 189-93(2006).

[30] Novotny L. et al. *Principles of Nano-Optics*. Cambridge University Press (2006)

[31] Fleischmann, M. et al. Raman Spectra of Pyridine Adsorbed at a Silver Electrode, *Chemical Physics Letters* **26**, 163–166 (1974).

[32] Nie, S.M. et al. Probing single molecules and single nanoparticles by surface-enhanced Raman scattering. *Science* **275**, 1102-1106 (1997).

[33] Purcell, E.M. et al. Spontaneous emission probabilities at radio frequencies. *Physical Review* **69**, 681 (1946).

[34] Hill, M.T. et al. Lasing in metallic-coated nanocavities. *Nature Photonics* **1**, 589-594 (2007).

[35] Oulton, R.F. et al. Plasmon lasers at deep subwavelength scale. *Nature* **461**, 629-32 (2009).

[36] Noginov, M. a et al. Demonstration of a spaser-based nanolaser. *Nature* **460**, 1110-2 (2009).

[37] Ma, R.-M. et al. Room-temperature sub-diffraction-limited plasmon laser by total internal reflection. *Nature Materials* **10**, 2-5 (2010).

[38] Knight, M.W. et al. Photodetection with active optical antennas. *Science* **332**, 702-4 (2011).

[39] Chen H.T. et al. Active terahertz metamaterial devices. *Nature* **444**, 597–600 (2006)

[40] Tang, L. et al. Nanometre-scale germanium photodetector enhanced by a near-infrared dipole antenna. *Nature Photonics* **2**, 226-229 (2008).

[41] Fang, N. et al. Ultrasonic metamaterials with negative modulus. *Nature Materials.* **5** (2006).

[42] Guenneau S,A. et al. Acoustic metamaterials for sound focusing and confinement *New Journal of Physics* **9**, 1367–2630 (2007).

[43] Bohren, C.F. *Absorption and scattering of light by small particles*. Wiley-Interscience (2010)

[44] Smith, D.R. et al. Metamaterials and negative refractive index. *Science* **305**, 788–792 (2004)

[45] Yao, J. et al. Optical negative refraction in bulk metamaterials of nanowires. *Science* **321**, 2008-2008 (2008).

[46] Dolling, G. et al. Negative-index metamaterial at 780 nm wavelength. *Optics Letters* **32**, 2006-2008 (2007).

[47] Guven, K. et al. Experimental observation of left-handed transmission in a bilayer metamaterial under normal-to-plane propagation. *Optics express* **14**, 8685-93 (2006).

[48] Kim, E. et al. Modulation of negative index metamaterials in the near-IR range. *Applied Physics Letters* **91**, 173105 (2007).

[49] Dani, K.M. et al. Subpicosecond optical switching with a negative index metamaterial *Nano Letters* **9**, 3565–3569 (2009).

[50] Smith D.R. et al. Direct calculation of permeability and permittivity for a left-handed metamaterial. *Applied Physics Letters*, **77**, 2246-2248 (2000)

[51] Engheta, N.et al. *Metamaterials: Physics and Engineering Explorations*. Wiley & Sons (2006)

[52] Lezec, H.J. et al. Diffracted evanescent wave model for enhanced and suppressed optical transmission through subwavelength hole arrays. *Optics Express* **12**, 3629-3651 (2004).

[53] Janssen O.T.A. et al. On the phase of plasmons excited by slits in a metal film. *Optics Express* **14**,11823-11832 (2006).

[54] Weiner, J. Phase shifts and interference in surface plasmon polariton waves. *Optics Express* **16**, 950-956 (2008).

[55] Obermuller, C. et al. Far-field characterization of diffracting apertures. *Applied Physics Letters* **67**, 3408-3410 (1995).

[56] Degiron, A. et al. Optical transmission properties of a single subwavelength aperture in a real metal. *Optics Communications* **239**, 61-66 (2004).

[57] Yin, L. et al. Surface plasmons at single nanoholes in Au films. *Applied Physics Letters* **85**, 467-469 (2004).

[58] Jackson, J. *Classical Electrodynamics.* Chapter 10.9, 3rd Edition, Wiley (1998).

[59] Stratton J.A. *Electromagnetic Theory*, 464, IEEE Press (1941)

[60] Bethe, H.A. Theory of diffraction by small holes. *Physical Review* **66**, 163-182 (1944)

[61] Bouwkamp, C.J. On Bethe's theory of diffraction by small holes. *Philips Research Report* **5**, 321 (1950)

[62] Smythe, W.R. The double current sheet in diffraction. *Physical Review.* **72**, 1066-1070 (1947)

[63] Buchsbaum, S.J. Microwave diffraction by apertures of various shapes. *Journal of Applied Physics* **26**, 706-715 (1955)

[64] Huang, C. Diffraction by apertures. *Journal of applied physics* **26**, 151-165 (1954)

[65] Ebbesen, T.W. et al. Extraordinary optical transmission through sub-wavelength hole arrays. *Nature* **391**, 667-669 (1998).

[66] Cao, Q. Negative role of surface plasmons in the transmission of metallic gratings with very narrow slits. *Physical Review Letters* **88** 057403 (2002)

[67] Kim J.W. et. al. Terahertz electromagnetic wave transmission through random arrays of single rectangular holes and slits in thin metallic sheets. *Physical Review Letters* **99**, 137401 (2007)

[68] Palik, E. D. *Handbook of Optical Constants of Solids*. Academic Press (1998).

[69] Hakkarainen, T. Subwavelength electromagnetic near-field imaging of point dipole with metamaterial nanoslab. *Journal of Optical Society of America A* **26**, 2226–2234 (2009).

[70] Zapata-Rodr´ıguez, C.J. et al. Three-dimensional point spread function and generalized amplitude transfer function of near-field flat lenses. *Applied Optics* **49**, 5870–5877 (2010).

[71] Smith, D.R. et al. Determination of effective permittivity and permeability of metamaterials from reflection and transmission coefficients. *Physical Review B* **65**, 195104 (2002).

[72] Zhang, S. Experimental demonstration of near-infrared negative-index metamaterials. *Physical Review Letters*, **95**, 137404 (2005).

[73] Kafesaki, M. et al. Left-handed metamaterials: The fishnet structure and its variations. *Physical Review B* **75**, 1-9 (2007).

[74] Gibson R. et al. Improved sensing performance of D-fiber/planar waveguide couplers. *Optics Express* **15**, 2139-2144 (2007).

[75] Mendez, A. et al. *Specialty Optical Fibers Handbook*, Academic Press (2007).

[76] Weiland, T. et al. Ab initio numerical simulation of left-handed metamaterials: Comparison of calculations and experiments. *Journal of Applied Physics* **90**, 5419 (2001).

[77] Schurig, D. Off-normal incidence simulations of metamaterials using FDTD. *International Journal of Numerical Modelling: Electronic Networks, Devices and Fields* **19**, 215-228 (2006).

[78] Ozbay, E. Plasmonics: merging photonics and electronics at nanoscale dimensions. *Science* **311**, 189-93(2006).

[79] Anker, J.N. et al. Biosensing with plasmonic nanosensors. *Nature materials* **7**, 442-53 (2008).

[80] Schuller, J. a et al. Plasmonics for extreme light concentration and manipulation. *Nature materials* **9**, 193-204 (2010).

[81] Gramotnev, D.K. et al. Plasmonics beyond the diffraction limit. *Nature Photonics* **4**, 83-91 (2010).

[82] Andrew, P. et al. Molecular fluorescence above metallic gratings. *Physical Review B* **64**, 1-11 (2001).

[83] Drexhage, K.H. et al. Variation of fluorescence decay time of a molecule in front of a mirror. *Berichte der Bunsengesellschaft für physikalische Chemie* **72**, 329 (1968)

[84] Chance, R.R. et al. Molecular fluorescence and energy transfer near interfaces. *Advances in Chemical Physics* **37**, 1-65 (1978)

[85] Ford, G.W. Electromagnetic interactions of molecules with metal surfaces. *Physics Reports* **113**, 195-287 (1984)

[86] Bergman, D. et al. Surface Plasmon Amplification by Stimulated Emission of Radiation: Quantum Generation of Coherent Surface Plasmons in Nanosystems. *Physical Review Letters* **90**, 1-4 (2003).

[87] Walters, R.J. et al. A silicon-based electrical source of surface plasmon polaritons. *Nature Materials* **9**, 21-25 (2009).

[88] Hryciw, A. et al. Plasmon-enhanced emission from optically-doped MOS light sources. *Optics Express* **17**, 185-92 (2009).

[89] Almeida, V.R. et al. Guiding and confining light in void nanostructure. *Optics Letters* **29**, 1209-1211 (2004).

[90] Oulton, R.F. et al. A hybrid plasmonic waveguide for subwavelength confinement and long-range propagation. *Nature Photonics* **2**, 496-500 (2008).

[91] García de Abajo, F.J. Optical excitations in electron microscopy. *Reviews of Modern Physics* **82**, 209-275 (2010).

[92] Yamamoto, N. et al. Photon emission from silver particles induced by a high-energy electron beam. *Physical Review* **64**, 1-9 (2001).

[93] Vesseur, E.J.R. et al. Direct observation of plasmonic modes in Au nanowires using high-resolution cathodoluminescence spectroscopy. *Nano Lett.* **7**, 2843-2846 (2007).

[94] Chaturvedi, P. et al. Imaging of plasmonic modes of silver nanoparticles using high-resolution cathodoluminescence spectroscopy. *ACS Nano* **3**, 2965-2974 (2009).

[95] Kumar, A. et al. Excitation and imaging of resonant optical modes of Au triangular nanoantennas using cathodoluminescence spectroscopy. *Journal of Vacuum Science & Technology B: Microelectronics and Nanometer Structures* **28**, C6C21 (2010).

[96] Kuttge, M. et al. Ultrasmall mode volume plasmonic nanodisk resonators. *Nano Letters* 1537-1541 (2010).

[97] Zhu, X. et al. Confined three-dimensional plasmon modes inside a ring-shaped nanocavity on a silver film imaged by cathodoluminescence microscopy. *Physical Review Letters* **105**, 1-4 (2010).

[98] Hofmann, C.E. et al. Plasmonic modes of annular nanoresonators imaged by spectrally resolved cathodoluminescence. *Nano Letters* (2007).

[99] Wolff, S. et al. Incident angle dependent damage of PMMA during Ar+-ion beam etching. *Microelectronic Engineering* **87**, 1444-1446 (2010).

[100] Verhagen, E. et al. Plasmonic nanofocusing in a dielectric. *Nano Letters* 3665-3669 (2010).

[101] Born, M.A., Wolf, E. *Principles of optics*. Pergamon Press (1959).

[102] Lezec, H.J. et al. Negative refraction at visible frequencies. *Science* **316**, 430-2 (2007).

[103] Shin, H. et al. All-Angle Negative Refraction for Surface Plasmon Waves Using a Metal-Dielectric-Metal Structure. *Physical Review Letters* **96**, 1-4 (2006).

[104] www.2spi.com

Author's Biography

Hyungjin Ma was born on Sep 5th, 1978 in Seoul, Korea. He received his B.S. degree in Physics from Seoul National University in 2004. Hyungjin joined Department of Physics at University of Illinois, Urbana-Champaign in fall 2005, and has been working with Prof. Nicholas Fang in the area of Nanophotonics since fall of 2006. His research has focused on design, fabrication and characterization of nano-optical devices including metamaterial based optical modulator, plasmonic nano-bubble light emitting device and etc. His research is presented in several conferences including OSA Meta, MRS and APS march meeting. After receiving his Ph.D., Hyungjin will join Intel Corporation in Portland, Oregon as RET design engineer.